

**MICROSCALE OPTICAL THERMOMETRY TECHNIQUES FOR
MEASURING LIQUID-PHASE AND WALL SURFACE
TEMPERATURES**

A Thesis
Presented to
The Academic Faculty

by

Myeongsub Kim

In Partial Fulfillment
of the Requirements for the Degree
Doctor of Philosophy in the
George W. Woodruff School of Mechanical Engineering

Georgia Institute of Technology
May 2011

**MICROSCALE OPTICAL THERMOMETRY TECHNIQUES FOR
MEASURING LIQUID-PHASE AND WALL SURFACE
TEMPERATURES**

Approved by:

Professor Minami Yoda, Advisor
George W. Woodruff School of
Mechanical Engineering
Georgia Institute of Technology

Professor Yogendra Joshi
George W. Woodruff School of
Mechanical Engineering
Georgia Institute of Technology

Professor Samuel Graham
George W. Woodruff School of
Mechanical Engineering
Georgia Institute of Technology

Professor Michael Schatz
School of Physics
Georgia Institute of Technology

Professor Donald Webster
School of Civil & Environmental
Engineering
Georgia Institute of Technology

Date Approved: December 9 2010

ACKNOWLEDGEMENTS

The completion of this thesis would not have been possible without the help, support, and guidance of many people. Foremost, I wish to thank my advisor Dr. Minami Yoda for her invaluable and continuous advice and support as I have pursued these studies. I would also like to express my gratitude to my committee members: Drs. Samuel Graham, Yogendra Joshi, Michael Schatz, and Donald Webster for their effort in reviewing this work and advices.

I am particularly grateful to Dr. Yutaka Kazoe at the University of Tokyo for helping me setting up the experimental apparatus in EFT studies; to Dr. Haifeng Li at Enercon, Inc and Mr. Keith Sudacederquist for sincere advices and helpful discussions; Dr. Tay-Gyu Hwang for selecting right fluorophores; to Mr. Zhenchun Peng and Dr. Peter Hesketh for sharing their facilities to fabricate PDMS channels; to Mr. E. Nakashio and Mr. J. Jones at Olympus corporation for getting proper laser beam; to Mr. A. Marash at CVI Melles Griot for tuning the laser; to MiRC staff members for helping me to learn and operate various equipments in cleanroom facilities.

Many thanks to my friends and laboratory colleagues, Yaofa Li for sharing the experimental setup with me, Dr. Leping Zhou, Necmettin Cevheri, and Tongran Qin for valuable discussions to my thesis. I also wish to thank Benjamin Chan, Ali Amahdavifar, Brantley Mills, and Jordan Rader for helpful suggestions.

More importantly, I wish to express my sincere appreciation to my parents and family for their continuous and unconditional support and love. Lastly, my deepest gratitude goes to my fiancée Jin A Kim. Without her love, support, and comprehension, none of this work which is important goal in my life would have been possible.

TABLE OF CONTENTS

ACKNOWLEDGEMENTS	iii
LIST OF TABLES	Vii
LIST OF FIGURES	Viii
SUMMARY	XV
I INTRODUCTION	1
1.1 Motivation	1
1.2 Thermal management in ICs.....	6
1.3 Why can microchannel flows efficiently cool electronic circuits?	11
II LITERATURE REVIEW	18
2.1 Liquid-Phase Thermometry	18
2.1.1 Laser-Induced Fluorescence Thermometry (FT)	18
2.1.2 Fluorescence Mechanism	20
2.1.3 How Fluorescence and Lifetime is Affected by Changes in Temperature	22
2.1.4 Thermochromic Liquid Crystal Thermometry	32
2.1.5 Particle Image Thermometry.....	34
2.2 Surface Thermometry Techniques	35
2.2.1 Micro-Thermocouple, Scanning Thermal Probe, and Diode Sensors 35	
2.2.2 Infrared Thermometry	38
2.2.3 Thermochormic Liquid Crystal Thermometry	39
III EXPERIMENTAL APPARATUS	43

3.1	Fluorescence Dyes	43
3.2	Optical Setups.....	46
3.2.1	Illumination Systems.....	46
3.2.2	Imaging Systems	52
IV	EVANESCENT WAVE-BASED FLUORESCENCE THERMOMETRY....	67
4.1	Total Internal Reflection Fluorescence Microscopy	67
4.1.1	Total internal reflection.....	67
4.1.2	Evanescent wave	69
4.2	Temperature Calibration for EFT Technique.....	70
4.2.1	Preparation of the working fluid	70
4.2.2	Experimental Setup	74
4.2.3	Temperature Calibration Results.....	80
4.3	EFT Results and Discussion	83
4.3.1	Results for PDMS-Glass Channels	83
4.3.2	Acrylic-Glass Channels.....	87
4.4	Numerical Simulation	91
4.4.1	PDMS-Glass Channels.....	91
4.4.2	Acrylic-Glass Channels.....	105
4.4.3	Comparison of EFT Results with Numerical Predictions	107
4.5	Summary	116
V	DUAL-TRACER FLUORESCENCE THERMOMETRY.....	118
5.1	Temperature Calibration for DFT Technique	118
5.1.1	Preparation of the working fluid	118
5.1.2	Experimental Setup and Procedures.....	119
5.1.3	DFT Calibration Results.....	121
5.2	DFT Results and Discussion.....	125
5.2.1	DFT Results in PDMS-Glass Channels	125
5.2.2	DFT Results in Acrylic-Glass Channels	134

5.3	Summary	144
VI	CONCLUSIONS AND RECOMMENDATIONS.....	146
6.1	Conclusions	146
6.1.1	Evanescent Wave Fluorescence Thermometry (EFT)	146
6.1.2	Dual-Tracer Fluorescence Thermometry (DFT).....	147
6.2	Contributions.....	149
6.3	Recommendations for Future Work	149
	REFERENCES	152

LIST OF TABLES

Table 3.1. Components of the illumination system used in the EFT studies.....	47
Table 3.2. Components of the volume illumination system	49
Table 3.3. Components of the imaging system for the EFT studies	54
Table 3.4. Components of the imaging system for the DFT studies.....	56
Table 4.1. A list of the aqueous fluorescent dye solutions tested for adsorption on borosilicate glass surface at various concentrations and pH values. In all cases, these dyes were tested in solution with fluorescein at molar concentrations between 5 and 50 $\mu\text{mol/L}$	72
Table 4.2. Nominal dimensions of the numerical model. All dimensions are in mm. ...	93
Table 4.3. Material properties at 25 $^{\circ}\text{C}$ used in the numerical simulations.....	100
Table 4.4. Average wall and fluid at $z = 0$ and 50 μm , respectively) temperature discrepancies between the 50 μm mesh and the 100 or 200 μm spatial resolution meshes in the channel near the ITO heater.	102
Table 4.5. Average temperature discrepancies in regions A, B, and C (<i>cf.</i> Figure 4.8) between EFT data and the numerical predictions at values of \dot{q}	110
Table 4.6. Similar to Table 4.5, but for acrylic-glass channels.	112

LIST OF FIGURES

Figure 2.1: A schematic diagram illustrating the processes involved in optical absorption and subsequent emission of fluorescence.	21
Figure 3.1. A schematic diagram of the absorption spectra as a function of excitation wavelength for FI at temperatures T_1 (dashed) and $T_2 > T_1$ (solid line). At $\lambda = 514$ nm (dotted line), the absorption at T_2 is greater than that at T_1	44
Figure 3.2. Plots of (a) absorption normalized by its maximum value and (b) emission normalized by its maximum value, both as a function of wavelength, for FI (black solid line) and SrB (blue dashed line). The arrows on both spectra indicate the excitation at 514 nm (and so only the portion of the emission spectrum to the right of this arrow will be emitted by FI and SrB). The shaded and hatched regions on the emission spectrum denote the wavelengths transmitted by the filter cubes that isolate the emissions from FI and SrB, respectively, in these experiments.	45
Figure 3.3. The illumination systems for the EFT experiments.	47
Figure 3.4. The illumination systems for the DFT experiments.	49
Figure 3.5. The normalized incident power as a function of the position of the razor blade when translating the knife-edge along the horizontal (<i>blue circles</i>) and vertical (<i>red squares</i>) directions. Two dotted lines represent 10 and 90% of the total beam power, respectively.	51
Figure 3.6. The output power from the argon-ion laser (543-MA-A03, Melles Griot) measured by the laser power meter as a function of time.	52
Figure 3.7. Sketch of the imaging systems used in the EFT studies.	54
Figure 3.8. Sketch of the imaging systems used in the DFT studies.	55
Figure 3.9. The emission intensities from FI and SrB as a function of concentration of the dye solution at two different exposure time, 1 and 20 ms.	57
Figure 3.10. A sample image of the scale marked in 20 μm increments obtained with the imaging system used for the DFT experiments.	58
Figure 3.11. A typical grayscale image of volumetrically illuminated 5 μM FI; flow goes	

from top to bottom in this image. The grayscale value V at a given laser power P was calculated by averaging the grayscale values for all the pixels inside the rectangular region (300×400 pixels) in the center of the channel.

..... 59

Figure 3.12. Camera calibrations showing the normalized incident laser power P_n as a function of the normalized grayscale value V_n for FI solutions at molar concentrations of $5 \mu\text{M}$ (*solid circles*) and $20 \mu\text{M}$ (*open circles*) excited at 514 nm at two different camera multiplication gain at $G_M = 2900$ (*circles*) and 3200 (*squares*) (*a*). Figure (*b*) shows the relationship between V_n and P_n at $5 \mu\text{M}$ (*open symbols*) and $20 \mu\text{M}$ (*closed symbols*) with two different dyes, FI (*circles*) and SrB (*squares*), at a EMCCD gain of 2700 . The standard deviation in all cases is smaller than the symbols. The dashed line in figure (*a*) represents $V_n = P_n$ 61

Figure 3.13. Camera response for images of $5 \mu\text{mol/L}$ and $20 \mu\text{mol/L}$ FI illuminated by volumetric (Vol) and evanescent wave (Eva) illuminations, respectively, at $G_M = 2700$. The standard deviation is smaller than the symbols. 62

Figure 3.14. Camera response curve showing the measured normalized incident power P_n as a function of the resultant normalized imaged grayscale value V_n (points) and a curve-fit to these data (dashed line) given by Eq. (3-6). 63

Figure 4.1: An illustration of Snell's law (*a*) and total internal reflection (TIR) (*b*) for the propagation of a ray of light near a glass-water interface. 68

Figure 4.2: Generation of evanescent waves from TIR at the interface between two media with different refractive indices, n_1 and $n_2 (>n_1)$ 69

Figure 4.3. Drawing of the positive master for the PDMS channel trench created by SolidWorks. The diameters of the inlet and outlet ports are 2 mm . The four pins protruding from the corners are used to connect the master with the rest of the PDMS mold. 75

Figure 4.4. The steps to fabricate the ITO heater on a glass substrate. (*a*) After cleaning the surface of the borosilicate glass substrates by plasma etching, the ITO film (nominal dimensions $6 \text{ mm} \times 1 \text{ mm} \times 300 \text{ nm}$) was deposited on the glass substrate through a metal mask containing the design of the heater configuration by the PVD75 RF sputterer. (*b*) Layers of conductive Ti, Cu

and Au (typical thicknesses of 50 nm, 4 μm , and 500 nm, respectively) were deposited on both sides of the ITO film in both sides to provide contact pads. (c) After cleaning impurities from the glass substrate by exposing it again to an induced plasma, a 500 nm thick silicon dioxide (SiO_2) layer was deposited over the ITO and Ti/Au/Cu layers to insulate the heater and most of the contact pads. (d) The PDMS block containing a negative relief of the channel was sealed onto the glass substrate after both were exposed to oxygen plasma. (e) Finally, electrical wires were soldered on the conductive layer to supply power to the ITO heater. 77

Figure 4.5. Top (a) and cross-sectional (b) views of the PDMS-glass channels with thin-film ITO heaters. The dotted rectangle in the top view and the thick dotted line the cross-sectional view represent the imaged region (IR). Flow goes from left to right in the top view, and out of the page in the side view, as indicated. All dimensions are given in mm. The two TCs are about 12 mm apart and placed roughly symmetrically upstream and downstream of the IR. 79

Figure 4.6. Representative 653×492 pixel ($160 \mu\text{m} \times 120 \mu\text{m}$) grayscale images (exp. 15 ms) from the EFT temperature calibrations of the emissions from FI excited by 514 nm light at $T = 20 \text{ }^\circ\text{C}$ [left] and $60 \text{ }^\circ\text{C}$ [right] at $Re = 67$. The yellow square indicates the 450×450 pixel ($150 \mu\text{m} \times 150 \mu\text{m}$) region processed in these images. 81

Figure 4.7. Plot of average normalized fluorescence intensity of the FI emissions for the EFT calibrations \bar{I} / \bar{I}_{20} as a function of solution temperature T . The overall change of the emission intensity was 1.8 % per $^\circ\text{C}$. Equation 4-6 is given by the solid line, and the error bars represent the standard deviations. 82

Figure 4.8. The three different regions, A, B, and C, imaged by the TIR microscope next to the bottom surface of the channel. The edge of region A is about $12 \mu\text{m}$ from the channel wall near heater, while the edge of C is about $12 \mu\text{m}$ from the opposite channel wall. Region B is in the center of the channel, and 0.408 mm from regions A and C. The flow goes from top to bottom, as shown, and all dimensions are given in mm. 84

Figure 4.9. Average images of FI emissions excited by evanescent wave at $T_{\text{ref}} = 20.2 \text{ }^\circ\text{C}$

	[left] and with a temperature gradient imposed by supplying 330 mW of electrical power to the ITO heater at $Re = 3.3$ [right]. Flow goes from top to bottom in the images.	84
Figure 4.10.	Pseudocolor temperature maps over regions (a) A, (b) B, and (c) C obtained in the PDMS-glass channel at $Re = 3.3$ at a spatial resolution of $1 \mu\text{m}$. The physical dimensions of all the regions are $120 \mu\text{m} \times 160 \mu\text{m}$	86
Figure 4.11.	Similar to the previous Figure, but at $Re = 8.3$	87
Figure 4.12.	Pseudocolor temperature maps over $120 \mu\text{m} \times 160 \mu\text{m}$ region at $12 \mu\text{m}$ apart from the wall near heater (a), at the center (b), and at $12 \mu\text{m}$ apart from the wall opposite to the heater (c) at a spatial resolution of $1 \mu\text{m}$ at $Re = 3.3$ in the acrylic-glass channel. The ring-like feature in the upper right and left corner in the image A and B is because the window for the light path to the camera port is not fully opened.	89
Figure 4.13.	Similar to the previous Figure, but at $Re = 8.3$	90
Figure 4.14.	Numerical models meshed in Gambit 2.2.30 of (a) the PDMS block, glass substrate and microscope stage and (b) just the PDMS block and glass substrate. Note that the magnification of (b) is greater than that for (a)....	92
Figure 4.15.	Detailed drawing of the numerical model consisting of the PDMS block and the glass substrate with the ITO heater and the Ti/Cu/Au conductive layer.	93
Figure 4.16.	(a) A top view of the numerical model and (b) a magnified view of the central portion of the channel, the ITO heater, and the conducting layer. The flow direction is from top to bottom in both views.	95
Figure 4.17.	Wall surface temperature T as a function of normalized channel coordinate y/L predicted by FLUENT at different heat generation rates corresponding to 100% (triangles), 90% (circles), and 80% (squares) of the electric input power at $Re = 3.3$	98
Figure 4.18.	Pseudocolor temperature map of the channel, ITO heater, and the surface of the glass substrate at $Re = 3.33$ for the PDMS-glass channel. The highest temperatures are in the region near the heater, while the edges of the glass substrate remain at room temperature.	103

Figure 4.19. Temperature distribution on the channel walls near the ITO heater at $Re = 3.33$ in the PDMS-glass channel. The temperatures at the bottom and top surfaces of the channel are about 50 °C and 33 °C, respectively.....	104
Figure 4.20. Detailed drawing of the numerical model of the acrylic-glass channel consisting of the acrylic block and the glass substrate with the ITO heater, the Ti/Cu/Au conductive layers, and the SiO ₂ layer. In the view shown, the channel trench is 4 mm to the left of the center of the acrylic block.	104
Figure 4.21. A magnified view of the central portion of the channel, the ITO heater and the conducting layer. The flow direction is from top to bottom in both views.	105
Figure 4.22. Temperature distribution over the channel wall near the ITO heater at $Re = 3.33$ in the acrylic-glass channel.	106
Figure 4.23. Temperature profiles T across the channel as a function of the normalized channel coordinate y/L measured by EFT (<i>triangles</i>) compared with FLUENT predictions at three different values of \dot{q} corresponding to 95% (<i>closed squares</i>), 93% (<i>circles</i>), and 91% (<i>open squares</i>) of the input electrical power. for $Re = 3.3$ (<i>a</i>) and 8.3 (<i>b</i>). The error bars on the EFT data, which are for the most part comparable to the size of the symbols, represent the experimental uncertainty.	108
Figure 4.24. Similar to Figure 4.23, but in acrylic-glass channels at values of \dot{q} corresponding to 97.5% (<i>filled squares</i>), 95.5% (<i>circles</i>), and 93.5% (<i>open squares</i>) of the input electrical power.	114
Figure 4.25. Pseudocolor map of wall surface temperatures (<i>i.e.</i> $z = 0$) from FLUENT at $0.93 q'''$ over $1 \text{ mm} \times 0.75 \text{ mm}$ region on the bottom surface of the PDMS-glass channel at $Re = 3.3$ (<i>a</i>) and 8.3 (<i>b</i>). Flow goes from top to bottom and the ITO heater is on the right. The dotted line across the image (<i>a</i>) in the center denotes the location of the temperature gradient compared to the EFT data in Figure 4.24.....	115
Figure 4.26. Similar to Figure 4.25, but with acrylic-glass channels at $0.935 q'''$	116
Figure 5.1. Top (<i>a</i>) and cross-sectional (<i>b</i>) views of the channels with thin-film ITO heaters. The dotted rectangle in the top view and two thick dotted lines the cross-sectional view represent the imaged region (IR) by the microscope	

objective. The thick dashed line in (a) denotes the centerline of the heater. Two parallel thin dashed lines in (b) represent the vertical extent of the laser light sheet used to illuminate the entire channel. Flow goes from left to right in the top view, and out of the page in the side view, as indicated. All dimensions are given in mm. 120

Figure 5.2. Typical 653×492 pixel ($954 \mu\text{m} \times 718 \mu\text{m}$) grayscale images at an exposure of 20 ms of FI [left] and SrB [right] at $T = 20^\circ\text{C}$ from the temperature calibrations. Note that these images, obtained within a few s of each other, are of the same solution imaged through different filters. The rectangle indicates the 650×300 pixel ($950 \mu\text{m} \times 440 \mu\text{m}$) region processed in these images. 122

Figure 5.3 Average normalized fluorescence intensity \bar{I} / \bar{I}_{20} as a function of solution temperature T for FI (*triangles*) and SrB (*circles*). The ratio of these two normalized intensities I' (*squares*) is also given as a function of T , along with a fifth-order polynomial curve-fit to these data (solid line), given by Eq. (5-1). 123

Figure 5.4. Temporally averaged images of the emissions from $5 \mu\text{M}$ FI [left] and SrB [right] volumetrically illuminated at $\lambda = 514 \text{ nm}$ in the heated PDMS-glass channels at $Re = 3.3$. Flow goes from top to bottom in the images. 126

Figure 5.5. Pseudocolor temperature map at $z = 14 \mu\text{m}$ over a $953 \mu\text{m} (y) \times 718 \mu\text{m} (x)$ region at a spatial resolution of $1.462 \mu\text{m}$ (1 pixel) at $Re = 3.3$ in the PDMS-glass channel. The flow goes from top to bottom in the images... 127

Figure 5.6. Pseudocolor maps of fluid temperatures measured by DFT at the depth of $z = 14 \mu\text{m}$ (a) and $z = 950 \mu\text{m}$ (b) at $Re = 3.3$ in the PDMS-glass channel. Both images are at a spatial resolution of $50 \mu\text{m}$ (34 pixels) and flow goes from top to bottom in the images. Note that the map shown in (a) is a spatial average of the previous Figure. The dotted line across these images and subsequent images in this Chapter denotes the location of the temperature profile compared to numerical predictions in Sec. 4.4.1..... 128

Figure 5.7. Pseudocolor map of the fluid temperature field at $z = 50 \mu\text{m}$ (a) and $z = 950 \mu\text{m}$ (b) predicted by FLUENT in PDMS-glass channels at $Re = 3.3$ with a heat generation rate corresponding to 93% of the input electrical power at a spatial resolution of $50 \mu\text{m}$. The ITO heater is on the right side of the

image and the flow goes from top to bottom.	130
Figure 5.8. Fluid temperatures T as a function of normalized channel coordinate y/L measured by DFT (<i>triangles</i>) compared with the predictions from FLUENT (<i>circles</i>) at $Re = 3.3$ (<i>a</i>) and 8.3 (<i>b</i>) in the PDMS-glass channel. Filled symbols denote fluid temperatures near the bottom wall at $z = 14 \mu\text{m}$ (DFT) and at $z = 50 \mu\text{m}$ (FLUENT), while open symbols represent fluid temperatures near the top wall at $z = 950 \mu\text{m}$. Both the numerical predictions and the DFT data are presented at a spatial resolution of $50 \mu\text{m}$. The error bars represent one standard deviation in the DFT results.	132
Figure 5.9 (<i>a</i>) A sketch of the acrylic-glass channel used in the DFT experiments and (<i>b</i>) a sketch illustrating how the channel was illuminated by the laser light sheet over the lower and upper portions of the channel over nominal locations $z \approx 0 - 400 \mu\text{m}$ and $z \approx 600 - 1000 \mu\text{m}$, respectively, as denoted by the hatched regions. As indicated by the arrows, the light sheet enters the channel through the side wall opposite the heater.	135
Figure 5.10. Temperatures predicted by FLUENT over the z -positions corresponding to the DFT results, or (<i>a</i>) from $z = 0$ to $400 \mu\text{m}$ and (<i>b</i>) from $z = 600 \mu\text{m}$ to $1000 \mu\text{m}$, as a function of y/L at a spatial resolution of $50 \mu\text{m}$ at $Re = 3.3$	137
Figure 5.11. Pseudocolor temperature maps measured by DFT (<i>a</i>) at $z = 14 \mu\text{m}$ compared to (<i>b</i>) the predictions of FLUENT averaged over $z = 0 - 400 \mu\text{m}$ at $Re = 3.3$ in the acrylic-glass. Both DFT and FLUENT results have a spatial resolution of $50 \mu\text{m}$. Flow goes from top to bottom and the heater is on the right in the images. The dotted line across image <i>a</i> in the center represents the location of the temperature profile compared to the numerical predictions later in this Section.	139
Figure 5.12. Pseudocolor temperature across the acrylic-glass channel (<i>a</i>) measured by DFT channel at $z = 950 \mu\text{m}$ compared to (<i>b</i>) the predictions of FLUENT averaged over $z = 600 - 1000 \mu\text{m}$ at a spatial resolution of $50 \mu\text{m}$ at $Re = 3.3$. The flow goes from top to bottom and the heater is on the right in the images. Note that the temperature scale for this Figure differs from that of the previous Figure.	140
Figure 5.13. Fluid temperatures T as a function of normalized channel coordinate y/L	

measured by DFT at $z = 14 \mu\text{m}$ (*filled triangles*) and $z = 950 \mu\text{m}$ (*open triangles*) compared with the predictions from FLUENT averaged over $z = 0\text{--}400 \mu\text{m}$ (*filled circles*) and $z = 600\text{--}1000 \mu\text{m}$ (*open circles*) at (a) $Re = 3.3$ and (b) $Re = 8.3$ in the acrylic-glass channel. All results are at a spatial resolution of $50 \mu\text{m}$. The error bars represent a standard deviation in the DFT results..... 143

NOMENCLATURE

Abbreviations

2D	Two Dimensional
3D	Three Dimensional
Ag	Silver
Au	Gold
CAD	Computer-Aided Design
CCD	Charge-Coupled Device
CFD	Computational Fluid Dynamics
Cu	Copper
CW	Continuous-Wave
DAQ	Data Acquisition System
DELIF	Dual Emission Laser-induced Fluorescence
DFT	Dual-tracer Fluorescence Thermometry
DI	Deionized
DDI	Distilled Deionized
EFT	Evanescent wave-based Fluorescence Thermometry
EMCCD	Electron Multiplication CCD
EOF	Electro-Osmotic Flow
Eva	Evanescent wave illumination
Fl	Fluorescein

Fl27	Fluorescein 27
FLIM	Fluorescence Lifetime Imaging Microscopy
FT	Fluorescence Thermometry
FWHM	Full Width at Half Maximum
HD	Hard Drive
HTC	Heat Transfer Coefficient
IC	Integrated Circuits
IEF	Iso-Electric Focusing
IR	Infrared
ITO	Indium-tin-oxide
ITRS	International Technology Roadmap for Semiconductor
LID	Low Image Density
LIF	Laser-induced Fluorescence
LOC	Labs-on-a-Chip
μ TAS	micro-Total Analysis Systems
MTT	Molecular Tagging Thermometry
MW	Molecular Weight
N ₂	Nitrogen gas
NA	Numerical Aperture
Ni	Nickel
Nu	Nusselt Number

OSSM	Optical Serial Sectioning Microscopy
PC	Personal Computer
PCR	Polymerase Chain Reaction
PDMS	Polydimethylsiloxane
PIT	Particle-image Thermometry
PTT	Particle Tracking Thermometry
Ra	Rayleigh number
Re	Reynolds number
RhB	Rhodamine B
RhB110	Rhodamine 110
RIE	Reactive-Ion Etcher
RTD	Resistive Temperature Detector
SiO ₂	Silicon Dioxide
SrB	Sulfo-rhodamine B
SrB101	Sulfo-rhodamine B 101
SThM	Scanning Thermal Microscopy
TC	Thermocouple
TGF	Temperature Gradient Focusing
Ti	Titanium
TIM	Thermal Interface Materials
TIRF	Total Internal Reflection Fluorescence
TLC	Thermochromic Liquid Crystal

UV	Ultra-Violet
Vol	Volumetric Illumination

Greek Letters

ε	Extinction coefficient
λ	Wavelength
λ_{em}	Emission wavelength
λ_{ex}	Excitation wavelength
μ	Micron (10^{-6} m) or dynamic viscosity of water
ν	Fluid kinematic viscosity
ν_{EX}	Frequency of excitation
ν_{EM}	Frequency of emission
θ_i	Incident angle of the evanescent waves
θ_c	Critical angle of the evanescent waves
ρ	Density
σ	Standard deviation
τ	Time when the intensity drops to $1/e$
Φ	Quantum efficiency

Symbols

A	Collection efficiency of the imaging system
---	---

A_s	Surface area of thin film
C	Dye concentration
c_p	Heat capacity
e	Smallest resolvable distance of the imaging system
h	Planck's constant or convective heat transfer coefficient
f	Focal length of the objective
g	Temperature-dependent function
G_M	Multiplication gain of the CCD camera
I	Intensity
\bar{I}	Average Intensity
I'	Normalized intensity
I_o	Initial intensity of laser beam
I_f	Fluorescence intensity
k	Thermal conductivity
L	Optical pathlength
M	Magnification
n	Refractive index
P	Actual incident power on the CCD
P_n	Normalized actual incident power on the CCD
\dot{q}	Volumetric heat generation rate in the ITO heater
Q	Volume flow rate

r	radial distance from the central axis of the laser beam
R	Distance between the laser beam and the central axis of the TIRF microscope objective or Thermal Resistance
R^2	Coefficient of determination
R_a^2	Adjusted coefficient of determination
t	Thickness of thin film
T	Temperature
T_{in}	Inlet temperature
T_{ref}	Reference temperature
V	Volume of the fluorescent solution
V_n	Normalized grayscale value of a CCD pixel
V_d	Grayscale value of a CCD pixel corresponding to the dark noise of the camera
y/L	Normalized distance across the channel
w	Diameter of the laser beam
δz	Depth of Field
z_p	Penetration depth

SUMMARY

Thermal management challenges for microelectronics are a major issue for future integrated circuits, thanks to the continued exponential growth in component density described by Moore's Law. Current projections from the International Technology Roadmap for Semiconductors predict that local heat fluxes will exceed 1 kW/cm^2 within a decade. There is thus an urgent need to develop new compact, high heat flux forced-liquid and evaporative cooling technologies.

Thermometry techniques that can measure temperature fields with micron-scale resolution without disturbing the flow of coolant would be valuable in developing and evaluating new thermal management technologies. Specifically, the ability to estimate local convective heat transfer coefficients, which are proportional to the difference between the bulk coolant and wall surface temperatures, would be useful in developing computationally efficient reduced-order models of thermal transport in microscale heat exchangers.

The objective of this doctoral thesis is therefore to develop and evaluate non-intrusive optical thermometry techniques to measure wall surface and bulk liquid temperatures with $O(1-10 \text{ }\mu\text{m})$ spatial resolution. Intensity-based fluorescence thermometry (FT), where the temperature distribution of an aqueous fluorescent dye solution is estimated from variations in the fluorescent emission intensity, was used to measure temperatures in steady Poiseuille flow at Reynolds numbers less than 10. The flow was driven through 1 mm square channels heated on one side to create temperature gradients exceeding $8 \text{ }^\circ\text{C/mm}$ along both dimensions of the channel cross-section. In the evanescent-wave fluorescence thermometry (EFT) experiments, a solution of fluorescein was illuminated by evanescent waves to estimate the solution temperature within about 300 nm of the wall. In the dual-tracer FT (DFT) studies, a solution of two fluorophores with opposite temperature sensitivities was volumetrically illuminated over most of the

cross-section of the channel to determine solution temperatures in the bulk flow. The accuracy of both types of FT is determined by comparing the temperature data with numerical predictions obtained with commercial computational fluid dynamics software. The results indicate that EFT can measure wall surface temperatures with an average accuracy of about 0.3 °C at a spatial resolution of 10 μm, and that DFT can measure bulk water temperature fields with an average accuracy of about 0.3 °C at a spatial resolution of 50 μm in the image plane. The results also suggest that the spatial resolution of the DFT data along the optical axis (*i.e.*, normal to the image plane) is at least an order of magnitude greater than the depth of focus of the imaging system.

CHAPTER 1

INTRODUCTION

1.1 Motivation

The development of microfabrication techniques over the past few decades has enabled miniaturization of a variety of devices, including conduits for the flow of liquids and gases. These techniques have made possible the new field of microfluidics, or the transport and analysis of fluids through small channels fabricated in silicon and other materials with overall dimensions of $O(10\ \mu\text{m} \sim 100\ \mu\text{m})$. Controlling transport through such microchannels has become an important technology in applications such as biochemical sample preparation and analysis, drug delivery, thermal management of microelectronics (and other types of electronics) and energy systems such as miniature internal combustion engines. The majority of microfluidic applications involve incompressible flow, so the velocity and temperature fields are the most important flow properties in most microscale flows. Although there has been a great deal of work on velocity measurement at the micro- to nanometer scales (Santiago *et al.*, 1998 and Zettner and Yoda, 2003), there has been far less work on microscale thermometry.

The study of thermal transport at $O(1\text{--}10\ \mu\text{m})$ spatial scales is motivated by the development of micro-total analysis systems (μTAS) or Labs-on-a-Chip (LOC). These microfluidic systems, which shrink the capabilities of an analytical or biochemistry lab onto a single “chip” a few centimeters across, have major advantages in that they can reduce sample and analyte consumption, separation and assay times, and equipment and personnel costs.

In most LOC, aqueous solutions of ions and biomolecules are pumped through

channels with overall dimensions of $O(10\text{--}100\ \mu\text{m})$. Monitoring and accurately measuring the temperature of these solutions is important in applications such as controlling chemical reaction kinetics and avoiding degradation of biomolecules. In capillary electrophoresis, for example, an electric field is used to separate biomolecules in an aqueous buffer solution based on differences in the electrophoretic mobilities of the biomolecules. The applied electric field can however also lead to Joule (ohmic) heating, and controlling buffer temperature is critical in minimizing protein folding and denaturation (Rush *et al.*, 1991). Implementing the polymerase chain reaction (PCR) commonly used for DNA replication in a continuous-flow LOC also requires controlling and changing the temperature of the DNA sample over different regions of the chip to optimize the performance of the reaction (Kopp *et al.*, 1998).

Temperature control is important as well in isoelectric focusing (IEF), an electrophoretic method in which either positively or negatively charged molecules such as proteins, enzymes, and peptides are separated on the basis of their isoelectric point (pI), the pH at which a molecule carries no net electrical charge (Huang and Pawliszyn, 2002). Separation of molecules takes place in a pH gradient created by Joule heating. As the molecules migrate to the pH region that corresponds to their pI (the molecules remain in that region because they have zero net charge there and hence experience no electrical forces that would transport them to other regions), the various molecules become concentrated, or focused, in different stationary regions, or bands. Fine control of solution temperature, and thereby the pH gradient, determines the separation efficiency. Although IEF is limited to analytes with a limited range of pI and the low solubility of most proteins at their pI, temperature gradient focusing (TGF) can be used instead to separate a wider variety of analytes (Ross and Locascio, 2002). In TGF, a temperature gradient is used to focus analytes in different regions or bands by balancing the electrophoretic velocity of a given analyte with the bulk velocity of the buffer solution

containing the analyte. Fine control of temperature in TGF also therefore determines the focusing efficiency. Unlike IEF, TGF can be used for any charged analyte (in solution) and is not limited to molecules with a specific range of pI.

Electronic cooling is another important motivation for measuring temperatures at the microscale. As the density of transistors has increased exponentially over the past half-century, as described by Moore's Law, integrated circuits (ICs), dissipating the heat generated by these transistors over a limited area has led to huge thermal management challenges. At present, average heat fluxes on ICs are projected to exceed 100 W/cm^2 for high-performance chips at the 14 nm of feature size within a decade (ITRS 2009), and local peak heat fluxes are projected to exceed 500 W/cm^2 . Since the reliability of electronic components decreases as their temperature increases—as a rule of thumb, the failure rate doubles for every 8–10 °C rise in their temperature (Blanks, 1980)—cooling microelectronics and managing such high heat fluxes is a major challenge for “next generation” microelectronic devices.

One commonly used solution to this thermal management problem is to cool the entire IC. At present, heat sinks using forced-air cooling that are usually at least as large as the entire IC are attached to the IC by a heat spreader using various thermal interface materials (TIMs). This thermal packaging has the disadvantages that it results in a large thermal resistance between the chip and its surroundings and limits the chip packing density on the substrate, thereby increasing the length of the connections between chips. These longer interconnects are associated with higher latency, increased power dissipation, and greater losses. Even with the latest advances in heat sinks, forced-air cooling cannot effectively dissipate the heat flux values projected over the next decade and so cannot maintain the next generation of ICs at their specified operating junction temperatures.

Future IC designs will therefore require new thermal management technologies

beyond forced-air convection. Single-phase forced liquid (Tuckerman and Pease, 1981) and two-phase evaporative (Hidrovo *et al.*, 2006) cooling are both promising alternatives because they can accommodate much higher heat loads. Furthermore, as the overall size of the ICs becomes smaller, the size of the cooling channel should also become smaller. To accommodate these projected heat flux values, a microchannel heat sink with a footprint of a few square centimeters will require a three-dimensional network of up to several hundred microchannels connected by numerous manifolds. The mainly steady, laminar and fully-developed flows in such networks can of course be numerically simulated, giving accurate estimates of the thermal performance of microchannel heat sinks. Nevertheless, these computations require significant time because of the geometric complexity of the networks and are further complicated by spatial variations in the heat flux incident upon the heat sink due to chip “power maps,” or the variations in the power dissipated by the IC because it is comprised of a variety of materials with different thermal properties.

An alternative approach to designing heat sinks that force liquid-phase coolant through a complex array of microchannels is to use reduced-order modeling of these networks based on local heat transfer correlations. By Newton’s Law of Cooling, the local heat flux q'' normal to the wall is proportional to the difference between the local surface and mean (bulk) fluid temperatures T_s and T_m , respectively.

$$q'' = h(T_s - T_m) \quad (1)$$

where h is the local convective heat transfer coefficient (HTC). Developing local heat transfer correlations for various geometries therefore requires accurate measurements of the wall and mean (bulk) fluid temperatures.

Although a variety of techniques such as infrared thermometry, surface-mounted micro-resistance temperature detector and temperature-sensitive diode arrays (Jang *et al.*,

2003 and Han and Kim, 2008), and even temperature-sensitive surface layers (Samy *et al.*, 2008) have been used to measure T_s , these are not appropriate for measuring coolant temperatures since they disturb the flow of coolant. Moreover, resistance and diode temperature sensors can only measure temperatures at a single point. Measuring temperatures at multiple points is of course feasible using an array of such sensors, but fabricating such an array is quite involved. Thus, there are few practical techniques that can accurately measure mean fluid temperature fields with micron-scale resolution without disturbing the flow of coolant.

The aim of this thesis is to develop and apply non-intrusive liquid-phase thermometry techniques where liquid temperatures are determined from variations in the intensity of fluorescent and/or photoluminescent tracers dissolved or suspended in the liquid with $O(1 \mu\text{m})$ spatial resolution. These techniques can be used to determine local heat transfer correlations in microchannel arrays that consider thermal coupling between the channels for reduced-order modeling and to evaluate the performance of new thermal management technologies.

The specific research objectives of this doctoral thesis are to:

- Develop dual-tracer fluorescence thermometry to measure 2D liquid-phase coolant temperature fields with a spatial resolution of $O(1 \mu\text{m})$;
- Use fluorescence thermometry with evanescent-wave illumination to measure liquid-phase temperatures well within $1 \mu\text{m}$ of the wall, or effectively the wall surface temperature distribution;
- Evaluate and apply these thermometry techniques by estimating local heat transfer coefficients in steady laminar Poiseuille flow through a heated channel;
- Quantify the accuracy of these techniques by comparing the experimental data with numerical predictions from the commercial computational fluid dynamics

(CFD) software package FLUENT.

1.2 Thermal management in ICs

A major application of these techniques is in thermal management for microelectronics, since the performance and reliability of ICs is a strong function of their operating temperatures. This section briefly summarizes current thermal management issues on electronic devices. .

As feature size decreases and package density increases, ICs are quickly reaching their maximum allowable temperatures. Overheating the circuits by operating above this maximum value leads to slower operation and device failure. For example, the mean-time-to-failure due to electro-migration effects decreases exponentially as temperature increases (Tsai and Kang, 2000). Tsai and Kang showed that the current drive capability of metal-oxide-semiconductor transistors, which determine the switching time of transistors between turn-on and turn-off operations, decreases about 4% for every 10 °C increase in temperature, while interconnect delays, which reduce the circuit speed, increase approximately 5% for every 10 °C increase. Cheng *et al.* (1998) demonstrated that the combination of an increase in operating temperature and a nonzero temperature gradient from poor circuit design caused logic faults that led to the malfunction of the entire device. Gurrum *et al.* (2004) showed that the non-uniform temperature distributions lead to a clock skew, or a loss of synchronization in the clock signal between electronic components. Moreover, higher operating temperatures can increase the thermal fatigue per cycle for certain materials and thereby speed up thermally-driven failures such as corrosion, cracking, and void formation.

In particular, interconnect performance and reliability decrease as the operating temperature increases. The resistivity of metal interconnect increases with temperature, decreasing signal propagation speeds and leading to Joule heating that generates an

additional increase in the interconnect temperature (Ajami *et al.*, 2005). More importantly, these temperature-induced effects combine to cause circuit failure (Joshi *et al.*, 2003).

Numerous ways to dissipate heat and remove it from the appropriate regions to maintain electronic devices within their desired operating temperature range have therefore been developed over the last thirty years. The most common thermal management technologies include single-phase liquid cooling, two-phase evaporative cooling, thermosyphons, and heat pipes.

Tuckerman and Pease (1981) first introduced forced-liquid cooling using microchannels, and showed that this could dissipate more heat than conventional forced-air cooling. Vafai and Zhu (1999) proposed a two-layered microchannel heat sink with countercurrent flow to reduce the temperature gradient along the axial direction. Their analysis of the thermal performance and temperature distribution showed that the streamwise temperature rise over the partially-heated base surface was significantly reduced about 300% less for the two-layered design than for a single layer design. Wei *et al.* (2007) fabricated stacked microchannel heat sinks composed of micro-fabricated networks of three-dimensional (3D) microchannels that featured both counter- and parallel flow to maximize the flexibility of the design. Their results showed that the total thermal resistance, defined as the ratio of the maximum temperature difference to the input power, for a counterflow at a flow rate of $1.38 \times 10^{-6} \text{ m}^3/\text{s}$ produced a 13 % higher thermal resistance than a parallel flow arrangement at the same flow rate. The difference between the two configurations at a higher flow rate of $5.83 \times 10^{-6} \text{ m}^3/\text{s}$ was, however, negligible. Overall thermal resistances of less than $0.1 \text{ }^\circ\text{C}/\text{W}$ were achieved for both counter- and parallel flow, suggesting that this design was a significant improvement over the forced-air cooling used at present.

The main limitation of single-phase cooling is the large pressure drop across the

flow channel associated with an increase in heat transfer rate either due to the increase in flow rate or the reduction in hydraulic diameter. Since evaporative cooling using a coolant with a high latent heat of vaporization can achieve much higher heat dissipation rates than single-phase liquid cooling at similar flow rates, several studies have been conducted to explore two-phase flow characteristics in the channel. Peng and Wang (1993) experimentally investigated the flow boiling of subcooled water flowing through a $0.6 \text{ mm} \times 0.7 \text{ mm}$ rectangular microchannel. They showed that nucleate boiling and heat transfer performance were enhanced in microchannels compared to normally-sized channel. Jiang *et al.* (1999) examined the boiling process in microchannel heat sinks with channel hydraulic diameters $D_h = 40 \text{ }\mu\text{m}$ and $80 \text{ }\mu\text{m}$ and observed different phase-change mechanisms for different channel diameters. The same authors later studied boiling mechanisms in microchannel with D_h as small as $26 \text{ }\mu\text{m}$ by flow visualization and 2D temperature field measurements along the streamwise direction at the centerline during forced-convection boiling experiments (Jiang *et al.*, 2001).

Furthermore, Koo *et al.* (2005) numerically simulated the performance of a 3D microchannel network for cooling ICs, and predicted a heat removal capacity as great as 135 W/cm^2 within a 3D architecture at a maximum circuit temperature of $85 \text{ }^\circ\text{C}$. Hidrovo *et al.* (2006) focused on understanding of two-phase boiling flows in microchannel for IC cooling as well as flow behavior and transport for liquid water management in fuel cell applications. For flow at a flow rate of 0.1 mL/min through a single $50 \text{ }\mu\text{m}$ -wide by $70 \text{ }\mu\text{m}$ -deep by 20 mm -long microchannel heated by an aluminum heater, they claimed that two-phase flow of water could be obtained at 2.12 W of input power to the heater based on temperature measurements in the channel, since the temperatures exceeded $100 \text{ }^\circ\text{C}$, indicating the presence of water vapor. However, only single-phase liquid flow was observed at lower input powers of 1.32 W or less, and the pressure drop across the channel initially decreased as the input power increased, though larger input powers did

increase the pressure drop. Koo *et al.* conjectured that increase in pressure drop corresponded to the onset of boiling, resulting in phase change requiring higher pressures to accelerate the low-density vapor to maintain constant mass flux.

An alternative cooling technique, the “digital microfluidic” platform, manipulates discrete droplets using electrowetting (*i.e.*, dynamic modification of the wetting properties of a dielectric surface by applying an electric field). Paik *et al.* (2008) showed that a large number of discrete water drops of volumes ranging from microliters to nanoliters could be used to reduce the temperatures of hot spots initially at 70–90 °C by up to 60 °C.

Over the last three decades, heat pipes have been a leading thermal management technology due to advantages such as no moving parts, lower pressure drop, cost-effectiveness (compared with other technologies), and compactness. Heat pipes are sealed pipes or tubes made of high thermal conductivity materials such as copper or aluminum with an inner lining of wick-like capillary material and a small amount of working fluid at pressures below ambient. They remove heat by vaporizing liquid by absorbing heat at the hot end, then returning the resulting vapor to the cold end by Continuity, where it condenses, then driving the resulting liquid back towards the hot end, where the cycle starts all over again, through the pores in the wick by capillary pressure.

More recently, a number of studies have considered micro heat pipes (Mallik and Peterson, 1995, Tsai *et al.*, 2004), where the wick is replaced by an array of microchannels. Mallik and Peterson (1995) experimentally investigated the cooling performance of vapor-deposited micro-heat pipe arrays of 34 and 66 pipes occupying 0.75% (A) and 1.45 % (B), respectively, of the cross-sectional area occupied by the heat pipe over entire silicon substrate at steady-state condition. Micro-heat pipe configurations A and B reduced the maximum surface temperature by 24.4% and 29%,

respectively, and the temperature gradient across the chip by 27.4% and 41.7%, respectively. Furthermore, the effective thermal conductivity of configuration B was improved by up to 47.1. The same authors subsequently studied the transient thermal response of the same heat pipe (Peterson and Mallik, 1995). Their results showed that silicon (Si) wafers cooled by micro heat pipe arrays reduced thermal time constants by up to 30–45% compared with values for Si wafers without micro heat pipes, due presumably to the enhancement in effective thermal conductivity caused by the phase change occurring in the micro heat pipe array.

Recently heat pipes using nanofluids, or nanoparticle suspensions, have been studied by a number of groups. Tsai *et al.* (2004) studied nanofluids containing 2–75 nm diameter gold nanoparticles suspended in deionized water at five different volume fractions in commercially available circular heat pipes made of copper with a length of 170 mm and an outer diameter of 6 mm. The thermal resistance of the heat pipes ranged from 0.17 °C/W to 0.215 °C/W for different particle sizes, and the thermal resistance of the heat pipe with nanofluids was lower than those with pure deionized (DI) water. Kang *et al.* (2006) used a 1–100 mg/L nanofluid containing 35 nm diameter silver nanoparticles in pure water in 211 μm ×217 μm deep grooved circular heat pipes and showed that the nanofluid reduced wall temperatures up 1.5 °C under various heat loads from two 120 W heaters compared with pure water. They also obtained an 80% reduction in thermal resistance compared with the same heat pipe using DI water.

Two-phase thermosyphons consisting of an evaporator and a condenser have also been used to cool microelectronic devices. Thermosyphons differ from heat pipes in two ways: 1) unlike heat pipes, they have no wicks and hence rely on gravity (*vs.* capillary forces) to return the condensate to the evaporator; and 2) thermosyphons depend, at least initially, on nucleate boiling, whereas heat pipes vaporize the fluid from a large interface between liquid and vapor. Thermosyphons often therefore require a significant

temperature difference to initiate boiling. Pal *et al.* (2002) used a two-phase thermosyphon to cool the microprocessor of a Hewlett-Packard Vectra VL800 desktop computer and was able to dissipate more than 50% of the total power consumed by CPU.

Evaluation of the cooling performance of such devices, however, is mainly determined by the heat flux or heat transfer coefficient calculated from the wall surface and fluid temperatures. These temperatures are also used to determine the thermal resistance and the heat removal rate. Therefore, accurate temperature data are important in evaluating and designing new thermal management technologies and in quantifying the thermal management requirements of microelectronic devices. Beyond the importance of accurate measurements for wall and bulk fluid temperatures, it is also important to accurately measure temperatures at finer spatial resolutions since the heat transfer in channel flows usually increases as the overall size of the channel decreases. The next section briefly summarizes the literature about heat transfer characteristics of microchannel flows.

1.3 Why can microchannel flows efficiently cool electronic circuits?

In most cases, the hydraulic diameter of a microchannel is small enough that the flows through such channels are laminar. In fully-developed laminar single-phase flow, the Nusselt number (Nu), a dimensionless number defined as the ratio of the convective heat transfer to the conductive heat transfer across the boundary, is constant for a given heat flux or temperature on the boundary:

$$Nu = \frac{hD}{k} = \text{constant} \quad (2).$$

For constant Nu , the convective heat transfer coefficient h will in general increase as the channel hydraulic diameter D decreases for otherwise identical boundary conditions at fixed thermal conductivity of the fluid, k (Wang *et al.*, 1994). The friction factor f , which

is the nondimensional pressure drop, in fully-developed laminar flow varies inversely with Re , and the pressure drop is inversely proportional to D^4 in laminar fully-developed flows. Increasing h by decreasing D is therefore associated with a severe penalty in terms of increased pressure drop.

A similar analysis also applies for turbulent flows. In both laminar and turbulent flows, the two parameters of interest are then the heat transfer coefficient and the friction factor. Most of studies about microchannels in the literature report these two parameters, how the values of these parameters may or may not deviate from classical theory, and the effect of these parameters on heat transfer performance. Overall, the literature is inconclusive regarding how a decrease in the characteristics length of the channel affects heat transfer performance. The next few paragraphs summarize the somewhat inconclusive previous studies on the heat transfer characteristics of microchannels in single- and two-phase flow.

An early investigation of heat transfer in microchannels using single-phase flow was conducted by Wu and Little (1984), who studied the flow of nitrogen gas through rectangular channels with hydraulic diameters around $150\ \mu\text{m}$. They found that the transition from laminar to turbulent flow occurred at lower Re than for larger, macroscale, ducts. For most Re , the HTC were found to be higher than expected from classical theory although Wu and Little did not report actual numerical values for h . Peng and Peterson (1995) investigated heat transfer and pressure drops in water flowing through arrays of rectangular microchannels with different aspect ratios for $D = 200\text{--}800\ \mu\text{m}$ at $Re = 50\text{--}4000$. They also found that transition to turbulence occurred at lower Re than at the macroscale, and that h more than doubled as the cross-sectional dimensions of microchannel decreased from $800\times 700\ \mu\text{m}^2$ to $200\times 700\ \mu\text{m}^2$. Peng and Peterson explained their observations by suggesting that heating such small channels creates a large change in the liquid temperature and hence a dramatic change in the thermophysical

properties of the flowing liquid, enhancing heat transfer.

Zhuang et al. (1997) then studied convective heat transfer due to impingement flow of transformer oil ($Pr = 200\text{--}400$) and the dielectric coolant FC-72 ($Pr = 15$) in two-dimensional microchannels at $Re = 70\text{--}4807$. Their experimental data showed $\sim 120\%$ and 225% enhancement of local Nu for both fluids compared with classical predictions and also suggested that the average HTC was at least six times greater than expected for similar macroscale flows. Adams et al. (1998) carried out experiments on the turbulent, single-phase forced convection of water flowing through circular channels of diameters $100\ \mu\text{m}\text{--}1.09\ \text{mm}$ and found both h and Nu were higher than values predicted by standard correlations, reporting Nu values that were up to 2.5 times the predictions from the Gnielinski correlation at $Re = 2 \times 10^4$. Jiang et al. (2001) measured volumetric heat transfer coefficients in a channel of nominal width and depth of $200\ \mu\text{m}$ and $600\ \mu\text{m}$, respectively, in micro-heat-exchangers with either microchannels or porous media. The volumetric heat transfer coefficients for water flowing through the micro-heat-exchangers with microchannels were as much as 10^4 times greater than the values for conventional plate heat-exchangers. However, the HTCs for a heat exchanger with a porous medium had a HTC that was only double that of the design with microchannels alone, presumably due to the enhanced thermal transport in the porous medium, and this improvement in thermal performance came at the cost of higher pressure drops.

Other studies have reported instead that h and Nu in microchannel flows are lower than the values predicted by classical correlations. Harms et al. (1999) examined the single-phase forced convection of water flowing through 68 parallel rectangular microchannels approximately $1000\ \mu\text{m}$ deep and $251\ \mu\text{m}$ wide at $Re = 173\text{--}12900$, and reported that although their experimentally determined Nu for turbulent flows agreed reasonably well with conventional theory, Nu was significantly lower than theoretical values for laminar flow. Qu et al. (2000) investigated the heat transfer characteristics of

water flowing through trapezoidal silicon microchannel with hydraulic diameters ranging from 62–169 μm at $Re = 100\text{--}1500$. and reported roughly constant Nu values when a constant heat flux was applied over one side wall. However, the absolute Nu at a given Re was around 75% lower than that predicted by conventional theory. The authors suggested that this discrepancy may be caused by surface roughness since the presence of the surface roughness will influence the momentum transfer near the wall, which will further affect the laminar velocity profile. Gao et al. (2002) measured HTC's in water flowing through a channel 25 mm \times 82 mm \times 0.1–1mm with an adjustable height e at $Re = 200\text{--}6000$. They observed that while the local Nu followed the classical laws for $e > 0.4$ mm, a significant decrease of the Nu was observed for lower values of e , e.g., for $e = 0.1$ mm, Nu was about 60 % smaller than the conventional value.

Despite these contradictory results on the heat transfer characteristics of microchannel flow, some researchers have investigated using single-phase flow through microchannel arrays to cool electronic devices and reported heat removal rates of 100–600 W/cm^2 . Roy and Avanic (1996), who designed and tested low-cost, high heat flux heat exchangers composed of copper tubing with cross-sectional dimensions of 125–500 $\mu\text{m}\times$ 12 mm, used their designs to cool high power (of the order of 1000 W/cm^2) semiconductor laser diode arrays at water flow rates up to 2×10^{-4} m^3/s . These heat sinks could dissipate 200–300 W from a solder bonded resistor about 500 μm^2 in area while limiting the surface temperature rise to 20–30 $^\circ\text{C}$. Aranyosi et al. (1997) used air-cooled heat sinks, composed of two microchannels, two wire screens, and porous metal fiber, for spot cooling of power packages and dissipated a heat flux of 15 W/cm^2 at an air flow rate of 20 g/s, corresponding to a fivefold enhancement in heat removal capability compared with traditional forced air-cooling schemes. Gillot et al. (2000) fabricated 3D multichip heat sinks composed of microchannel arrays and demonstrated that these heat sinks could dissipate power densities from 230 to 350 W/cm^2 with a temperature rise of 35 $^\circ\text{C}$ in

microchip modules. Perret et al. (2000) investigated the performance of water-cooled microchannel heat sinks embedded in a Si substrate, and reported heat removal rates as high as 100 W/cm^2 at an increase of the junction temperature of $60 \text{ }^\circ\text{C}$.

The heat transfer in two-phase flow in microchannels has not been studied as extensively as that in single-phase flow, but the literature on heat transfer characteristics for this case is also inconsistent. Peng and Wang (1993) experimentally studied the boiling heat transfer characteristics for subcooled water flowing through $600 \mu\text{m} \times 700 \mu\text{m}$ microchannels at $Re = 1600\text{--}6000$. Their results indicated that the single-phase convection and flow boiling characteristics are quite different from those observed in larger macroscale ducts. For example, the convective heat flux in the laminar or transitional regime at $Re = 1600\text{--}6000$ in their microchannels was at least comparable to the values for turbulent flow at $Re = 5090\text{--}9160$ in macroscale ducts. Bowers and Mudawar (1994) measured pressure drops and critical heat flux values for R-113 flowing through $D = 2.54 \text{ mm}$ and $510 \mu\text{m}$ channel heat sinks that were heated over 1 cm of the channel. Flow boiling using R-113 in mini- and microchannel heat sinks resulted in high heat fluxes exceeding 200 W/cm^2 at low flow rates ($Q < 65 \text{ mL/min}$) and pressure drops ($\Delta P = 0.32 \text{ Bar}$) compared with single-phase microchannel heat sinks, where a pressure drop of 1 Bar was required to achieve a heat flux of 181 W/cm^2 using water (Tuckerman and Pease, 1981).

Some researchers have also investigated whether the cooling performance of two-phase microchannel flows can be further enhanced by surface modification of the channel wall or by injecting noncondensable gas bubbles. Adams *et al.* (1999) studied the effect of dissolved noncondensables on convection heat transfer coefficients for subcooled forced-flow cooling of water through $760 \mu\text{m}$ diameter microchannels at $Re = 5000\text{--}23000$. The presence of dissolved air was found to increase the heat transfer coefficients by as much as 17% compared with an otherwise identical case with no

dissolved air, even though the maximum increase in the coolant velocity due to the noncondensable release was only a few percent. Khanikar *et al.* (2009) modified the bottom wall of a rectangular $370\ \mu\text{m} \times 44.8\ \text{mm}$ microchannel with $60\ \text{nm}$ diameter carbon nanotubes (CNT) to see if the CNT would enhance heat transfer. They observed that water flowing through the channel with CNT had a greater HTC than a channel of the same size without CNT, and hypothesized that this enhancement was due to the CNT arrays both increasing the heat transfer area and serving as very high conductivity fins. Fang *et al.* (2010), who evaluated how wall hydrophobicity affects condensation in microchannels, studied the condensation of steam in silicon microchannels with a hydraulic diameter of $286\ \mu\text{m}$ and different wall hydrophobicities. Although no quantitative comparisons were reported, they observed that the hydrophobic microchannel had both higher heat transfer rates and pressure drops compared with the hydrophilic channel for the same inlet vapor flux and inlet temperature.

On the other hand, there are a few studies reporting smaller heat transfer rates at the microscale, compared to those at the macroscale. For example, Lee and Mudawar (2008) measured both the pressure drop and heat transfer characteristics of the two-phase flow of water through channels with hydraulic diameters of $176\text{--}416\ \mu\text{m}$. Their results showed that while smaller hydraulic diameters tend to enhance two-phase cooling performance by increasing both mass velocity and wetted area, they can also trigger early transition from bubbly to slug flow, and thereby reduce cooling effectiveness.

In summary, the data reported in the literature are inconclusive for h and Nu in the flow in microchannels. To some degree, these deviations are caused by the difficulties in measuring the parameters necessary for the appropriate theoretical calculations (Palm, 2001). For example, it is often difficult to nonintrusively measure the bulk fluid and wall surface temperatures simultaneously, and these two parameters are necessary for determining h and Nu . The small dimensions of the test section also makes temperature

measurements difficult. However, the majority of the literature has shown that the smaller channels are associated with enhanced heat transfer rate. Accurate thermometry techniques at the microscale would help to accurately quantify the improvement in heat transfer for such microchannel flows. Accurate measurements of bulk and wall temperature distributions may also help explain why the heat transfer characteristics in microchannels deviate from classical theory.

CHAPTER 2

Literature Review

The primary objective of this thesis is to develop non-intrusive liquid-phase thermometry techniques to, if possible, simultaneously measure bulk fluid and wall surface temperatures with a spatial resolution of $O(1 \mu\text{m})$. This chapter reviews current thermometry techniques for measuring both bulk fluid temperatures and wall surface temperatures, and their respective advantages and disadvantages.

2.1 Liquid-Phase Thermometry

This section discusses thermometry techniques for measuring bulk fluid temperatures and their respective strengths and weaknesses. The techniques described here include temperature-sensitive laser-induced fluorescence (LIF), thermochromic liquid crystal (TLC) thermometry, and particle-image thermometry (PIT).

2.1.1 Laser-Induced Fluorescence Thermometry (FT)

Perhaps the most commonly used liquid thermometry methods are based on laser-induced fluorescence (LIF), which can be used to characterize passive scalar concentration as well as temperature fields (Nakajima *et al.*, 1990). Liquid temperatures are estimated based on changes in the lifetime or intensity of the emissions from fluorescent or phosphorescent species dissolved in the liquid.

The intensity of a laser beam (I_o) propagating through an absorbing medium diminishes along its line of propagation. As described by the Beer-Lambert law, the intensity of a beam of light with an initial intensity I_o will be reduced by absorption when it passes through a small distance dz of a solution of fluorescent dye of molar concentration C as follows:

$$\frac{dI_o}{I_o} = -\varepsilon C dz \quad (2-1)$$

where ε is the extinction coefficient (Crimaldi, 2008). The local fluorescence intensity from this solution at any point b along the path of this beam of light at a given time is then:

$$I_f = AI_o \Phi \varepsilon LC(b) \exp\left(-\varepsilon \int_0^b C dz\right), \quad (2-2)$$

where A is related to the collection efficiency of the imaging system, Φ is the quantum efficiency of the dye, L is the optical pathlength, and $C(b)$ is the local concentration of the dye (Walker, 1987). Hence, high dye concentrations can produce nonlinearities in the fluorescence due to absorption related changes in the local value of I_o . However, at low concentration and small optical pathlength,

$$-\varepsilon \int_0^b C dz \ll 1 \quad (2-3)$$

and the exponential function in Eq. (2-2) can be linearized to give:

$$I_f = AI_o \Phi \varepsilon LC(b) = AI_o LC(b) g(T), \quad (2-4)$$

so that the local fluorescence intensity is directly proportional to $C(b)$. In this thesis, the experimentally determined relation between the concentration of fluorescent dye C and the fluorescence intensity I_f is detailed in Chapter 3. In all cases, the dye concentration C , which was constant during a given experiment, was small enough so that Eq. (2-4) is valid.

Since the thesis uses the temperature-sensitive variations in I_f in Eq. (2-4) from certain fluorescent dyes in aqueous solution to estimate temperature fields, the next sections briefly review the theory of fluorescence, and how and why fluorescence intensity is affected by the solution temperature. Photobleaching, a phenomenon which also affects fluorescence intensity, is also introduced and discussed. A more detailed

introduction to fluorescence is available in the classic text by (Pringsheim, 1949) among other references.

2.1.2 Fluorescence Mechanism

When a beam of light passes through a material, its energy can be transferred to and/or pass through the material in a variety of forms. The light can be absorbed, reflected, transmitted, and scattered in various ways. The absorption of photons of light by a material excites the molecules of the material to an electronically excited state where the absorbed energy can be converted to rotational, vibrational (*i.e.* heat), or chemical energy, or re-emitted as photons with a lower energy, a process known as photoluminescence.

Two different types of photoluminescence, the process by which dye molecules absorb electromagnetic radiation and subsequently re-radiate photons of lower energy, are fluorescence and phosphorescence. The major difference between these two types is the time over which the photons are re-radiated. For fluorescence, the absorption of light of a particular wavelength is followed by the emission of light of longer wavelengths within a few ns. The term “fluorescence” was coined by the British scientist Sir George G. Stokes, who observed this phenomenon when the mineral fluorspar was illuminated with ultraviolet light. Stokes observed that the light emitted by fluorspar had longer wavelengths than the ultraviolet illumination, and the difference in wavelength between the excitation and emission is known as the “Stokes shift.”

Phosphorescence, on the other hand, is relatively long-lived, with emission lifetimes ranging from ms to min (Hu *et al.*, 2006). The relatively long lifetime of phosphorescence makes it possible to filter out any secondary fluorescence excited by reflected or scattered illumination by adjusting the time delay between excitation and imaging, thereby improving the signal-to-noise ratio (SNR) of the images.

Phosphorescent tracers are less commonly used than fluorescent tracers in aqueous solution, however, because most phosphorescent tracers require UV excitation, increasing both the cost and hazards associated with the illumination, and because phosphorescence can be quenched by oxygen, making it difficult to obtain accurate results under typical laboratory conditions (Hu *et al.*, 2006).

The process of fluorescence can be schematically illustrated by a simple diagram of the energy states of a “typical” fluorophore as shown in Figure 2.1. Fluorescence is the result of a three-stage process: absorption, existence at an excited state, and emission. During absorption, a fluorophore absorbs photons of energy $h\nu_{\text{EX}}$ (where h is Planck’s constant and ν_{EX} is the frequency of the excitation) incident upon the fluorophore from an external light source such as an incandescent lamp or a laser. This absorbed photon excites an electron in the fluorophore molecule from the ground state to a higher energy state. The electron then exists in this excited state for a very brief time, known as the excited-state lifetime, which is typically ps to ns.

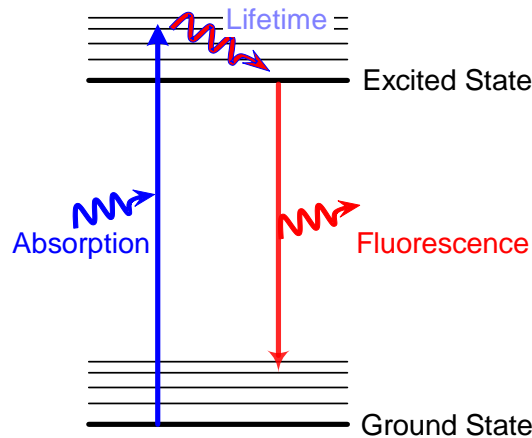


Figure 2.1: A schematic diagram illustrating the processes involved in optical absorption and subsequent emission of fluorescence.

Fluorescence emission is then the emission of a photon of energy $h\nu_{\text{EM}}$ (where ν_{EM} is the frequency of the emission) when the fluorophore electron returns to its ground state from an excited state. Because of energy dissipation during the excited-state

lifetime, $h\nu_{EM}$ is generally lower, and the emitted photon has a longer wavelength (by the Stokes shift), than that of the excitation. In general, fluorescence emission will occur if the excited photon energy is greater than the minimum energy corresponding to the band gap, so the emission spectrum is typically independent of the excitation wavelength. The entire fluorescence process repeats indefinitely as long as photons in the appropriate absorption band are available, unless the fluorophore is irreversibly destroyed in the excited state (an important phenomenon known as photobleaching, which will be discussed later).

Quantum yield (also known as the quantum efficiency), Φ , is the ratio of photons emitted to the number of photons absorbed, and a measure of the probability of fluorescence emission relative to all of the possible pathways for relaxation. In other words, Φ represents the probability that a given excited fluorophore will produce an emitted photon (fluorescence). In most applications, a high quantum yield is desired; the quantum yield of a given fluorophore varies with the temperature, the pH, and polarity of the solvent, and the concentration of the fluorophore in the solvent.

2.1.3 How Fluorescence and Lifetime is Affected by Changes in Temperature

As temperature increases, the fluorescence from most fluorophores decreases, although the degree of temperature sensitivity varies among fluorophores. Variations in the fluorescence emission can be considered to indicate changes in molecular activity with temperature, which suggests that increasing temperature increases molecular motion and collision, and hence decreases the rate of fluorescence, since the rate of radiative and nonradiative decay of electronically excited organic molecules in solution usually depends on the solution temperature.

The emissions from fluorescent solutions can be affected by temperature by a variety of mechanisms. First, the rate of collisional quenching, which can reduce

quantum yield by increasing non-radiative decay of excited electrons to the ground state, increases as the viscosity of the medium decreases, and the viscosity of liquids generally decreases as temperature increases. Thus, the collisional quenching of fluorescence can lead to significant decreases in Φ as temperature increases. Second, an increase in temperature usually increases chemical reaction rates, including the rates of the transitions between energy levels involved in fluorescence. The probability that fluorescence will occur, *i.e.*, that an electron will be excited and then decay back to its ground state and emit a photon, will therefore decrease as temperature increases.

The temperature-dependent portion of I_f , $g(T)$, in Eq. (2-4) depends on the quantum yield and the extinction coefficient of the fluorophore. The change in fluorescence intensity I_f with temperature is therefore mainly due to the variations in Φ , since ε is a weak function of temperature for most organic dyes (Kim *et al.*, 2003).

On the other hand, the lifetime of a fluorescence or phosphorescence can also extract temperatures from the temperature dependence of intensity decay of the temperature probes. Generally, the intensity decay of photoluminescence can be described by a single exponential function:

$$I(t) = I_o \exp\{-t / \tau\} \quad (2-5)$$

where the lifetime τ refers to the time when the intensity drops to $1/e$ (approximately 37 percent) of the initial intensity I_o and the lifetime is dependent on temperatures. Hence, temperatures can be measured by evaluating the characteristics of the intensity decay of the temperature probes with temperatures.

Photobleaching refers to the phenomenon where a fluorophore loses the ability to fluoresce due to over-exposure to excitation. Photobleaching occurs due to photon-induced chemical damage and chemical reactions, and is partially reversible in that some of this “lost” fluorescence is recovered some time after the excitation ceases. The

average number of required excitation and emission cycles for a particular fluorophore before significant photobleaching occurs varies with the type of fluorophore and its local environment, and varies by orders of magnitude. In general, photobleaching can be reduced by reducing the excitation energy or by limiting the time over which the fluorophore is exposed to excitation, at the cost of course of reducing the emitted fluorescence. Photobleaching should be negligible here because the flow of a fluorophore solution is imaged in these studies, so the fluorophore molecules, which are convected by the flow through the region illuminated by the excitation, are exposed to the excitation for only a brief interval (2–5 s).

In summary, fluorescence is a three-step process where an electron in a fluorophore molecule at the ground state is excited to a higher energy level by absorbing a photon at an appropriate excitation wavelength, remains up to a few ns at the excited higher-energy state, then decays back to the ground state by emitting a photon at a longer wavelength than the excitation. Both fluorescence intensity and fluorescence lifetime are single-valued function of the temperature of a fluorescent solution at a fixed concentration, and so variations in either property can be used to estimate the temperature of the solution. The next section reviews previous work on intensity-based and lifetime-based fluorescence thermometry.

2.1.3.1 Intensity-Based Fluorescence Thermometry (FT)

Liquid temperatures are most often estimated from changes in the intensity of the emissions from temperature tracers. In these methods, the emission from one or more fluorophores such as fluorescein (Fl), rhodamine B (RhB), and sulforhodamine B (SrB) in aqueous solution over one to three distinct wavelength bands are recorded, and used to estimate the temperature of the solution. The accuracy and spatial resolution of the temperature data then depends on the number of tracers, the number of wavelength bands imaged, and the details of the optical setup. This section describes intensity-based FT

techniques.

2.1.3.1.1 Single Tracer and Single Wavelength Band Techniques

Perhaps the most popular temperature tracer is RhB, a water-soluble fluorophore with a fluorescent intensity I_f in Eq (2-4) that decreases markedly with increasing temperature (Coppeta and Rogers, 1998). In its simplest implementation, intensity-based thermometry estimates temperatures from the change in fluorescence intensity from one tracer imaged over a single wavelength band.

Coolen *et al.* (1999) used a high-power Nd:YAG laser with a power density up to $2 \times 10^5 \text{ W/m}^2$ to excite RhB in natural convection in a cavity at a Grashof number $Gr = 4.5 \times 10^7$. By using this laser, they were able to examine a larger area of the flow compared with the more commonly used argon-ion lasers. The maximum uncertainty, which included the photobleaching of RhB at their high laser powers and re-absorption effects, was $1.7 \text{ }^\circ\text{C}$. Seuntiëns *et al.* (2001) applied this technique to measure the instantaneous 2D temperature field in the wake of a heated cylinder (8.5 mm in diameter and 495 mm in length) using $4 \times 10^{-7} \text{ mol/L}$ RhB, and measured temperature of $20\text{--}35 \text{ }^\circ\text{C}$ with an accuracy of $\pm 0.1 \text{ }^\circ\text{C}$ at a spatial resolution of $230 \text{ }\mu\text{m} \times 220 \text{ }\mu\text{m}$ using 8 bit CCD camera.

These methods have also been used to measure liquid temperatures with microscale resolution. Ross *et al.* (2001) used RhB to measure temperature fields and quantify the effects of Joule heating in the electrokinetically pumped flow of water through trapezoidal channels with cross-sectional dimensions of $20\text{--}75 \text{ }\mu\text{m} \times 30 \text{ }\mu\text{m}$ and $50 \text{ }\mu\text{m}$ diameter capillaries. Fluid temperatures ranging from $22 \text{ }^\circ\text{C}$ to $90 \text{ }^\circ\text{C}$ were measured with a precision ranging from $0.03 \text{ }^\circ\text{C}$ to $3.5 \text{ }^\circ\text{C}$, depending upon the extent of temporal and spatial averaging. Lavieille *et al.* (2000) used RhB to estimate the temperatures of monodisperse $200 \text{ }\mu\text{m}$ diameter evaporating ethanol droplets with a

random error of 1 °C. Fu and Li (2006) used RhB excited at a wavelength of 488 nm to visualize temperature gradients in an on-chip 50 μm \times 550 μm \times 28 μm microheater consisting of a resistance wire heater embedded in a PDMS chip.

The most commonly used transparent materials in microfluidic devices are silicate glasses and PDMS (polydimethylsiloxane). However, most of the fluorophores in the rhodamine family, including RhB, have at least some adsorption on negatively charged glass and PDMS surfaces due to their zwitterionic characteristics in solution (Ramette and Sandell, 1956). This absorption, by changing the fluorescence intensity, can introduce large errors in intensity-based fluorescence thermometry. Samy *et al.* (2008) therefore embedded RhB in a thin PDMS film and used this film, sandwiched between two glass substrates, as the “lid” for a PDMS-glass microchannel to measure surface temperatures. The largest discrepancy between their experiments of Joule heating in this channel and their numerical simulation was 4 °C.

A number of temperature-sensitive fluorophores other than RhB have been used as well. Sato *et al.* (2003) used Tris(bipyridine)ruthenium(II), which is excited by ultraviolet light, immobilized in a surface layer of SU-8 photoresist, to measure 2D temperature fields in a T-shaped microchannel. They reported that this film had a temperature sensitivity, measured in terms of the change in intensity per K, of $-3\%/^{\circ}\text{C}$ and estimated their temperature uncertainties based on 95% of confidence levels was 1.2 °C at a spatial resolution of 5 μm . Motosuke *et al.* (2009) used a mixture of 0.1 mM FI and 1 mM Brilliant Blue FCF in a tetraborate buffer solution to measure temperature distributions in a 500 μm \times 50 μm \times 50 mm borosilicate glass microchannel heated by a diode laser beam at 635 nm with an uncertainty of 0.5 °C at a spatial resolution of 530 nm.

The major practical disadvantage of single tracer intensity-based FT is that variations in I_f can (*cf.* Eq. 2-4) be due to variations in C and I_o as well as T . It is difficult

to have spatially uniform illumination of the region of interest, especially if absorption is significant, and it is also in many cases difficult to have steady illumination because of variations in the laser power output and/or imperfections in the components of the optical system (*e.g.* mirrors, lenses, and filters). We next briefly review liquid thermometry techniques that use the emissions from two dyes (at different wavelength bands), or a single dye at two or three different wavelength bands, to overcome the weaknesses of the single-tracer technique.

2.1.3.1.2 Dual-Tracer FT

Dual-tracer fluorescence thermometry (DFT), the most common method to decouple variations in I_f due to changes in T from those due to changes in I_o , uses two different tracers, A and B, with different emission bands. The temperature of the solution containing both fluorescent species is determined from the ratio of the intensities imaged over two distinct spectral bands, where each spectral band is selected to isolate the emissions from one of the two tracers. Since the species is excited by the same illumination (so $I_o^A = I_o^B$), the ratio of the intensities can be expressed as:

$$I'(T) \equiv \frac{I_f^A(T)}{I_f^B(T)} \propto \frac{g_A(T)}{g_B(T)} \quad (2-6).$$

Coppeta and Rogers (1998), who first described such a ratiometric scheme, which they called dual emission laser-induced fluorescence (DELIF), considered nine different water-soluble dyes. They then demonstrated DELIF by to directly measure temperature fields using 5×10^{-7} mol/L Fl and 8×10^{-7} mol/L RhB in a thermal plume with a standard deviation of 1.8 °C, or 2.5% of the ratio of the Fl and RhB emissions.

Sakakibara and Adrian (1999) used a similar technique, which they called two-color LIF, to measure nearly instantaneous three-dimensional water temperature distributions by scanning a laser light sheet. Using RhB and Rh110, which had

temperature sensitivities based on changes in intensity per °C change in solution temperature of 2.3 %/°C and 0.13 %/°C, respectively, they reported random errors, mainly due to random noise in their image acquisition system, of ± 1.4 °C (95 % confidence level) and maximum bias errors of 1.3 °C for their measurements in a stably stratified layer. The same authors later (Sakakibara and Adrian, 2004) used the same technique to study turbulent Rayleigh-Bénard convection, where a horizontal layer of fluid is heated from below and cooled from above. Using two high-resolution 14-bit monochrome CCD cameras (*vs.* to the 8-bit cameras used in their previous study) and improved post-processing techniques, they were able to reduce the uncertainty in their temperature data by nearly an order of magnitude to 0.17 K.

Recently, DFT has also been used to measure temperature fields at the microscale. Kim *et al.* (2003), who used RhB and Rh110 in what they called ratiometric thermometry, measured steady-state temperature fields in buoyancy-driven flow inside a 1 mm \times 10 mm \times 45 mm closed test cell under conditions where the product of the Grashof and Prandtl numbers varied from 86 to 301. Reported standard deviations of the temperature calibration in 95 % confidence level range from ± 1.967 °C for the 150 μm \times 100 μm calibration field-of-view to 0.412 °C for the 1200 μm \times 800 μm . Also, the deviations of the measured temperature from the numerical predictions were 2.3 °C and 0.92 °C at a spatial resolution of 19 μm \times 19 μm and 76 μm \times 76 μm , respectively. Natrajan and Christensen (2009), who used Q-switched Nd:YAG laser pulses providing sufficient illumination intensity over timescales much shorter than those of thermal transport at microscale to excite RhB and sulforhodamine 101 (SrB101), measured steady-state temperature gradients created by hot and cold thermal reservoirs across an array of parallel microchannels. The temperature sensitivities of the ratio of RhB and SrB101 emissions in ethanol and aqueous solutions were -1.5 %/K and -2.7 %/K, respectively. The standard deviations in Natrajan and Christensen's temperature data

were as great as 0.6 °C and 0.5 °C in ethanol and water, respectively, at a spatial resolution of about 22 μm. Fogg *et al.* (2009) used RhB/Rh110 to measure liquid-phase temperatures ranging from 35 °C to 100 °C in a two-phase microscale flow where air was injected into a heated microchannel.

Jeong *et al.* (2009) combined DFT with confocal laser scanning microscopy, which images only the light (here, fluorescence) from a small volume around the focus of the imaging system, to measure liquid temperatures in a heated microchannel. They used RhB/Rh110 in methanol to measure the temperature distribution across a 240 μm deep channel heated at the top; the bottom was simply exposed to ambient conditions, and estimated that the uncertainty in their intensity ratio measurements were 1% and 7% at 0 μm and 240 μm from the top and bottom of the channel, respectively.

The majority of DFT studies use a temperature-sensitive species, e.g. RhB, and a temperature-insensitive species, such as Rh110. As pointed out by Sutton *et al.* (2008), however, the accuracy of DFT can be further improved by using two temperature-sensitive species whose temperature sensitivities are “inverted.” They showed that fluorescein 27 (FL27) in aqueous solution had a temperature sensitivity of about 3.5 %/°C over a temperature range of 20–80 °C when excited by a 532 nm Nd:YAG laser pulse, and that DFT using the ratio of emissions from FL27 and RhB or FL27 and SrB had temperature sensitivities of 6.5%/°C and 7%/°C, respectively, *vs.* ~2%/°C for the combination of RhB and Rh101. Shafii *et al.* (2009), who used instead FL/SrB to measure temperature fields in the unidirectional solidification of aqueous ammonium chloride chilled from the bottom, reported that the temperature sensitivity of this combination was ~4%/°C over a temperature range of 4–20 °C, and that their in-situ measurement uncertainties were 0.8 °C for a single image frame, decreasing to 0.25 °C for the average of 10 consecutive frames.

2.1.3.1.3 Single Dye and Two Wavelength Bands

Although DFT can decouple variations in I_f due to changes in T from those due to changes in I_o , it cannot account for variations in dye concentration in, for example, an evaporating flow because the tracers may have different solubilities. Liquid temperatures in evaporating droplets, among other applications, can instead be estimated from the ratio of the emission intensities from a single dye imaged over two different wavelength bands.

Lavielle *et al.* (2001) developed what they call two-color LIF, where the ratio of the fluorescence emissions from RhB over two different wavelength bands, 520–540 nm and >590 nm, was used to isolate the variations in the signal due to temperature changes. They demonstrated that they could measure temperatures with an absolute accuracy of 1 °C of absolute accuracy in streams of monodisperse 100 μm and 200 μm diameter evaporating or combusting ethanol droplets. Wolff *et al.* (2007) applied the same technique to spray combustion in automotive engines.

Deprédurand *et al.* (2008) used pyromethene 597-8C9 as the temperature tracer because its emission spectrum, unlike those of RhB or SrB, is independent of the pH of the solution. They estimated the error in their temperature data in experiments modeling spray combustion where monodisperse droplets made of different fuels (dodecane, 3-pentanone, ethanol and a mixture of ethanol and 3-pentanol) were injected into a hot air chamber at 645 K to be 1.5 °C. Castanet *et al.* (2003) extended the technique to measurement of temperature fields within a single droplet with an estimated absolute accuracy of 1 °C by scanning a small $20 \times 20 \times 57 \mu\text{m}^3$ probe volume through a 200 μm diameter drop. Castanet *et al.* (2007) used this technique, along with acetone planar LIF to measure fuel vapor concentrations, to study the two-phase flow of an evaporating droplet stream for temperatures as great as 75 °C. Finally, Bruchhausen *et al.* (2005) used two-color LIF to measure instantaneous two-dimensional temperature fields in a heated turbulent jet injected into a co-flowing stream.

2.1.3.1.4 Single Dye and Three Wavelength Bands

Finally, Lavieille *et al.* (2004) extended their two-color technique to imaging the emissions from RhB over three “colors,” or wavelength bands. Although two-color FT can isolate variations in I_f due to changes in T from those due to changes in I_o and dye concentration, the accuracy of FT measurements over large optical pathlengths can be affected by reabsorption of the fluorescent emissions, especially since the amount of reabsorption varies between the two bands. The intensity of the emissions over the three different wavelength bands (1, 2, and 3) was combined to give two different ratios (1 to 3 and 2 to 3, for example) to quantify the amount of reabsorption and correct for this effect, and they were able to measure temperatures in a heated jet over optical pathlengths as large as 80 mm with measurement errors of 0.5 °C.

Maqua *et al.* (2006) used the same technique to measure transient temperatures in moving evaporating ethanol-acetone droplets with an accuracy of about 1.5 °C. Comparison with numerical simulations shows that the experimental results and the numerical results follow a similar trend, although there are significant discrepancies due, at a minimum, to the assumptions made in the simulations (the heat and mass transfer within the droplets are assumed to be spherically symmetrical; the calculation starts with uniform temperature and composition distributions; and the physical properties of the acetone-ethanol mixture, such as binary diffusion coefficient, and their variations with temperature are not well-known).

2.1.3.2 Fluorescence Lifetime or Phosphorescence-Based Thermometry

Although the intensity-based thermometry technique is the most well-known technique to measure liquid phase temperatures, the dependence of fluorescence lifetime on temperatures has been also utilized to estimate liquid temperatures in several applications. Mendels *et al.* (2008) developed fluorescence lifetime imaging microscopy

(FLIM) for SrB and validated their method by comparing their experimental results to predictions from finite-volume simulations for the mixing of water at two different temperatures and the mixing of methanol with a water-methanol mixture. They reported that the lifetime of SrB emissions varied from 0.4 ns to 1.8 ns over a temperature range of 20–90 °C in laminar flows at $Re \leq 10$.

Phosphorescent emissions, which typically have longer lifetimes than fluorescence, have also been used to measure temperature fields. Thomson and Maynes (2001) measured liquid temperatures using the emissions from the phosphorescent supramolecule 1-bromonaphthalene bound inside a “cup” of mono glucosyl- β -cyclodextrin sealed by an alcohol “lid” (1-BrNp.Gb-CD.ROH). They measured temperatures of 23–53 °C in a horizontal tube with laminar buoyant mixing at $Re = 200$ and reported experimental uncertainties of 1.0–1.5 °C. Hu and Koochesfahani (2003) developed the molecular tagging thermometry (MTT) technique, and used it to obtain simultaneous temperature and velocity measurements in a pulsed jet of water at $T = 25$ °C discharging into ambient fluid at $T = 36$ °C. The estimated temperature uncertainty was less than 0.25 °C for $T = 20$ –50 °C. Hu *et al.* (2006) further developed the MTT technique to have an adjustable temperature sensitivity, and reported that their method had a temperature sensitivity, measured in terms of variation in emission lifetime per °C, of 18.2 %/°C. The random error in their MTT temperature data obtained in the wake of a heated cylinder at $Ri = 0.36$ was estimated to be 0.2 °C based on 95 % confidence levels.

2.1.4 Thermochromic Liquid Crystal Thermometry

Although TLCs are mainly used to measure wall surface temperatures, TLCs have also been used in a few applications to measure liquid temperatures. Ozawa *et al.* (1992) used 10–20 μm diameter encapsulated TLCs to visualize the temperature and velocity fields in natural convection in a 40 mm \times 40 mm \times 6 mm Hele-Shaw at Rayleigh

numbers $Ra = 9.7 \times 10^5 - 2.7 \times 10^7$, reporting isotherms from 28 to 30 °C at 0.3 °C intervals and velocity magnitudes in the cell of 2–3 mm/s. Hiller *et al.* (1993) used TLC to investigate the transient natural convection of a water-glycerin mixture under conditions where both convection and conduction are significant in a cubical cavity at $Ra = 1.66 \times 10^5$ and Prandtl number $Pr = 1109$ based on the cavity dimension

Thermochromic liquid crystals have also been used as particle-image velocimetry (PIV) tracers to simultaneously obtain velocity and temperature data. Kowalewski (2001) used 50 µm unencapsulated TLC to measure 2D temperature and velocity fields in natural convection flows generated from a temperature gradient between a heater and the bulk fluid, and obtained temperature uncertainties of 0.15 °C for temperatures $T = 2-5$ °C in the red-green color range of his TLC and 0.5 °C for $T = 5-8$ °C in the blue color range. The different accuracies in temperature were due to the nonlinear relationship between reflected color and temperature. Dabiri and Gharib (1996) visualized flow patterns, vorticity fields, and temperature fields using encapsulated TLCs inside a 2.54 cm cube where a pair of opposite walls were heated and cooled sinusoidally at phases of 0°, 90°, and 180° at an oscillation period of 25.9 s. Park *et al.* (2001) obtained time-resolved velocity and temperature distributions using microencapsulated TLC in the wake of a heated circular cylinder at $Re = 610$ and reported an uncertainty of 0.5 °C for temperatures ranging from 25.8 °C to 28.5 °C. Pehl *et al.* (2000) examined the performance of encapsulated TLCs at very high pressures (as great as 7000 Bar), reported that temperature resolution of TLCs thermometry was 0.6 °C estimated by human eye, and measured temperature variations as great as 2.4 °C generated by pressurizing water from 2670 to 3920 Bar, over a region 6 mm in diameter.

Fujisawa and Funatani (2000) mapped 3D water temperature fields near a heated surface seeded with encapsulated TLCs by scanning two parallel light sheets, each 5 mm thick, generated by two stroboscopes. By traversing these light sheets at a constant speed

of 98 mm/s in 0.61 s, and capturing color images with a CCD camera (768×492 pixels), they were able to determine the 3D temperature distribution from a sequence of images. The reported measurement uncertainty was $0.11 \text{ }^\circ\text{C}$ over a temperature bandwidth $\Delta T = 2.3 \text{ }^\circ\text{C}$. Five year later, the same group (Fujisawa *et al.*, 2005) used a similar technique to study turbulent Rayleigh-Bénard convection at $Ra = 2.3 \times 10^7$ over a temperature range of $5 \text{ }^\circ\text{C}$ with an accuracy of $0.13 \text{ }^\circ\text{C}$. Ciofalo *et al.* (2003) also demonstrated simultaneous 3D PIV and thermography in Rayleigh-Bénard convection of glycerin in a $60 \text{ mm} \times 120 \text{ mm} \times 240 \text{ mm}$ rectangular enclosure at $Ra = 3000\text{--}2000$, and reported a measurement uncertainty of $0.05 \text{ }^\circ\text{C}$ for temperatures ranging from $19.2 \text{ }^\circ\text{C}$ to $20.9 \text{ }^\circ\text{C}$.

Although TLC is a non-intrusive and cost-effective thermometry method that can be used for liquid thermometry, it is impractical in many cases for microscale measurements. Above all, most encapsulated TLCs, are too large, with diameters of $O(10 \text{ } \mu\text{m})$, to spatially resolve temperature fields in many microfluidic devices. Moreover, as will be discussed subsequently, the narrow temperature bandwidth of TLC makes them impractical for flows with large temperature gradients or time-varying temperature fields.

2.1.5 Particle Image Thermometry

For particles suspended in a fluid, Brownian diffusion due to the collision of fluid molecules with the particle due to their random thermal motions is significant for particles less than $1 \text{ } \mu\text{m}$ in diameter suspended in an aqueous solution. Because the random motion of the fluid molecules depends on the temperature of the fluid, this temperature can be extracted from estimates of Brownian motion (Santiago *et al.*, 1998). Olsen and Adrian (2000), who postulated that a spreading of the correlation peak in PIV data could be used to deduce fluid temperature, derived equations describing the shape and height of the cross-correlation function in the presence of Brownian motion at a

given temperature in μ PIV. Hohreiter *et al.* (2002) then applied the theory of Olsen and Adrian (2000) to measure temperatures in quiescent pools of water containing 700 nm particles over a range of 20–50 °C, and reported results within 3 °C of experimental independent thermocouple readings.

Chamarthy *et al.* (2009) attempted to improve Hohreither’s work by introducing three different thermometry methods: particle image velocimetry-based thermometry (PIVT), particle tracking thermometry (PTT), and low image density (LID) PIV. The maximum uncertainty for water temperatures of 20–80 °C was found to be 0.5 °C in PIVT. Park *et al.* (2005) measured liquid temperatures by tracking the 3D Brownian motion of 500 nm polystyrene fluorescent particles suspended in water at temperatures of 5–70 °C using optical serial sectioning microscopy (OSSM). They implemented in situ and full-field mapping thermometry with microscale resolution and the overall 3D mean square displacement detection uncertainty at 25 °C was $\pm 0.054 \mu\text{m}^2$.

Perhaps the biggest disadvantage of these methods is that accurately quantifying Brownian fluctuations requires statistically well-converged data, or measurements over long times compared with typical microscale flow time scales. These methods are at present hence unsuitable for unsteady flows.

2.2 Surface Thermometry Techniques

One of the objectives in this thesis is to measure wall surface temperatures using fluorescence thermometry with evanescent-wave illumination with a spatial resolution of $O(1 \mu\text{m})$. This section therefore reviews current surface thermometry techniques.

2.2.1 Micro-Thermocouple, Scanning Thermal Probe, and Diode Sensors

Thermocouples (TCs) are among the most commonly used devices for measuring surface temperatures, and several groups have fabricated thin-film microthermocouples

(μ TCs) that can measure temperatures with micrometer-scale spatial resolution. Beckman *et al.* (1993) fabricated a chromel-alumel μ TC with a junction consisting of a thin circular disk 80 μm in diameter and 2.5 μm in thickness, and characterized its static and dynamic characteristics by measuring the temperature field in the turbulent subcooled boiling flow of R-113 through a heated annular channel. Allen *et al.* (2003) fabricated a nickel (Ni)-silver (Ag) μ TC to measure the in-channel temperature rise caused by a simple acid-base reaction between HCl and NaOH, an enzyme-catalyzed biochemical reaction, and Joule heating in electroosmotic flow. They claimed that both the response time and sensitivity of their μ TCs were significantly superior to traditional wire-based TCs although their device was more fragile, especially when operating under harsh conditions, *e.g.* in corrosive solutions.

A number of groups have also fabricated 2D arrays of nanometer-scale TCs. Park and Taya (2005) constructed an array of 10×10 thermocouples 0.15 μm thick with 100 junctions to measure temperature distributions over a 9 mm \times 9 mm area on a silicon chip, and were able to use this array even in the presence of high temperature gradients. Jang *et al.* (2003) used a micro-thermal sensor array having 25 temperature sensors 500nm thick with size of 200 $\mu\text{m} \times 400 \mu\text{m}$ corresponding to surface area of 5 mm \times 5 mm to measure temperature distribution at the bottom surface of microchannel heat sink of 10 mm \times 10 mm composed of microchannels 200 μm thick, 1.4 mm height, and 200 μm fin thickness. Their temperature sensor array agreed with readings of a commercial K-Type thermocouple within 7.5 $^{\circ}\text{C}$ at maximum in the temperature range of 0–1250 $^{\circ}\text{C}$.

Other techniques used for microscale solid-state thermometry include scanning thermal microscopy (SThM), diode sensors, and micro-resistive temperature detectors (μ RTD). Majumdar (1999), who introduced SThM for mapping surface temperature distributions and thermal properties with spatial resolutions of less than 100 nm, reviews the fabrication steps for SThM probes, their measurement characteristics, and

applications of the SThM such as gas conduction, near-field radiation, and liquid-film conduction. Later, Shi *et al.* (2001) developed a batch fabrication process for mass production of thermally designed SThM probes in silicon dioxide with a silicon nitride tip of radius as small as 20 nm suitable for thermal imaging with sub-100 nm resolution. These probes have been used extensively for thermal imaging of micro- and nano-electronic devices with spatial resolutions as fine as 50 nm in ~ 0.5 K/K of the temperature response of the probes estimated from the comparison of the temperature change between junction temperature of the thermal probe and sample temperature.

Diode sensors, where temperatures are estimated from the voltage drop across a forward biased p-n junction diode are also commonly used to measure temperatures. Sclar and Pollock (1972) showed that the voltage was directly proportional to temperature at temperatures of 4–300 K for three types of silicon (Si) p-n diodes, and that these diodes avoided the degradation effects common in highly doped p-n gallium arsenide (GaAs) diodes. Shwarts *et al.* (2000) developed criteria for design parameters for diode temperature sensors for maximizing either the temperature bandwidth or sensitivity. Recently, Han and Kim (2008) measured temperatures ranging from 0 °C to 70 °C over a 8 mm square area with a diode temperature sensor array of 32×32 diodes (1024 diodes total), where each diode had an area 50 μm square.

Although these solid-state temperature sensors have been used extensively to measure wall surface temperature distributions, they are seldom used to measure liquid-phase temperatures because they disturb the flow. Moreover, given the additional complexity involved in the fabrication, integration and alignment of 2D μTCS or diodes in a microfluidic device, it is impractical to fabricate such temperature probes inside complex 3D microscale flow loops at every location of interest. These types of probes are therefore impractical for measuring liquid-phase or wall surface temperature fields over large regions of the flow.

2.2.2 Infrared Thermometry

Nonintrusive infrared (IR) thermal imaging is widely used to measure surface temperatures and a variety of commercial systems are available for this purpose. Arakawa *et al.* (1993) used automated IR radiometry, which is useful for non-contact temperature measurements, to obtain transient 2D wall surface temperature distributions imaging through a flame, but their technique could not be used for flames with emissivities exceeding 0.1. Konishi *et al.* (2000) considered the accuracy, measurement characteristics, and limitations of IR thermography using an IR camera over a spectral range of 8–12 μm , and measured transient 2D temperature profiles with the same camera at the interface between liquid propanol and its vapor at temperatures of 20–80 $^{\circ}\text{C}$ with an estimated accuracy of 0.1 $^{\circ}\text{C}$.

However, IR imaging is in most cases unsuitable for measuring liquid temperatures because this method estimates the temperature from the radiation emitted by an object. Accurate IR thermography results therefore require accurate calibration of the object's emissivity, which is a function of wavelength. Since the emissivity of a liquid varies significantly with wavelength at IR wavelengths, and many of the transparent solids used as window materials to contain the liquid strongly absorb in the IR (Fan and Longtin, 2000), it is in many cases impractical to obtain accurate liquid temperatures, especially in the bulk of the liquid, using IR thermography. Moreover, it is practically difficult to determine the spatial resolution of IR thermography along the optical axis because an exact determination of the locations along this axis where the imaged radiation is emitted requires a complete solution of the radiation transfer equations in the fluid that accurately accounts for absorption, emission, transmission of the fluid and convection (Patil and Narayanan, 2006).

Since the infrared emissions that are imaged in IR thermography include not just the emissions from the object whose temperature is being measured, but also from its

surroundings, these emissivity calibrations typically require not only determining how the emissivity of the object varies with temperature over a given range of wavelengths, but also calibrations to determine how much of the emissions are from the surroundings and scattered by the object. Also, since the radiation from the object and its surroundings is attenuated before imaging due to absorption by the surrounding atmosphere and scattering by particles, the effects of this attenuation must also be quantified. Commercial IR thermography systems therefore usually require the emissivity of the object, the attenuation and temperature of the atmosphere, and the temperature of the surroundings as inputs.

2.2.3 Thermochromic Liquid Crystal Thermometry

Thermochromic liquid crystals (TLC), specifically cholesteric and nematic liquid crystals, are also commonly used to measure local surface temperatures. When a thin layer of TLC is applied to a surface, the crystals selectively reflect light at different wavelengths depending upon the local surface temperature. The color of the light reflected by TLC when illuminated by white light changes from red at low temperatures to green, blue or violet at higher temperatures, but the temperature bandwidth over which these colors vary is quite limited, and typically less than 10 °C for a given type of TLC . These color changes are repeatable and reversible as long as the liquid crystals are not physically damaged. The liquid crystals are usually encapsulated in microspheres of 5 to 20 μm diameter to protect them from mechanical and chemical damage (Ireland and Jones, 2000), then applied evenly to a well-prepared surface to obtain reproducible and accurate temperature data.

The colors reflected from the TLC depend on the lighting/viewing setup, the spectra of the light incident upon the TLC and the background light, and the optical properties of the measurement path (Farina *et al.*, 1994). All of these effects must be considered when determining a single TLC color-temperature calibration curve. Colors

in the red, green, blue (RGB) color space are usually quantified in terms of their hue, saturation and value (HSV space). In TLC thermometry, the temperature of the encapsulated liquid crystals is usually estimated from their hue.

At present, two methods are used to derive quantitative temperature information from the color of TLCs. The first method, the “narrow-band” technique, utilizes TLCs in a narrow temperature bandwidth, typically no more than 1 °C. Colors over the yellow band are typically mapped to the temperature of the encapsulated liquid crystals because this spectral band usually spans the smallest temperature range for most TLCs. A number of researchers have used the narrow-band technique to determine local convective heat transfer coefficient distributions. Narrow-band TLC enables accurate measurements of the temperature distribution for nominally isothermal objects, giving highly accurate estimates of small surface temperature variations. However, using this method to determine the isotherms over the entire surface of an object is usually very time-consuming, and obtaining full-field temperature measurements with the narrow-band technique is difficult (Farina *et al.*, 1994

Because narrow-band TLC is limited to a small temperature range, there are few measurements of heat transfer coefficient using this technique. Hippensteele *et al.* (1983) used a plastic sheet coated with TLCs and a thin-foil heater to estimate steady-state isotherms and heat transfer coefficients (HTC) in turbine blade cooling. Their thermography results were obtained over a narrow temperature range, however, suggesting that their data represent a limited set of isotherms. Camci *et al.* (1993) used the narrow-band technique developed by Camci *et al.* (1992) to measure transient HTC fields over a duct section whose cross-section changed from a square 20.8 cm on a side to a 32.2 cm × 10.7 cm rectangle. The standard deviation in the hue was about 10% of the temperature bandwidth of the TLCs and the estimated uncertainty in convective HTC was 5.9%.

Temperatures can also be estimated using a variety of TLCs by “wide-band” thermometry, which relates the hue to the surface temperature over the full range of colors. Temperatures spanning a wide range can be obtained from a single image by spraying different types of encapsulated TLCs onto the surface whose temperature bandwidths span the range of expected surface temperatures. The primary drawback of this technique is that it requires a complicated TLC color-temperature calibration to accurately resolve the highly non-linear variation of hue versus temperature of TLC. Also, it’s more time-consuming to implement than narrow-band technique because of the required post processing.

Hollingsworth *et al.* (1989) calibrated wide-band liquid crystal paints over a temperature range of 28–34 °C with an uncertainty of 0.5–1 °C and used these TLCs to measure the steady-state temperature field in the flow around a row of unheated cubical elements placed on a heated wall in a wind tunnel. The estimated uncertainty in their convective heat transfer coefficients was 11.7% based on their mean surface temperature measurements. Camci *et al.* (1992) developed a new digital image processing technique, the hue capturing technique, which reduced the uncertainty of wide-band thermometry to values as small as 0.08 °C, and used this method to obtain temperature fields for a heated impinging jet on a flat surface. Farina *et al.* (1994) developed a coherent, transportable, and video-based calibration system for accurate, full-field, surface temperature measurements with microencapsulated TLCs that is independent of the spectrum of the illumination, the presence of background lighting, the angle of incident beam, and the optical path in measurement system. Their approach gives an estimated experimental uncertainty of ± 0.4 °C (based on 95% confidence intervals) for temperatures $T = 309\text{--}319\text{K}$. Richards and Richards (1998) investigated the transient temperature changes in an evaporating water droplet suspended in a jet of dry air using microencapsulated TLC ranging from 5 to 15 μm in diameter with a temperature range of 30–35 °C, and.

reported transient temperature data at spatial resolutions as small as 100 μm and temporal resolutions as small as 0.03 s with an uncertainty of 0.75 $^{\circ}\text{C}$.

In summary, the technique does not require much equipment to implement, and the tracers themselves are inexpensive. The characteristics of TLC thermometry are, however, determined by the relatively narrow range of a specific TLC, and by the requirement to extract temperature information from (reflected) color. Liquid crystals can be used to determine surface temperatures with good accuracy because of the small temperature bandwidth of TLC. However, TLC are for the most part impractical for transient temperature measurements because significant changes in surface temperature will give temperatures beyond the working range of the liquid crystal. Liquid crystal thermometry is also often impractical for measurements over a wide range of surface temperatures because of the difficulties in calibrating a variety of TLC in the wide-band technique. Finally, quantifying color (*vs.* intensity), and quantifying how variations in the illumination and imaging systems affect the colors reflected by the TLC, greatly complicates the image processing required to map colors to surface temperatures, and can significantly reduce the accuracy of TLC thermometry.

CHAPTER 3

Experimental Apparatus

This chapter details the apparatus used in the evanescent wave-based fluorescence thermometry (EFT) studies to measure wall surface temperatures and the dual-tracer fluorescence thermometry (DFT) experiments to measure bulk fluid temperatures. Section 3.1 describes the criteria for selecting the specific fluorescent species employed here, and their spectral characteristics. Section 3.2 discusses the optical systems used to illuminate and image the fluid flowing through the heated channel.

3.1 *Fluorescent Dyes*

In this thesis, both EFT and DFT exploit the temperature-dependent intensities of the fluorescence emissions from various species. As reviewed in chapter 2, the majority of temperature-sensitive fluorophores have a quantum yield, and hence an emission intensity, that decreases with increasing temperature because the non-radiative dissipation in most cases increases with increasing temperature. Fluorescein, however, has an emission intensity that, when excited at $\lambda = 514$ nm (*i.e.*, a wavelength significantly longer than its absorption peak), *increases* with increasing temperature because its absorption at 514 nm also increases with temperature. This atypical behavior of Fl is due to the change in its absorption spectra with temperature. As illustrated in Figure 3.1, the increase in the excitation wavelength λ_{ex} corresponding to the absorption peak with increasing temperature leads to an increase in the absorption at $\lambda = 514$ nm. This increase in absorption, and hence the amount of energy that excites fluorescence, leads to an increase in emission as temperature increases (Coppeta and Rogers 1998).

As indicated previously, the second fluorophore should have a fluorescence which

decreases with increasing temperature to improve the temperature sensitivity of DFT. Although there are several fluorophores whose emission intensity decreases with increasing temperature, SrB was chosen as the second species because: *i*) it can also be excited at 514 nm due to its relatively broad absorption spectrum; and *ii*) its emission band, with a peak at 591 nm, has little overlap with that of Fl, with a peak at 518 nm (Shafii *et al.* 2009).

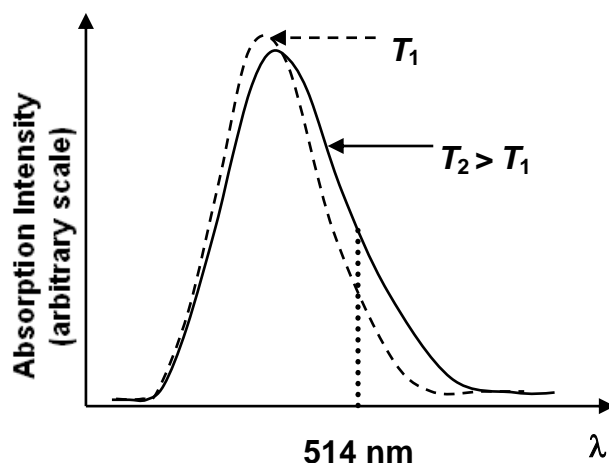


Figure 3.1. A schematic diagram of the absorption spectra as a function of excitation wavelength for Fl at temperatures T_1 (dashed) and $T_2 > T_1$ (solid line). At $\lambda = 514 \text{ nm}$ (dotted line), the absorption at T_2 is greater than that at T_1 .

Figure 3.2 shows (a) the normalized absorption spectrum measured by a spectrometer (HR4000CG-UV-NIR, Ocean Optics, Inc.) and (b) the normalized emission spectrum measured by a fluorescence spectrometer (QuantaMaster, PTI, Inc.) as functions of λ for 5 $\mu\text{mol/L}$ Fl (black solid line) and 5 $\mu\text{mol/L}$ SrB (blue dashed line), with both fluorophores present in the same aqueous solution, at pH 8.5. The absorption and emission spectra for Fl and SrB at pH 9.2 are identical to those obtained at pH 8.5, suggesting that the spectral characteristics of Fl and SrB is independent of pH over this range of values. The absorption spectra verify that both Fl and SrB can be excited at a wavelength of 514 nm. The emission spectra show that the fluorescence from the Fl and the SrB can be isolated from each other using appropriate filters. Shafii *et al.* (2009)

isolated the SrB emissions from those of the FI using a longpass filter that only transmitted light at $\lambda \geq 600$ nm, and reported that the leakage of FI emissions through this filter, or “cross-talk” with the FI, was no more than 0.1% of the total signal.

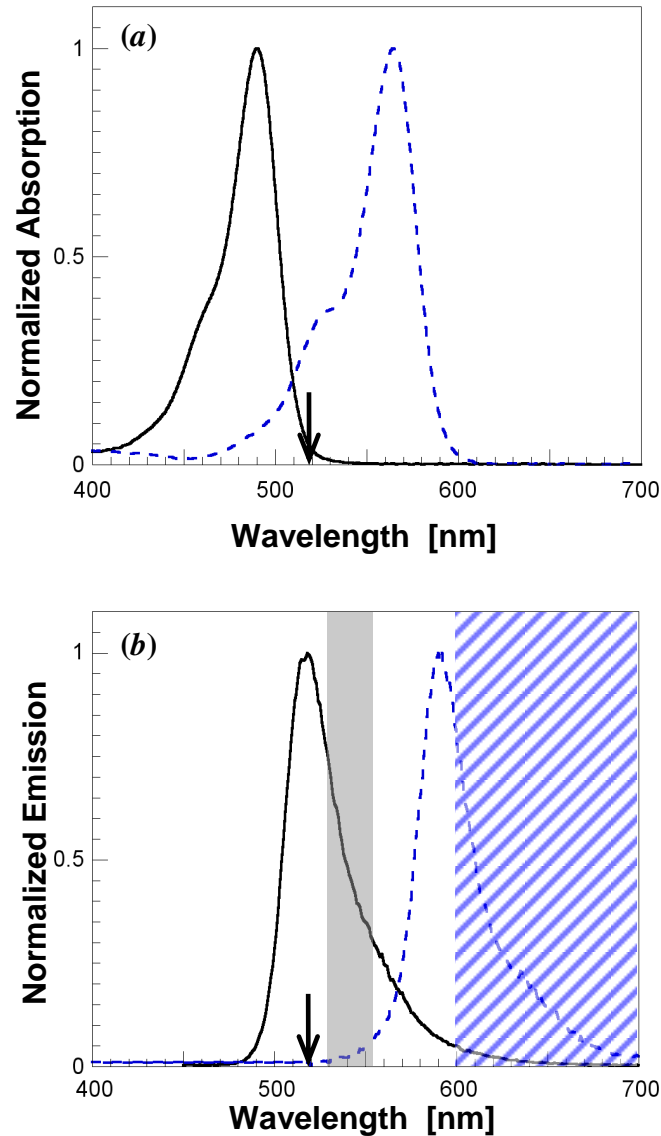


Figure 3.2. Plots of (a) absorption normalized by its maximum value and (b) emission normalized by its maximum value, both as a function of wavelength, for FI (black solid line) and SrB (blue dashed line). The arrows on both spectra indicate the excitation at 514 nm (and so only the portion of the emission spectrum to the right of this arrow will be emitted by FI and SrB). The shaded and hatched regions on the emission spectrum denote the wavelengths transmitted by the filter cubes that isolate the emissions from FI and SrB, respectively, in these experiments.

3.2 *Optical Setups*

The optical setups used in the two different sets of experiments consist of illumination systems to excite the fluorescence and imaging systems to collect the temperature-sensitive fluorescence. This section discusses the major components of these systems and their characteristics.

3.2.1 **Illumination Systems**

Figure 3.3 illustrates the evanescent-wave illumination system for the EFT studies. The evanescent-wave illumination is generated from a $\lambda = 514$ nm laser beam from a continuous-wave (CW) air-cooled argon-ion laser (543-GSA03, CVI Melles Griot) coupled to an angled, polished, and polarization-maintaining optical fiber (09 PMF 001, CVI Melles Griot) with a laser-to-fiber coupler (09 LFC 001, CVI Melles Griot). The coupler, which focuses the light from the laser to a spot matching the size of the fiber core with a lens, is attached directly to the laser head. Three fine tilt adjustment screws are used to align the spot from the laser beam to the fiber core, and once the coupler is aligned to give the maximum coupling efficiency of about 65%, the alignment is maintained by tightening three locking screws. The output power of the laser in all cases was kept below 20 mW to avoid damaging the microscope optics and the microscope objective.

The opposite end of the optical fiber is connected to the inverted total internal reflection fluorescence (TIRF) microscope system (IX71, Olympus). To create an evanescent wave at the glass-water interface, the optical fiber must be carefully aligned to the TIRF illuminator. Summarizing the instructions from the manufacturer, the four steps involved in this alignments are: *i*) make the illumination from the fiber without the objective lens as uniform as possible; *ii*) align the illumination so that it passes along the vertical through the objective; *iii*) adjust the position of the fiber with respect to the

illuminator so that the beam emerges from the objective with a profile that is as close as possible to a Gaussian profile; and *iv*) if required, re-adjust the beam path so that it passes along the vertical through the objective.

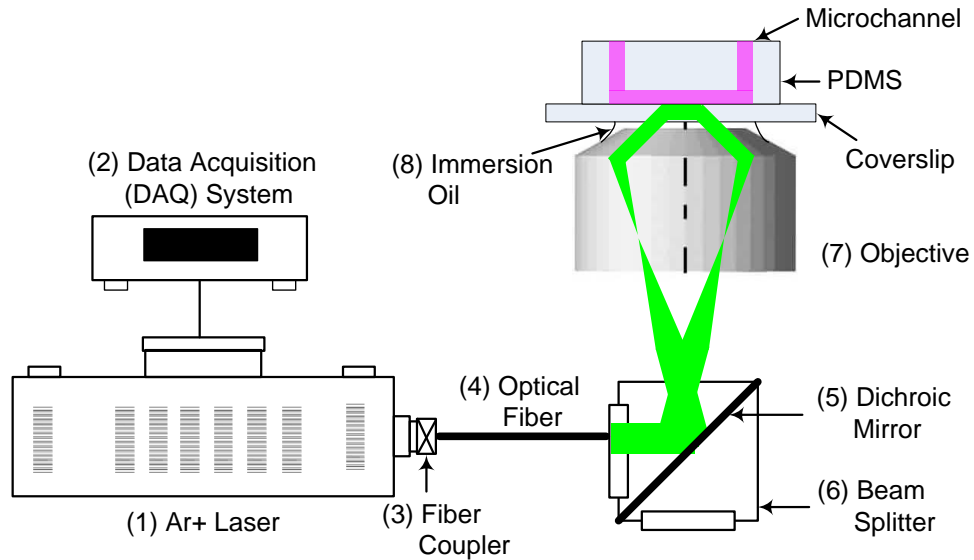


Figure 3.3. The illumination systems for the EFT experiments.

Table 3.1. Components of the illumination system used in the EFT studies

Label	Item	Manufacturer	Model	Notes
1	Argon-Ion Laser	CVI Melles Griot	543-GS-A03	
2	DAQ system	Agilent Technology	HP 34970A	
3	Fiber Coupler	CVI Melles Griot	09 LFC 001	Packaged together
4	Optical Fiber	CVI Melles Griot	09 PMF 001	
5	Dichroic Mirror	Chroma Technology	Zq514rdc	
6	Beam Splitter	Chroma Technology	C122968	Custom
7	Objective Lens	Olympus	PlanApo N	60×/NA 1.45
8	Immersion Oil	Cargille Laboratories	16242	Type DF

After the optical fiber has been aligned to the TIRF illuminator, the evanescent waves are created by using the laser alignment micrometer attached to the illuminator to adjust its position, thereby translating the laser beam vertically. As the laser beam is translated, the angle of incidence changes, and the beam is first refracted glass-water interface between glass and water. As the angle of incidence continues to increase by further translation of the laser beam, the angle of incidence becomes greater than the critical angle, the beam becomes totally internally reflected at the interface. The reflected beam will then return through the objective. The components of this illumination system are listed in Table 3.1.

The angle of incidence θ_i of the laser beam after passing through the TIRF objective is given by:

$$\sin \theta_i = \frac{R}{f n} \quad (3-1)$$

where R is the distance between the laser beam and the central axis of the TIRF microscope objective, f is the focal length of the objective, and n is the refractive index of the glass coverslip (which is same as that of immersion oil) (www.olympusmicro.com). For the TIRF microscopy system used here, $f = 3$ mm, $n = 1.522$, and $R = 4.27$ mm, giving $\theta_i = 70.06^\circ$. The penetration depth, or the length scale of the exponential decay of the evanescent-wave illumination (*i.e.*, $I(z_p)/I_o = 1/e$) $z_p = 79.1$ nm (*cf.* section 4.1.2).

Figure 3.4 illustrates the volume illumination system for the DFT studies. The beam from a multiline air-cooled argon-ion laser (543-MA-A03, Melles Griot) was passed through an iris (04 IDC 003, Melles Griot) to remove higher-order spatial modes and then a laser excitation filter (z514/10x, Chroma Tech.) to isolate the light at $\lambda = 514$ nm. Although the laser produced about 110 mW of 514 nm light, only about 60 mW was transmitted through the excitation filter. The 514 nm beam was then steered by two

mirrors (02 MPQ 007/001, Melles Griot) into a beam expander (NT55-578, Edmund Optics) which expanded the diameter of the beam tenfold. The beam expander was then adjusted to ensure that the expanded beam illuminated the appropriate region of interest. Table 3.2 lists the components of the volume illumination system.

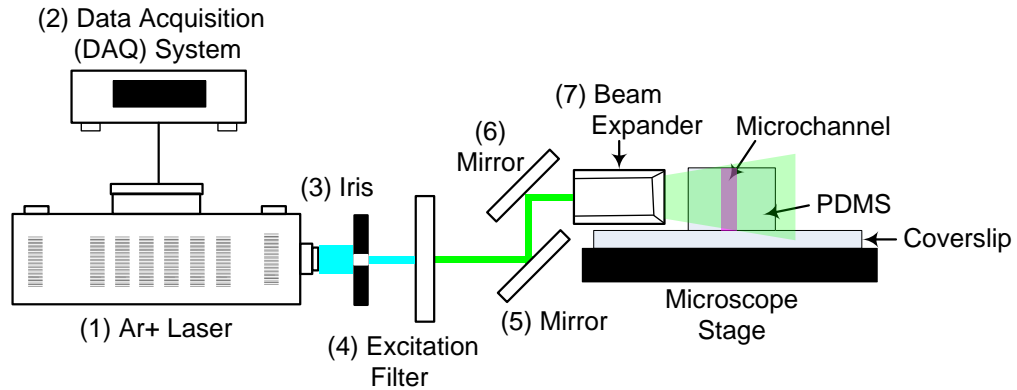


Figure 3.4. The illumination systems for the DFT experiments.

Table 3.2. Components of the volume illumination system

Label	Item	Manufacturer	Model	Notes
1	Argon-Ion Laser	Melles Griot	543-MA-A03	0.5 W, mutiline
2	DAQ system	Agilent Technology	HP 34970A	
3	Iris	Melles Griot	04 IDC 003	
4	Excitation Filter	Chroma Technology	z514/10x	FWHM* =10 nm
5	Optical Mirror	Melles Griot	02 MPQ 007/001	
6	Optical Mirror	Melles Griot	02 MPQ 007/001	
7	Beam Expander	Edmund Optics	NT55-578	10x expander

* FWHM = Full width at half maximum

3.2.1.1 The Characteristics of the Argon-Ion Laser

The profile of laser beam in its fundamental transverse mode, TEM₀₀, is a Gaussian:

$$I(r) = I_o \exp\left(-\frac{2r^2}{w(z)}\right) \quad (3-2)$$

where I_o is the intensity at the center of the beam at its waist (*i.e.*, at the z -position where the beam has the smallest diameter or $z=0$), r is the radial distance from the central axis of the beam, z is the axial distance from the beam waist, and $w(z)$ is the radius at which the intensity drops to $1/e^2$ of its value at the center, or $r=0$. Although there are a variety of beam profiling methods, a simple knife-edge method was used here to estimate the properties of the laser beam profile (Khosrofian and Garetz, 1983).

In this method, a sharp-edged razor blade was translated along a given diameter of the beam from the argon-ion laser (543-MA-A03, Melles Griot) using a translation stage with a micrometer (406, Newport Corp.) immediately before the beam expander. The power transmitted through the knife edge was then measured with a laser power meter (Lasermate Q, Coherent) as the knife edge was translated 100 μm increments across the beam until the entire beam was blocked by the knife edge.

Figure 3.5 shows the normalized power of the argon-ion laser as a function of the position of the knife edge. Cross-sectional power profiles were obtained by translating the knife edge across the laser beam along both vertical and horizontal directions in separate experiments. At a given location z along the optical axis, the diameter of the laser beam $w(z)$, assuming that it has a Gaussian profile, is then (Khosrofian and Garetz, 1983)

$$w = 1.28(x_{10} - x_{90}) \quad (3-3)$$

where x_{10} and x_{90} are the knife-edge positions along a given (*e.g.* horizontal or vertical) diameter of the beam where 10 and 90% of the total beam power is transmitted (*cf.* dashed lines in Figure 3.5) and 1.28 is the value at which the Gaussian distribution equals 0.1 and 0.9. Using the profiles shown in the Figure, $w(z)$ was estimated to be about 1.4

mm and 1.5 mm along the horizontal and vertical, respectively. These values are slightly higher than the value of 1.2 mm given by the manufacturer 1 cm from the exit of the laser head, presumably due to the divergence of the beam, which is given by the manufacturer as 2.4 mrad. Note that the profiles shown in Figure 3.5 were measured about 1.2 m from the exit of the laser head.

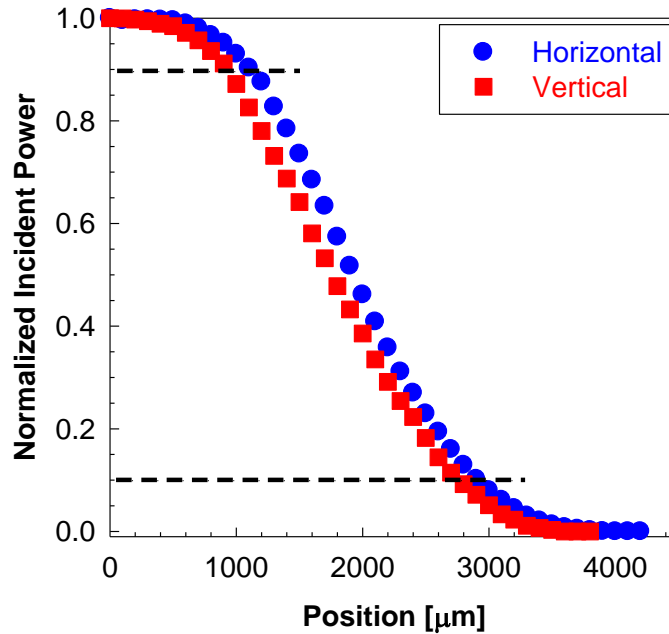


Figure 3.5. The normalized incident power as a function of the position of the razor blade when translating the knife-edge along the horizontal (*blue circles*) and vertical (*red squares*) directions. Two dotted lines represent 10 and 90% of the total beam power, respectively.

Figure 3.6 shows the output power at $\lambda = 514$ nm of the argon-ion laser (543-MA-A03, Melles Griot) over 8 h measured by the internal power meter built into the laser, which uses a photodiode to monitor the power of a small fraction of the laser beam. The power readings, which were sampled at 2 Hz with a data acquisition system (HP34970A, Agilent Tech.), suggest that the laser output power varied by no more than 0.02 % over the 8 h after the laser was turned on, and by less than 0.01% over 7 h if the laser was allowed to warm up for 1 h after startup. All the experiments shown here were therefore

performed after turning on the laser and waiting for 1 h.

Similar calibrations were performed to characterize the stability of the evanescent-wave illumination for the imaging system used in the EFT experiments. The results showed that the output power of the air-cooled argon-ion laser coupled to the optical fiber (543-GS-A03, CVI Melles Griot) varied by less than 0.1% over 6 h as measured at the output end of the fiber if the laser was again allowed to warm up for 1 h after startup.

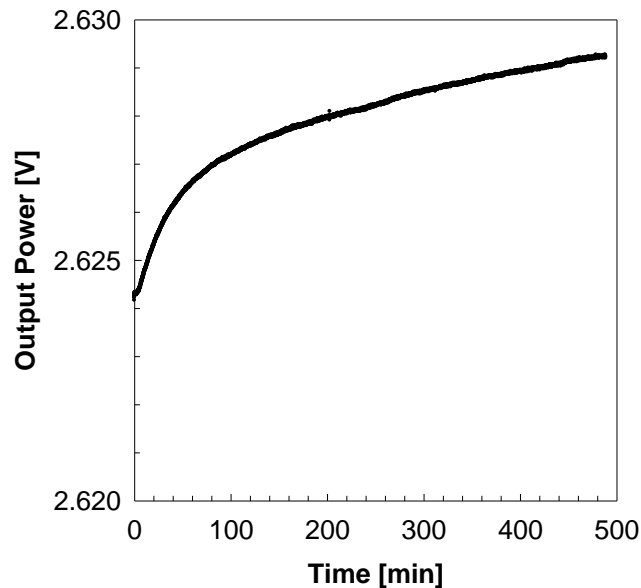


Figure 3.6. The output power from the argon-ion laser (543-MA-A03, Melles Griot) measured by the laser power meter as a function of time.

3.2.2 Imaging Systems

Figure 3.8 depicts the imaging system for the EFT experiments. The fluorescence from the FI solution illuminated by evanescent waves at $\lambda = 514$ nm with a penetration depth $z_p \approx 80$ nm were isolated by an epi-fluorescent bandpass filter cube (hq550/40m + zq514rdc, Chroma Tech.) that transmitted light at $\lambda = 530$ – 570 nm (and reflected the 514 nm illumination), then imaged by the TIRF objective onto an electron multiplying CCD (EMCCD) camera (Cascade 650, Photometrics) and recorded as 16-bit 653×492 pixel

images on the hard drive of a personal computer. The nominally 16-bit images, which have a maximum grayscale value of ~ 53000 (I_o), had a typical bias noise level of 1000 (I_{\min}). Based on the exponential decay of the evanescent-wave intensity, $I_{\min} / I_o = 0.019 = \exp\{-z_{\max} / z_p\}$, where z_{\max} is the farthest from the wall that signals excited by the evanescent wave can distinguished above the noise “floor. Solving, $z_{\max} \approx 4z_p$, suggesting that the z -extent of the region illuminated by the exponentially decaying evanescent waves is the first 320 nm next to the wall since $z_p \approx 80$ nm (*cf.* section 3.2.1).

To estimate equivalent illumination depth of evanescent waves \bar{z} , namely the thickness of imaging depth which the fluorescence is imaged to the CCD camera, we used the equation:

$$\bar{z} = \frac{\int_0^{4z_p} z e^{-z/z_p} dz}{\int_0^{4z_p} e^{-z/z_p} dz} \quad (3-4)$$

and obtained $\bar{z} = 0.93z_p$. This suggests that the evanescent wave can penetrate up to $\sim z_p$ and the fluorescence intensities within $\sim z_p$ is actually imaged. Although z_p varies with fluid temperature because the refractive index of the fluid varies with temperature, the penetration depth varied by no more than 1 nm for temperatures between 20 °C and 60 °C. The components of the imaging system are listed in Table 3.3.

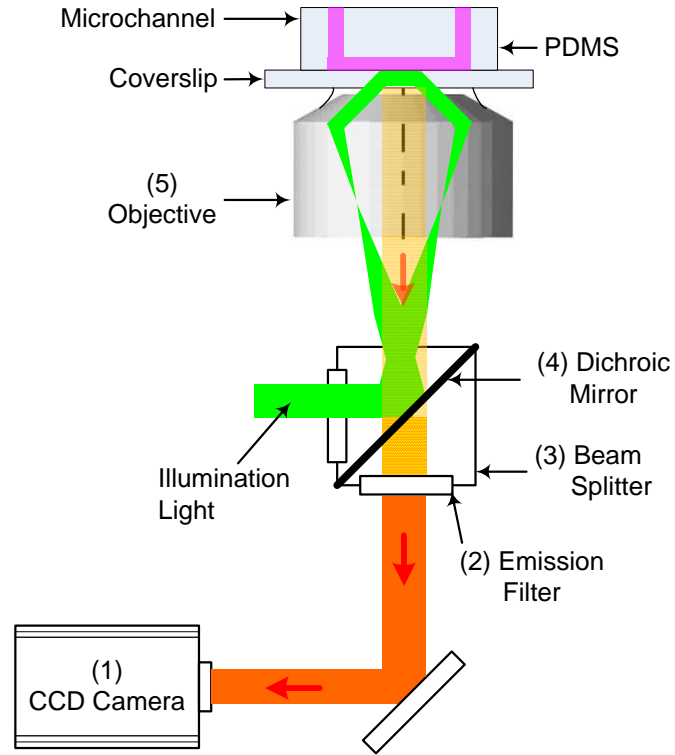


Figure 3.7. Sketch of the imaging systems used in the EFT studies.

Table 3.3. Components of the imaging system for the EFT studies

Label	Item	Manufacturer	Model	Notes
1	Camera	Photometrics	Cascade 650	16 bit, 492×652 pixels
2	Emission Filter	Chroma Technology	Hq550/40m	
3	Beam Splitter	Chroma Technology	C122968	Custom
4	Dichroic Mirror	Chroma Technology	Zq514rdc	
5	Objective	Olympus	PlanApo N	60×
	Microscope	Olympus	IX71	TIRF microscope

In the imaging system used in the DFT studies (Figure 3.8), the fluorescence from

Fl and SrB was isolated by a bandpass filter (NT48-083, Edmund Optics) that transmitted light at $\lambda = 529\text{--}555\text{ nm}$ and a longpass filter (NT47-618, Edmund Optics) that only transmitted light at $\lambda \geq 600\text{ nm}$, respectively, and imaged by an inverted microscope (Leica DM IL) through a 10x magnification, 0.25 NA objective (506084, N Plan, Leica) and a 0.5 \times camera adaptor, onto an EMCCD camera (Cascade 650, Photometrics) and recorded 16-bit 653×492 pixel images on a PC HD. Both the bandpass and longpass filters reflected the 514 nm illumination, ensuring that only the fluorescence emission were recorded by the EMCCD. In all cases, the Fl and SrB emissions were recorded within a few seconds of each other by manually switching between the two different filters. The components of the imaging system used in the DFT experiments are tabulated in Table 3.4.

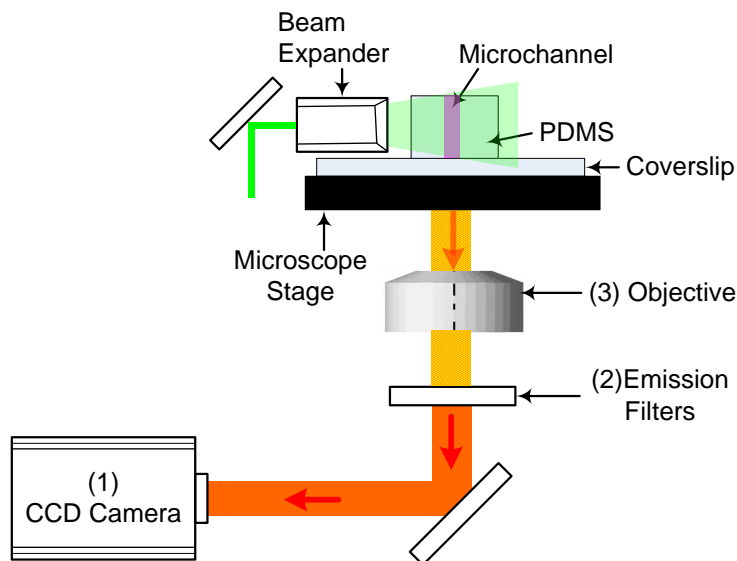


Figure 3.8. Sketch of the imaging systems used in the DFT studies.

Table 3.4. Components of the imaging system for the DFT studies

Label	Item	Manufacturer	Model	Notes
1	Camera	Photometrics	Cascade 650	16 bit, 492 × 652 pixels
2	Emission Filters	NT48-083	Edmund Optics	For I_{Fl}
		NT47-618	Edmund Optics	For I_{SrB}
3	Objective	Leica	506084	N Plan
	Microscope	Leica	DM IL	Inverted microscope

3.2.2.1 Effect of Dye Concentration on Fluorescence Intensity

As explained in Section 2.1.1, the fluorescence intensity depends on the illumination intensity and the fluorescent dye concentration, among other properties. For dilute fluorophore solutions, the fluorescence intensity becomes directly proportional to these parameters. Experimental calibrations were carried out to determine the maximum Fl and SrB concentrations where the fluorescence is still proportional to the intensity using volume illumination.

Aqueous solutions of Fl and SrB at molar concentrations ranging from 0.1 $\mu\text{mol/L}$ to 200 $\mu\text{mol/L}$ were driven by the syringe pump through the 1 mm square channel at a flow rate of 33.3 $\mu\text{L/s}$ ($Re = 33.3$) to minimize any photobleaching, and volumetrically illuminated by an argon-ion laser beam at 514 nm with an output power of 60 mW. Two sequences of 100 images each of the fluorescence were recorded by the EMCCD camera at two different exposure times, 1 ms and 20 ms, to quantify photobleaching effects. The averaged emission intensity from each fluorophore is shown as function of dye concentration in Figure 3.9. For Fl, the emission intensity varies linearly with concentration for molar concentrations up to 200 $\mu\text{mol/L}$; linear regression of the data

gave $R^2 = 99.9\%$ for both exposure times. The SrB emissions are, however, only linearly proportional to the molar concentration for concentrations up to $50 \mu\text{mol/L}$; linear regression of these data gave $R^2 = 99.9\%$ (again for both exposure times). Based on these calibrations, the molar concentrations of FI and SrB used in the DFT experiments were $5 \mu\text{mol/L}$, and the molar concentration of the FI used in the EFT experiments was $30 \mu\text{mol/L}$. In all cases, these values are well within the range where the fluorescence emissions are directly proportional to the illumination intensity, at least based on the experiments with volume illumination.

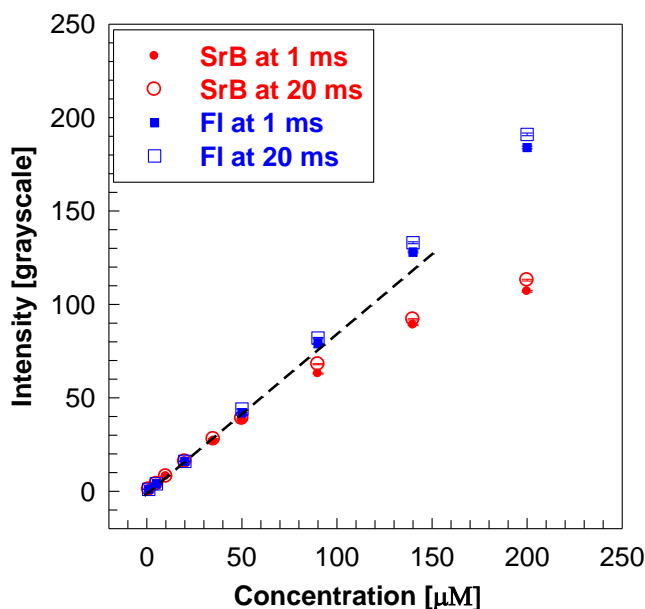


Figure 3.9. The emission intensities from FI and SrB as a function of concentration of the dye solution at two different exposure time, 1 and 20 ms.

3.2.2.2 Imaging System Magnification

In theory, the effective magnification of the imaging system used for the DFT studies should be the product of the magnification of the objective, 10, and that of the camera adaptor, 0.5, or 5. To verify this magnification, a scale marked at $20 \mu\text{m}$ intervals was imaged by the EMCCD camera through the microscope objective and the camera

adaptor, as shown in Figure 3.10. A discrete Fourier transform (DFT) of this image gives a spatial frequency of $0.07312 \text{ pixel}^{-1}$, corresponding to the spatial frequency for the scale, which should be $1/(20 \mu\text{m})$. Since the pixels of the EMCCD are $7.4 \mu\text{m}$ square, the effective magnification of the imaging system is 5.06, or each pixel spans $1.4624 \mu\text{m}$ in the object plane.

The effective magnification of the imaging system used for the EFT studies should be product of the objective magnification of 60 and the camera adaptor magnification of 0.5, or 30. Images of the same scale acquired using this objective and camera adaptor were found to have a spatial frequency (again obtained using a DFT) of $0.01234 \text{ pixel}^{-1}$. The effective magnification of this imaging system is 29.97, corresponding to $0.2469 \mu\text{m}/\text{pixel}$.

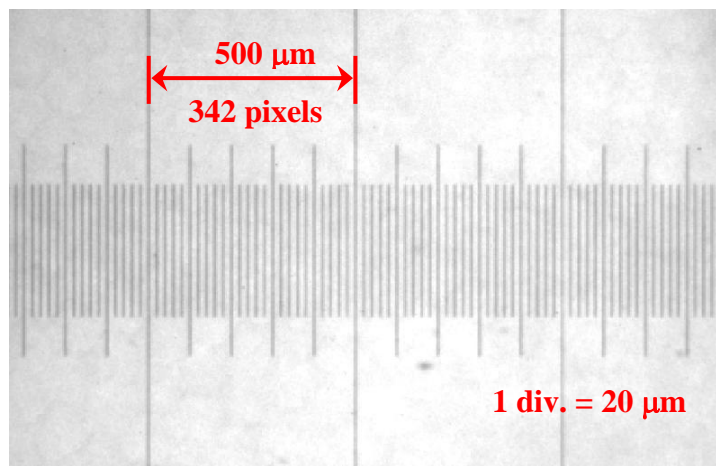


Figure 3.10. A sample image of the scale marked in $20 \mu\text{m}$ increments obtained with the imaging system used for the DFT experiments.

3.2.2.3 *Depth of Field*

The depth of field of a microscope system is defined to be the distance between the nearest and farthest object planes that are considered to be in focus. Inoué and Spring (1997) estimated the total depth of field to be the sum of the depths of field due to diffraction and geometric affects:

$$\delta z = \frac{n\lambda}{NA^2} + \frac{ne}{M \cdot NA} \quad (3-5)$$

where n is the index of refraction of the immersion medium (*e.g.* oil, air) between the specimen and the objective lens, λ is the wavelength of the imaged light in a vacuum, NA is the numerical aperture of the objective lens, M is the total magnification of the system, and e is the smallest resolvable distance of the imaging system which in these studies is the size of single pixel in the EMCCD camera (so $e = 7.4 \mu\text{m}$). For the EFT imaging system, $n = 1.52$, $\lambda = 514 \text{ nm}$, $M = 30.3$ and $NA = 1.45$, giving $\delta z = 14 \mu\text{m}$ for. For the DFT imaging system, $n = 1$, $\lambda = 514 \text{ nm}$, $M = 5.06$, and $NA = 0.25$, giving $\delta z = 20 \mu\text{m}$.

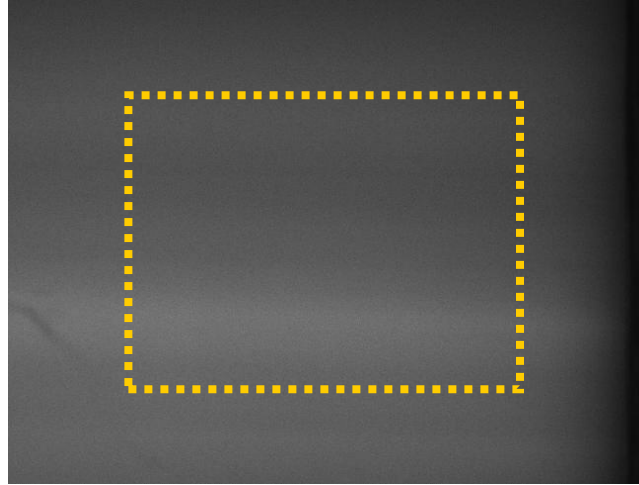


Figure 3.11. A typical grayscale image of volumetrically illuminated $5 \mu\text{M}$ FI; flow goes from top to bottom in this image. The grayscale value V at a given laser power P was calculated by averaging the grayscale values for all the pixels inside the rectangular region (300×400 pixels) in the center of the channel.

3.2.2.4 EMCCD Camera Calibrations

In this thesis, the solution temperature is estimated from variations in the emission intensity from fluorescence dye solutions excited by volumetric or evanescent wave illumination and recorded by an EMCCD camera. Accurately quantifying the relationship between the grayscale recorded by the EMCCD and the fluorescence incident upon the EMCCD is therefore critical in accurately estimating the temperature of

the solution.

Two FI solutions in DI water at molar concentrations of 5 μM and 20 μM were driven by a syringe pump (NE-500, New Era Pump System, Inc.) at $Re = 33.3$ (again to minimize photobleaching) through the 1 mm square channel and volumetrically illuminated by a light sheet formed from a 60 mW argon-ion laser beam at $\lambda = 514$ nm. The fluorescence from the FI was then imaged the same system used for the DFT studies. A sequence of 100 images was recorded under otherwise identical conditions on the EMCCD at various illumination levels, controlled by changing the output power P , measured by a power meter (Lasermate Q, Coherent), from $P_{min} = 0.01$ W to $P_{max} = 115$ mW, a level where the camera pixels became saturated. Experiments were performed under otherwise identical conditions at two different EMCCD gain values (G_M), 3200 and 2700, to verify that the camera response was consistent at different gains.

A spatially and temporally averaged grayscale value V was calculated over a rectangular 300×400 pixel region in the center of the channel (Figure 3.11) and over all 100 images in the sequence. This average grayscale and the laser output power (which should be proportional to the laser power incident upon the camera) were normalized as follows:

$$V_n = \frac{V - V_d}{V_{max} - V_d} \quad (3-6)$$

$$P_n = \frac{P - P_{min}}{P_{max} - P_{min}} \quad (3-7)$$

where V_d is the dark noise of the camera, determined by calculating the average grayscale value at P_{min} and V_{max} is the average grayscale value at P_{max} . In these calibrations, $V_d \approx 1045$ out of a maximum grayscale value of 65536 in the 16-bit images.

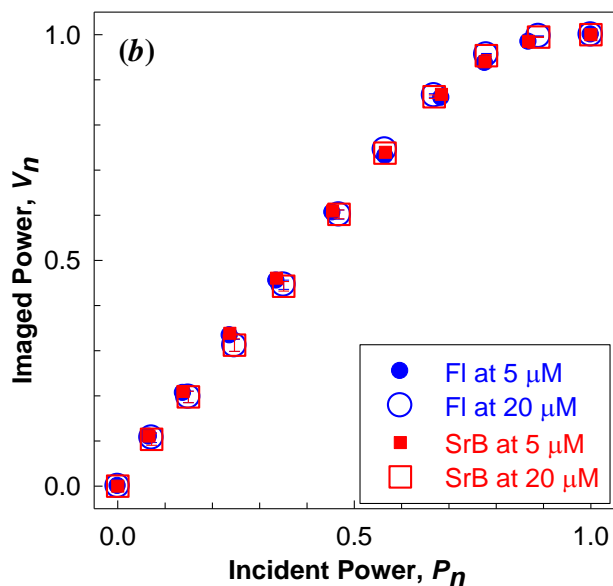
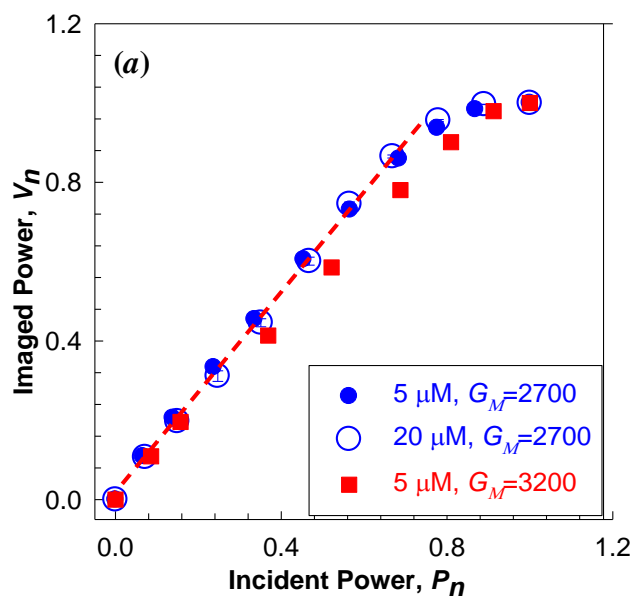


Figure 3.12. Camera calibrations showing the normalized incident laser power P_n as a function of the normalized grayscale value V_n for FI solutions at molar concentrations of 5 μM (*solid circles*) and 20 μM (*open circles*) excited at 514 nm at two different camera multiplication gain at $G_M = 2900$ (*circles*) and 3200 (*squares*) (a). Figure (b) shows the relationship between V_n and P_n at 5 μM (*open symbols*) and 20 μM (*closed symbols*) with two different dyes, FI (*circles*) and SrB (*squares*), at a EMCCD gain of 2700. The standard deviation in all cases is smaller than the symbols. The dashed line in figure (a) represents $V_n = P_n$.

Figure 3.12(a) shows the normalized grayscale value V_n as a function of the normalized incident power P_n on the Cascade 650 CCD camera at $G_M = 2700$ for two difference concentrations, 5 and 20 μM . Clearly, the response of the CCD becomes nonlinear for $P_n > 0.75$, as can be seen by the deviation of the data from the expected linear behavior $V_n = P_n$ denoted by the red dashed line. The FI concentration appears to have no effect upon the camera response. Figure 3.12(b) shows results obtained from images of the emissions from FI and SrB, which have different emission bands, with emission peaks at 491 nm and 514 nm, respectively. The different emission bands appear to have no effect upon the camera response.

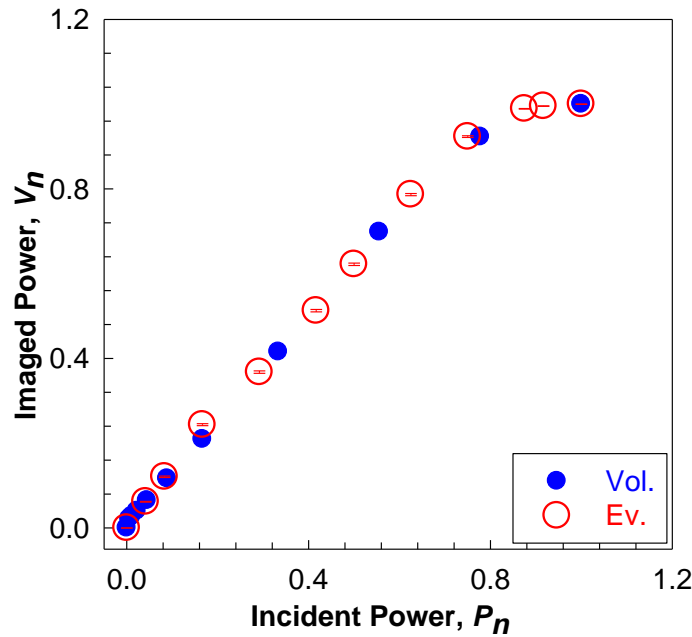


Figure 3.13. Camera response for images of 5 $\mu\text{mol/L}$ and 20 $\mu\text{mol/L}$ FI illuminated by volumetric (Vol) and evanescent wave (Eva) illuminations, respectively, at $G_M = 2700$. The standard deviation is smaller than the symbols.

Similar calibrations were performed for FI illuminated by evanescent waves (imaged using the same setup as that used for the EFT experiments), since the intensity

distribution of the evanescent wave along the optical axis is very different from that of the volumetric illumination. Figure 3.13 compares the response of the EMCCD for FI excited by volume and evanescent-wave illuminations. The results suggest that the camera response is not affected by the type of excitation.

In summary, the normalized camera response appears to be unaffected by the type of fluorophore and hence fluorescent emission, the concentration of the fluorophore, the camera gain setting, and the type of excitation: in all cases, the camera response was identical within 0.1%. The camera response was therefore curve-fit following previous work (Li, 2008) to the ratio of a 2nd-order polynomial and a 3rd-order polynomial:

$$P_n = \frac{-55.92V_n^2 + 56.57V_n + 0.0842}{V_n^3 + 1.2V_n^2 - 72.61V_n + 71.15} \quad (3-8)$$

with $R^2=99.9\%$ and adjusted $R^2=99.9\%$ (Figure 3.14).

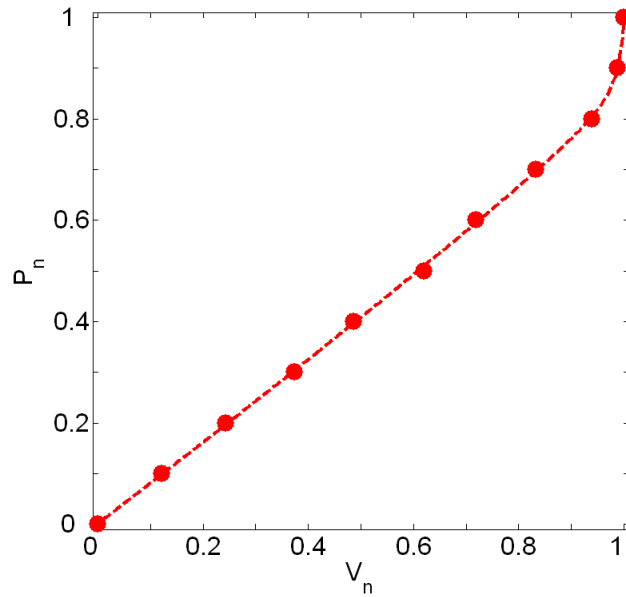


Figure 3.14. Camera response curve showing the measured normalized incident power P_n as a function of the resultant normalized imaged grayscale value V_n (points) and a curve-fit to these data (dashed line) given by Eq. (3-6).

Because the solution temperature is estimated from variations in fluorescence

intensities as recorded by an EMCCD camera, it is also important to quantify the effects of any spatial variations in the sensitivity of the camera pixels themselves. If the sensitivity of the camera pixels does not vary over time, variations in pixel sensitivity will be canceled by taking the (pixel by pixel) ratio of the grayscale values of two images, since the grayscale value recorded by a pixel is proportional to its sensitivity. In the EFT studies, the solution temperature is estimated from the ratio of two images, namely one with a temperature gradient due to power being supplied to the heater, and an otherwise identical image with the heater off. Variations in pixel sensitivity should therefore have little, if any, effect on the accuracy of the raw EFT data.

To verify this, the two sequences, each 100 images long, of the EFT calibration images, acquired at two different (constant) reference temperatures, specifically $T = 20$ and 60 °C, at different time were processed. After temporally average over each 100 images, the ratio of two average images was obtained and the spatial variations in pixel sensitivity over time were estimated by calculating the standard deviation of the ratio values over the entire image. The estimated standard deviation was 2.0%, corresponding to 310 in 16bit grayscale value. Considering that the typical grayscale value of FI at 20 °C, the lowest value since the emission intensity of FI increases with increasing temperature, was ~15000 and the standard deviation of the temperature calibration was ~750 in 16bit grayscale value, the variation of 2.0% in pixel sensitivity over time has little effect to variations in recorded fluorescence intensity to the CCD camera.

In the DFT studies, however, the solution temperature is estimated from the ratio of two images of the emissions from FI and SrB obtained over different wavelength bands, and it is unclear if the sensitivity of the pixels is independent of wavelength. To estimate this effect, the two sequences, each 100 images long, of the DFT calibration images for FI and SrB, acquired at a constant temperature $T = 20$ °C at a few seconds difference were temporally averaged and used to take a ratio of average image.

Assuming that the temporal variation of the pixel sensitivity over a few seconds is negligible from the discussion in the previous paragraph, the spatial variations in pixel sensitivity at different wavelengths can be quantified by estimating the standard deviation of the ratio values over the image. The estimated standard deviation was 1.9% and this variation is still lower than 2% of temporal variation in the pixel sensitivity suggesting that the variation in pixel sensitivity of the CCD at different wavelength is negligible.

In the ideal case where each pixel has the same sensitivity, the standard deviation of the grayscale values over the single image reaches to zero as long as the illumination intensity is uniform over the entire CCD sensor at constant concentration of the solution. To quantify spatial variations in pixel sensitivity, a sequence, 100 images long, of DFT calibration images taken at constant solution temperature $T = 20\text{ }^{\circ}\text{C}$ was temporally averaged as shown in Figure 3.15. Since it is impractical to assume uniform illumination over the entire image, the average image was divided into smaller window regions 34×34 pixels, for example, the region A and B in Figure 3.15, which the assumption of uniform illumination over the window is valid. The 34 pixels square is also equivalent size to the spatial resolution at which the temperatures in DFT studies was estimated. By randomly selecting the square windows over the entire image except the black region of the side wall, the standard deviation over the each 34 pixels square was calculated and compared to those in different windows. The typical standard deviation ranges $1.6\sim 1.7\%$, corresponding to 380 in 16 bit grayscale value. Note that the average grayscale value of SrB image at $20\text{ }^{\circ}\text{C}$ was ~ 23000 in 16 bit. The variation in standard deviations in different windows was 0.1% , 23 in 16 bit grayscale. Hence, the variation of 0.1% in different windows is negligible and this suggests that the pixel sensitivity of the CCD sensor is almost uniform at least based on our estimation.

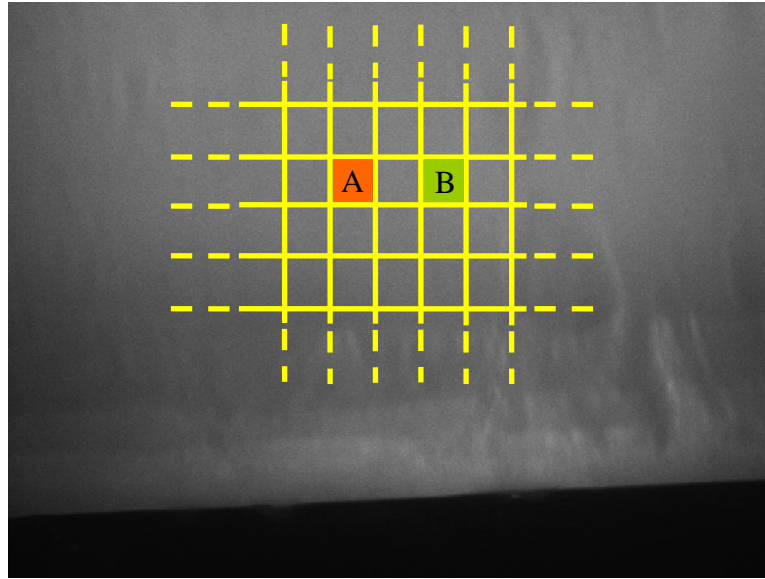


Figure 3.15. An average calibration image of SrB at $T = 20\text{ }^{\circ}\text{C}$ over 653×492 pixel ($954\text{ }\mu\text{m} \times 718\text{ }\mu\text{m}$) grayscale at an exposure of 20 ms. The image was divided into 34×34 pixel window region, namely the squares including A and B, to compare the standard deviation of these windows over the entire region. The black region on the bottom of the image is the sidewall of the channel.

In summary, the effect of variations in pixel sensitivity of CCD camera due to time, wavelength, and space was evaluated using calibration images in EFT and DFT studies. These three effects on the variation of pixel sensitivity were found to be negligible compared to experimental uncertainties in temperature calibrations and measurements of wall and coolant temperatures.

CHAPTER 4

Evanescent Wave-Based Fluorescence Thermometry

This chapter describes a thermometry technique for measuring wall surface temperature distributions using evanescent wave-based fluorescence thermometry (EFT). Section 4.1 introduces evanescent waves. Section 4.2 describes calibration studies of how the fluorescent emissions from an aqueous solution of fluorescein (Fl) illuminated by evanescent waves depend on the solution temperature. Section 4.3 then describes and briefly discusses the EFT experiments. The EFT results are compared to predictions from FLUENT[®] simulation in Section 4.4, followed by a short discussion. Finally, Section 4.5 summarizes the chapter.

4.1 Total Internal Reflection Fluorescence Microscopy

To measure liquid temperature fields near the wall, this thesis uses evanescent-wave illumination, which typically illuminates only the first few hundred nanometers next to a refractive-index interface. Any fluorescence excited by evanescent waves must therefore originate in this thin region next to the wall. This section gives the theoretical background of evanescent waves and their characteristics.

4.1.1 Total internal reflection

As a light ray propagates through different isotropic media, it usually changes both its speed of propagation and its direction. The change in the propagation speed is quantified by the refractive index (n), which is the ratio of the speed of light in a vacuum to that in the material. When a ray of light travels from medium 1 with refractive index n_1 such as glass to medium 2 with refractive index $n_2 > n_1$ such as water, it is partially reflected and also partially refracted at the glass-water interface (Figure 4.1). The

direction of the refracted ray, measured with respect to the direction normal to the interface, is given by Snell's Law

$$n_1 \sin \theta_i = n_2 \sin \theta_t \quad (4-1)$$

where θ_i is the angle of incidence describing the direction of the ray in glass and θ_t is the angle of refraction describing the direction of the ray in water. Since the sine of an angle cannot exceed unity, Snell's Law gives an upper limit on the angle of incidence for which refraction occurs. This angle, known as the critical angle θ_c , is given by the following relation:

$$\theta_c = \sin^{-1} \left(\frac{n_2}{n_1} \right) \quad (4-2)$$

When $\theta_i \geq \theta_c$, all of the light is reflected at the glass-water interface (Fig. 4.2b), a phenomenon known as total internal reflection (TIR). For a borosilicate glass ($n_1 = 1.52$)-water ($n_2 = 1.33$) interface, $\theta_c = 61.0^\circ$.

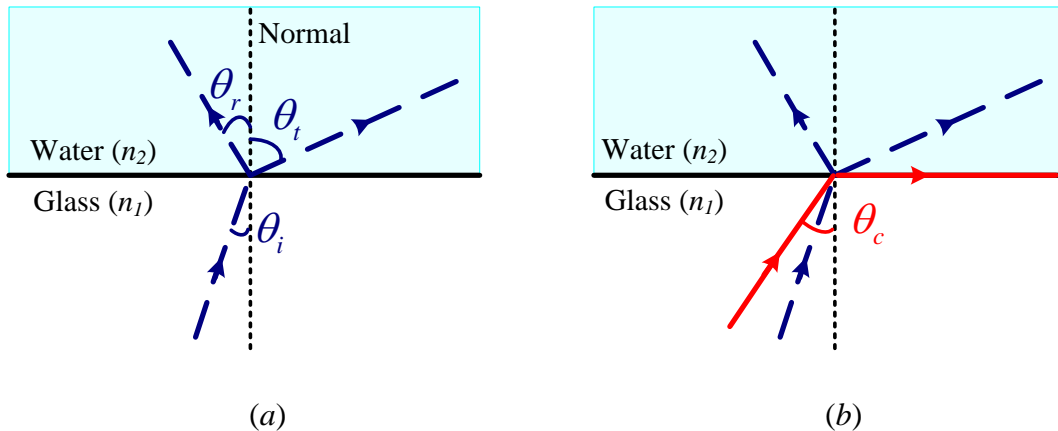


Figure 4.1: An illustration of Snell's law (a) and total internal reflection (TIR) (b) for the propagation of a ray of light near a glass-water interface.

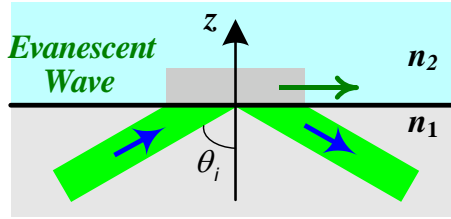


Figure 4.2: Generation of evanescent waves from TIR at the interface between two media with different refractive indices, n_1 and $n_2 (>n_1)$.

4.1.2 Evanescent wave

The Fresnel equations relations describe how electromagnetic waves (*i.e.*, light) are transmitted and reflected at the interface between two dielectric media with different indices of refraction. In all cases, the tangential component of both the electric and magnetic fields must be continuous across the interface. When TIR occurs, the portion of the electromagnetic wave with complex wavenumber is transmitted to the medium with the lower refractive index n_2 (*i.e.*, water) to satisfy this boundary condition. This so-called “evanescent wave” propagates parallel to the interface for a short distance (known as the Goos-Hänchen shift) before re-entering the medium with the higher refractive index n_1 .

Because the evanescent wave has a complex wavenumber, its intensity, $I(z)$, decays exponentially with distance z normal to the interface:

$$I(z) = I_0 \exp\{-z / z_p\} \quad (4-3)$$

where I_0 is the intensity at the interface ($z = 0$) and z_p , characterizing the length scale of the exponential decay, is the intensity-based penetration depth. The penetration depth

$$z_p = \frac{\lambda}{4\pi} \sqrt{n_1^2 \sin^2 \theta_i - n_2^2} \quad (4-4)$$

where λ is the wavelength of the illumination in vacuum. In most cases, z_p is comparable in order of magnitude to and less than λ . For a glass-water interface, $z_p \approx 100$ nm and

evanescent-wave illumination is therefore restricted to the first few hundred nm of water next to the glass surface.

Evanescent waves have been used in a variety of applications to probe interfacial particle dynamics, investigate cell-surface interactions and cell adhesion in biological applications. For example, Zettner and Yoda (2003) measured velocity fields in the rotating Couette flow of water within 380 nm of the stationary glass surface by illuminating 300 nm and 500 nm diameter polystyrene and silica particles with evanescent waves. Sadr *et al.* (2004) used a similar method to measure two components of the velocity field in the fully-developed and steady electro-osmotic flow (EOF) within about 100 nm of the channel wall in rectangular channels with depths of 5–25 μm . Le *et al.* (2007) described a monolithic and massive fabrication technique for a TIR-based biochip that can produce evanescent-wave illumination suitable for highly sensitive fluorescent imaging at very low cost.

However, we are unaware of any work using evanescent waves to measure temperatures using intensity-based FT. The next sections describe the wall surface thermometry technique based on EFT developed in this thesis including calibration results, EFT temperature measurements, and validation of the EFT results by numerical predictions.

4.2 Temperature Calibration for EFT Technique

This section describes the procedures for preparing the working fluid and the EFT temperature calibrations. The results and the accuracy of the wall surface temperatures measured with this method are then discussed.

4.2.1 Preparation of the working fluid

In the EFT studies, only one temperature-sensitive tracer, FI was used. In microscale

devices with their relatively large surface areas and small volumes, accurate intensity-based FT requires that the fluorophores have little, if any, surface adsorption on PDMS and glass surfaces since even a small amount of emissions from surface-bound fluorescent molecules can overwhelm the variations in fluorescent emissions due to temperature gradients, especially since the intensity of evanescent-wave illumination is maximum at the glass-water interface as explained in Section 4.1. Although a second tracer, such as SrB, should in theory improve the accuracy of the EFT results, as discussed previously, SrB was found to have a small amount of surface adsorption onto glass surfaces at moderate pH values.

In an attempt to find a second appropriate temperature-sensitive species, numerous fluorescent tracers which had intensities that decreased as temperature increased and could also be excited by 514 nm light were tested, as listed in Table 4.1, and all were unfortunately found, in aqueous solution with 30 or 50 $\mu\text{mol/L}$ fluorescein at various pH, to have at least some adsorption onto borosilicate glass surfaces (Gupta *et al.*, 2000). In these tests, the aqueous fluorescent dye solutions were buffered to pH 9.2 and 8.5 using 7 mmol/L sodium tetraborate ($\text{Na}_2\text{B}_4\text{O}_7$, ACS reagent grade, Acros Organics) and 0.1 mol/L phosphate buffer composed of sodium phosphate dibasic dihydrate (71643, Sigma-Aldrich) and sodium phosphate monobasic monohydrate (71504, Sigma-Aldrich), respectively.

Most of the fluorophores in the rhodamine family, including SrB and RhB, have at least some adsorption on negatively charged glass surfaces due to their being zwitterions with both positively and negatively charged portions in solution (Ramette and Sandell, 1956). Fluorescein, on the other hand, is negatively charged in aqueous solution with a valence of 1 at moderate pH, and has a valence of 2 at pH values above about 8.5 (Haugland, 2002).

The slight adsorption of SrB had a negligible effect on the accuracy of the FT results with volume illumination, and so the combination of the two fluorophores gave greater

temperature sensitivity and accuracy, as discussed previously. Even a minor amount of adsorbed SrB had a significant effect on the EFT results, and so only a single temperature-sensitive tracer, namely Fl was found to give the most accurate and reproducible temperature data.

Table 4.1. A list of the aqueous fluorescent dye solutions tested for adsorption on borosilicate glass surface at various concentrations and pH values. In all cases, these dyes were tested in solution with fluorescein at molar concentrations between 5 and 50 $\mu\text{mol/L}$.

Case	Fluorescent Dye	Catalog #	Manufacturer	$\mu\text{mol/L}$	pH
1	Sulforhodamine B	86183 Fluorescence grade	Fluka	5/10/30	8.5/9
2	Dichlorotris(1,10-phenanthroline)ruthenium(II)	343714-1G	Sigma	50	9.2
3	Rhodamine B	29657-0250	Acros Organics	5	9.2
4	5-carboxynaphthofluorescein	C652	Invitrogen	10	8.5
5	Sulforhodamine 640	25266	Exciton	50	8.5
6	LDS 698	60122	Exciton	5	8.5
7	Tris(2,2'-bipyridyl) dichlororuthenium(II)	244758- 250MG	Sigma	30	8.5

The aqueous solution of 30 $\mu\text{mol/L}$ Fl used in the EFT studies was kept at a pH of 8.5 (to ensure that the fluorophore in solution was negatively charged at a valence of 2) with phosphate buffer, which kept the pH of the solution at 8.5 ± 0.1 for the range of solution temperatures studied here of 20–60 °C. The solution was prepared by diluting a Fl stock solution at an intermediate molar concentration of 1 mmol/L. To prepare the stock

solution, a phosphate buffer was first prepared by adding the appropriate amounts of sodium phosphate dibasic dihydrate (71643, Sigma-Aldrich) and sodium phosphate monobasic monohydrate (71504, Sigma-Aldrich) salts, measured using a precision scale (Mettler Toledo type H4; resolution of 1 mg) to the appropriate volume of distilled deionized (DDI) water and stirring with a magnetic stirrer (33918-239, VWR). The pH value of the buffer solution was measured to be 8.5 using a handheld pH meter (WD-35614-20, Oakton Instrument). Next, the appropriate mass of disodium salt of Fl (FL116, Spectrum Chemicals) was added to the phosphate buffer solution. In all cases, the masses of the salts were determined from the equation:

$$C [\text{mol/L}] = \frac{m [\text{g}]}{V [\text{L}] \cdot MW [\text{g/mol}]} \quad (4-5)$$

where C and V are the molar concentration and volume, respectively, of the solution, and m and MW are the mass and molecular weight, respectively, of the salt. The pH value of the final stock solution was re-measured to ensure that the addition of the Fl salt had a negligible effect on the pH values of the final solution; in all cases, the change in pH was less than 0.1 pH units.

To make a Fl solution at the designated concentration, about 300 mL of DDI water prepared and appropriate amount of the phosphate dibasic and monobasic salts were then added to the diluted solution to keep the solution at a pH of 8.5. The final 30 $\mu\text{mol/L}$ Fl solution is then prepared by diluting the 1 mol/L stock with DDI water. After stirring the final solution with the magnetic stirrer for 1 min, the pH of the Fl-phosphate buffer solution was again verified by the pH meter. Finally, the fluorescent solution was filtered through a 1.5 μm pore size glass-fiber filter (09-804-70A, Grade G6, Fisher Scientific), then a 0.7 μm pore size glass-fiber filter (09-874-72, type GF/F, Fisher Scientific) in a Büchner funnel (Nalgene, 4280-0700) and degassed by placing the solution under a vacuum using a vacuum pump (model 2628VE44-598, Gardner Denver

Thomas) for at least 2 h. The final solution was used in the experiments in all cases within a few hours of preparation.

4.2.2 Experimental Setup

This section describes the channels used in these studies, and the calibration setup used for the EFT studies. Two different types of channels were used in this thesis: PDMS-glass channels that were fabricated by replica molding and acrylic-glass channels created by milling.

4.2.2.1 Channel Fabrication

The PDMS-glass channels consisted of a rectangular PDMS block molded with a channel trench sealed by a borosilicate glass lid with an indium tin oxide (ITO) thin-film heater. Polydimethyl siloxane (PDMS) is commonly used in the fabrication of microchannels because it: *i*) can be easily molded with features as fine as $O(1 \mu\text{m})$ at temperatures ranging from 20 °C to 150 °C (Duffy *et al.*, 1998), *ii*) is optically transparent at visible wavelengths, and *iii*) can seal reversibly to itself or irreversibly to other materials such as glass and Si after exposure to an oxygen plasma by covalently bonding to the other material. To create a mold to emboss a channel trench in PDMS, a positive “master” geometry with a channel 1 mm square and 20 mm long was created in the solid modeling software SolidWorks and converted to a file compatible to a computer-aided design (CAD) program (Figure 4.3). The master was then fabricated by stereolithography rapid prototyping using a liquid photopolymer resin cured by a scanning UV laser beam on a Viper si2 SLA (stereolithography) system (3D systems). After fabrication, the master was soaked in isopropyl alcohol for 1 h to remove any unpolymerized resin, then cured in an oven at ~100 °C for 2 h.

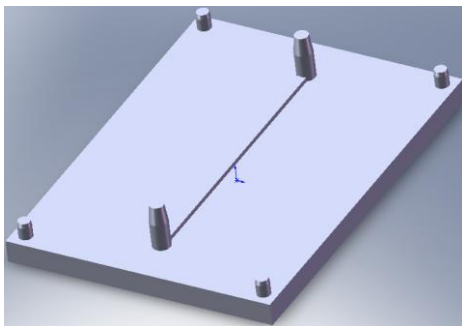


Figure 4.3. Drawing of the positive master for the PDMS channel trench created by SolidWorks. The diameters of the inlet and outlet ports are 2 mm. The four pins protruding from the corners are used to connect the master with the rest of the PDMS mold.

The channel trenches were then created in PDMS by replica molding. A 10:1 mixture of PDMS prepolymer and curing agent (Sylgard 184, Dow Corning, Midland MI) was stirred thoroughly, degassed under vacuum using a vacuum pump (model 2628VE44-598, Gardner Denver Thomas) for at least 1 h, and poured into a mold consisting of the master attached to a 25 mm × 25 mm × 5 mm rectangular box by the pins at the four corners (*cf.* Fig. 4.3) and cured for at least 6 h in an oven at 60 °C. The PDMS replica was then removed from the master. Although the nominal outer dimensions of the PDMS block were identical to those of the rectangular box, the nominal diameter of the inlet and outlet ports was 1.5 mm (*vs.* the 2 mm diameter of the ports in the positive master) due to slumping of the PDMS.

To fabricate the ITO heater with conductive (titanium, copper and gold) contact pads and an insulating dielectric top layer (SiO₂), glass substrates (C030401S, Matsunami Glass Ind., Ltd.) were first cleaned by induced-plasma etching for 30 s in a plasma thermal reactive ion-etching (RIE) system (Fig. 4.4). The ITO layer was deposited by a PVD75 RF sputterer through a 150 μm thick stainless steel mask (fabricated from an in-house CAD design by UTZ technologies, NJ) at 5 mTorr of argon gas at 100 W of RF power for 20 min. Although the nominal dimensions of the rectangular ITO heater was 6

mm \times 1 mm \times ~300 nm, the standard deviation in the thickness of the ITO within a single run of the RF sputterer was ~10 %, or 30 nm. In all cases, the thickness of the ITO layer was therefore measured after fabrication by a direct contact method using KLA-Tencor P-15 profilometer or by an optical method using Wyko profilometer. The thickness results from the two methods agreed in all cases within 1%. The sheet resistivity of the ITO heater, which was measured by a Signatone four-point probe, varied from 150 Ω /square to 200 Ω /square.

Titanium (Ti) and copper (Cu) layers with thicknesses of 50 nm and 4 μ m, respectively (as measured by Tencor profilometer), were deposited at the ends of the ITO heater through a metal mask by the CVC DC sputterer for 2 h. The glass substrate containing the ITO and Ti/Cu films was then cleaned by methanol and etched for 30 s in the RIE system to remove any surface impurities, and a 500 nm gold (Au) layer was deposited on top of the Cu layer to protect it from oxidation and provide better bonding strength for the solder connections using the CVC E-beam evaporator at rate of 1.5 \AA /s for 1 h. Finally, a 500 μ m thick insulating layer of silicon dioxide (SiO₂) was deposited on top of the ITO film and part of the Ti/Cu/Au layer through a metal mask with the CVC E-beam evaporator.

The molded PDMS block and the glass substrate were cleaned by rinsing in methanol, then DI water, and drying under a stream of nitrogen (N₂) gas. They were then both oxidized for 90s by a plasma thermal reactive ion etcher. Immediately after removal from the plasma etcher, the PDMS and glass were then pressed together to irreversibly seal the channel by the strong covalent Si-O-Si bonds between the silanol groups (Si-OH) on the PDMS and glass surfaces (McDonald *et al.*, 2000). Creating silanol groups on the PDMS surface by exposing it to oxygen plasma also makes the PDMS surface hydrophilic, and negatively charged in the presence of aqueous solutions. Finally, electrical wires were soldered on the contact pads to supply electric power to the ITO

heater.

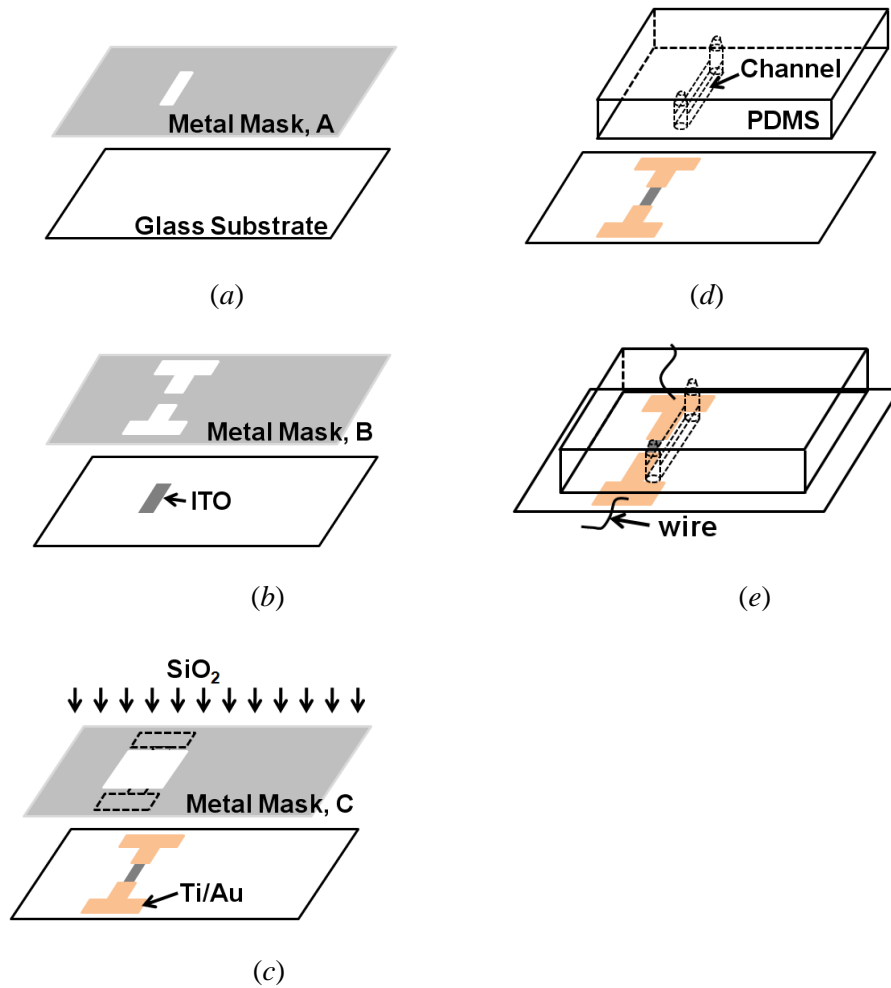


Figure 4.4. The steps to fabricate the ITO heater on a glass substrate. (a) After cleaning the surface of the borosilicate glass substrates by plasma etching, the ITO film (nominal dimensions $6 \text{ mm} \times 1 \text{ mm} \times 300 \text{ nm}$) was deposited on the glass substrate through a metal mask containing the design of the heater configuration by the PVD75 RF sputterer. (b) Layers of conductive Ti, Cu and Au (typical thicknesses of 50 nm, 4 μm , and 500 nm, respectively) were deposited on both sides of the ITO film in both sides to provide contact pads. (c) After cleaning impurities from the glass substrate by exposing it again to an induced plasma, a 500 nm thick silicon dioxide (SiO_2) layer was deposited over the ITO and Ti/Au/Cu layers to insulate the heater and most of the contact pads. (d) The PDMS block containing a negative relief of the channel was sealed onto the glass substrate after both were exposed to oxygen plasma. (e) Finally, electrical wires were soldered on the conductive layer to supply power to the ITO heater.

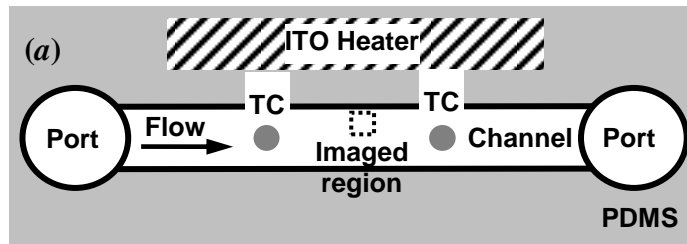
For the acrylic-glass channels, the channel trenches were machined into an acrylic (8560K265, McMaster Carr.) block with nominal dimensions of 13 mm \times 25 mm \times 5 mm 4 mm from the center of the block (*cf.* Fig. 4.22) using a 0.4 mm diameter end mill. Inlet and outlet ports were then bored into the ends of the channel using a 2 mm diameter end mill. A borosilicate glass substrate with the ITO heater and conducting pads, fabricated as described previously, was, after cleaning by methanol and DDI water, attached to the acrylic block using a UV-curable optical adhesive (Optical adhesive 81, Norland Products) that was cured by exposure to UV light for 4 min. Fittings (2808K101, ID 2 mm, McMaster-Carr) were attached to the inlet and outlet ports with epoxy (353NDT 80Z Kit part A, B, Epoxy Technology). As the final step, electrical wires were soldered to the contact pads.

4.2.2.2 Temperature Calibration Setup

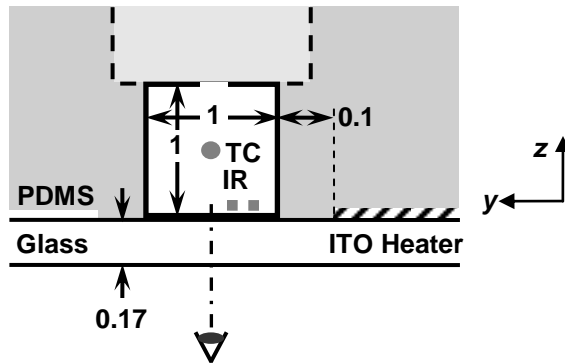
Figure 4.5 shows a schematic of experimental apparatus used for the temperature calibrations and for measuring (near-) wall surface temperature fields with evanescent-wave illumination. The channels used here, with cross-sectional dimensions of 1 mm \times 1 mm and a length of 20 mm, were fabricated as explained previously. For the EFT calibrations and experiments, the ITO heater edge was 0.1 mm from the side wall of the channel.

During the temperature calibrations, no power was supplied to the ITO heater. The temperature of the working fluid was controlled instead by passing the fluid through a heat exchanger consisting of a coil of 15 m of 1.5 mm ID copper tubing submerged in a temperature-controlled water bath (GH-D8, Haake). The fluid passed through 0.8 mm ID silicon tubing (51134K14, McMaster-Carr) connected to a Luer-Lok tip (14-823-31, Fisher Scientific) and a reducing tube coupling (5121K261, McMaster, Carr) attached to the heat exchanger, which was connected at its other end to more 0.8 mm silicon tubing and a fitting (2808K101, ID 2 mm, McMaster-Carr) inserted into the inlet port of the

channel, then exited the channel through 0.8 mm silicon tubing attached to the outlet port. The flow through the channel, the heat exchanger and the other components was driven by a syringe pump (NE-500, New Era Pump System, Inc) at a flow rate $Q = 67 \mu\text{L/s}$, corresponding to a Reynolds number based on the channel dimension $L = 1 \text{ mm}$ and the average velocity $Re \equiv Q/(Lv) = 67$, where v is the fluid kinematic viscosity. For each calibration experiment, and for each actual FT experiment, the ambient or room temperature was measured by a K-type TC (KMTSS-022G-6, Omega Eng.).



(a) Top view



(b) Cross-sectional View

Figure 4.5. Top (a) and cross-sectional (b) views of the PDMS-glass channels with thin-film ITO heaters. The dotted rectangle in the top view and the thick dotted line the cross-sectional view represent the imaged region (IR). Flow goes from left to right in the top view, and out of the page in the side view, as indicated. All dimensions are given in mm. The two TCs are about 12 mm apart and placed roughly symmetrically upstream and downstream of the IR.

The fluid temperature was determined by the set point temperature of the water

bath and monitored in the channel by two T-type thermocouples (TCs) (HYP1-30-1/2-T-G-60-SMPW-M, Omega Engineering, Inc.) with a bead diameter of 0.3 mm placed symmetrically upstream and downstream of the imaged region roughly in the center of the channel with a streamwise spacing of about 12 mm, as shown in Figure 4.5. The TCs were calibrated to an accuracy of 0.2 °C, and the TC readings were recorded by an A/D data acquisition board (HP34970A, Agilent Technologies) onto a PC HD. In all cases, images were acquired at least 20 min after the flow was started by turning on the syringe pump.

4.2.3 Temperature Calibration Results

The channel was mounted on the stage of an inverted total internal reflection fluorescence (TIRF) microscope (IX 71, Olympus) and illuminated by evanescent waves at a wavelength $\lambda = 514$ nm with a penetration depth $z_p \approx 80$ nm formed by a 60 \times /NA 1.45 TIRF objective (PlanApo N, Olympus) from the optical fiber-coupled beam of an air-cooled argon-ion laser (543-GS-A03, CVI Melles Griot) as shown in Figure 3.4. The laser output power was less than 20 mW in all cases to avoid damaging the objective. The FI concentration in the EFT studies, 30 $\mu\text{mol/L}$, was low enough so that the fluorescence intensity was proportional to the illumination intensity, as shown in Figure 3.9.

The FI emissions were transmitted by an epifluorescent bandpass filter cube (hq550/40m + zq514rdc, Chroma Tech.), that transmitted light at $\lambda = 530\text{--}570$ nm and reflected the 514 nm illumination, and imaged by the TIRF objective onto the EMCCD camera with 0.5 \times camera adaptor and recorded as 16-bit 653 \times 492 pixel images on the hard drive of a personal computer. The magnification of the imaging system was 29.97, corresponding to 0.2469 $\mu\text{m/pixel}$ (Sec. 3.2). The nominally 16-bit images, which have a maximum grayscale value of ~ 53000 , had a typical bias noise level of 1000, suggesting

that the extent of the region illuminated by the exponentially decaying evanescent waves was about $4z_p$ (*cf.* section 3.2), or the first 320 nm next to the wall. Although z_p varies with fluid temperature (because the refractive index of the fluid varies with temperature), the penetration depth varied by no more than 1 nm for the range of solution temperatures T studied here, where $T = 20\text{--}60$ °C.

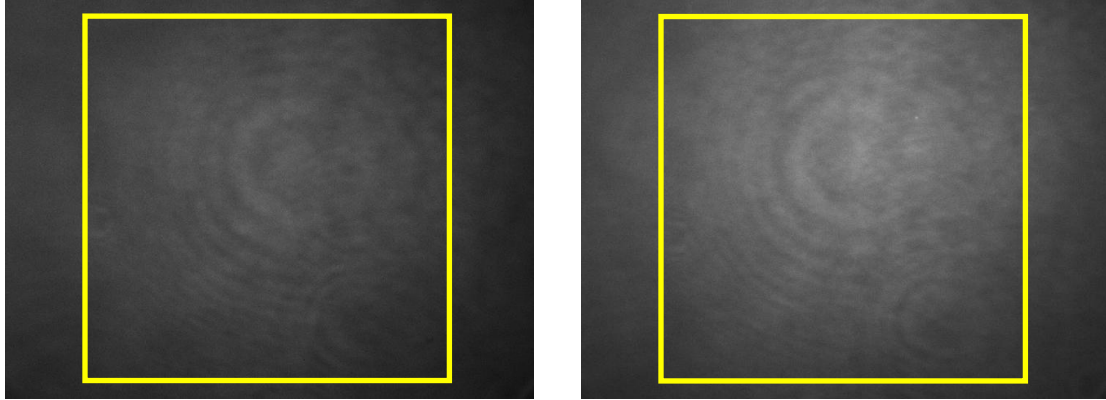


Figure 4.6. Representative 653×492 pixel ($160 \mu\text{m} \times 120 \mu\text{m}$) grayscale images (exp. 15 ms) from the EFT temperature calibrations of the emissions from FI excited by 514 nm light at $T = 20$ °C [left] and 60 °C [right] at $Re = 67$. The yellow square indicates the 450×450 pixel ($150 \mu\text{m} \times 150 \mu\text{m}$) region processed in these images.

Figure 4.6 shows representative images of the FI emissions excited by 514 nm light at $T = 20$ and 60 °C. Both images are mapped to the same grayscale map, and, as expected, the FI emission at 20 °C is weaker than that at 60 °C. The circular diffraction rings in the image, likely caused by aberrations in the imaging system and dust on the optics, are typically observed when using TIRF microscopes.

A sequence of 100 images was recorded at a framing rate of 19 Hz and an exposure of 15 ms at each T . A 450×450 pixels ($150 \mu\text{m} \times 150 \mu\text{m}$) region in the center of each image (yellow square in Fig. 4.6) was corrected for camera nonlinearities using Eq. 3-6, and the spatially and temporally averaged grayscale value corresponding to the average FI emission intensity, \bar{I} , and the standard deviation, $\sigma_{\bar{I}}$, were calculated over all 100 450×450 pixel images, or more than 2×10^7 samples. The uncertainty in the temperature

data was determined from $\sigma_{\bar{I}}$ using standard propagation of uncertainty analysis (Kline and McClintock, 1953). The average emission intensity, normalized by its value at 20 °C, \bar{I} / \bar{I}_{20} , is shown in Figure 4.3 as a function of the solution temperature T for 27 different temperatures between 20 °C and 60 °C. The error bars represent one standard deviation. A linear curve-fit to the data (solid line) with (adjusted) $\bar{R}^2 = 98.5\%$ gives the fluid temperature:

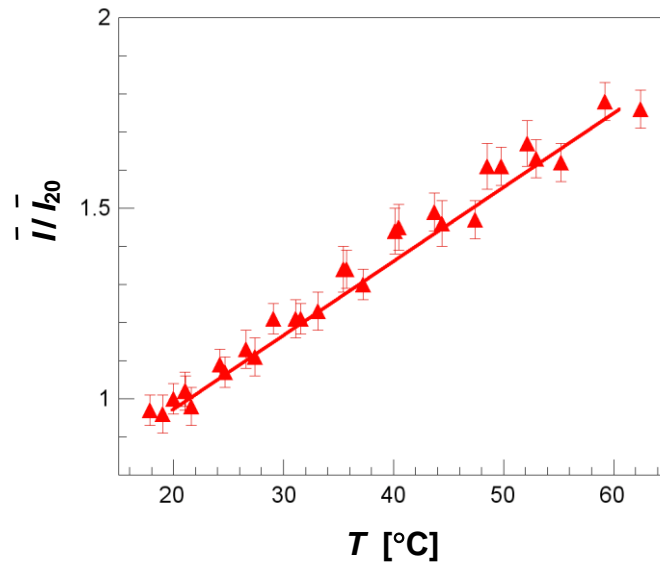


Figure 4.7. Plot of average normalized fluorescence intensity of the FI emissions for the EFT calibrations \bar{I} / \bar{I}_{20} as a function of solution temperature T . The overall change of the emission intensity was 1.8 % per °C. Equation 4-6 is given by the solid line, and the error bars represent the standard deviations.

$$T [\text{°C}] = 51.5 \bar{I} / \bar{I}_{20} - 30.1 \quad (4-6)$$

with a rms error of 1.8 °C. From this equation, the temperature sensitivity of FI illuminated by evanescent waves is 1.8% per °C, or lower than that for volume illumination in the literature (for example, Coppeta and Rogers, 1998), due perhaps to the nonuniform illumination.

4.3 EFT Results and Discussion

The liquid temperature fields over the first 320 nm next to the glass channel bottom were measured using EFT in steady Poiseuille flow through 1 mm square channels at $Re = 3.3$ and 8.3 (corresponding to volume flow rates $Q = 3.3 \mu\text{L/s}$ and $8.3 \mu\text{L/s}$, respectively). The next sections discuss the EFT results obtained in PDMS-glass and acrylic-glass channels.

4.3.1 Results for PDMS-Glass Channels

The Poiseuille flow of the FI solution in the channel was illuminated with evanescent waves. Two sequences of 100 images with physical dimensions of $120 \mu\text{m} \times 160 \mu\text{m}$ (492×653 pixels) at 16 Hz (exposure 20ms) were obtained by the EMCCD camera of the FI emissions within 320 nm of the glass surface (*cf.* section 3.2.1) at three different locations across the channel. The first reference sequence was obtained at the reference temperature $T_{\text{ref}} = 20.2 \text{ }^\circ\text{C}$.

Then, a temperature gradient was applied across the PDMS-glass channel by supplying 330 mW (3 V at 110 mA) to the ITO thin-film heater using a DC power supply (E3612A, Agilent Technologies) (Figure 4.5). In these experiments, the distance between the edge of the ITO heater and the side wall of the channel was 0.1 mm. The second sequence of images was acquired once the temperature field in this laminar and steady flow reached steady-state, which was taken in these experiments to be after the TC downstream of the imaged region (*cf.* Figure 4.5(a)) gave a temperature reading that varied by no more than $0.2 \text{ }^\circ\text{C}$ over 2 min.

Figure 4.8 shows the three different regions, A, B, and C, with physical dimensions of $120 \mu\text{m} \times 160 \mu\text{m}$, that were imaged next to the channel bottom. The edge of region A starts about $12 \mu\text{m}$ from the side wall of the channel next to the ITO heater. Region B in the center of the channel is 0.408 mm from region A. Finally, region C, which has an

edge about $12\ \mu\text{m}$ away from the opposite side wall, is $0.408\ \text{mm}$ from region B. The measured temperature gradients along the horizontal dashed line passing through the center of the three regions were used to determine the volumetric heat generation used in the numerical simulations (*cf.* section 4.4).

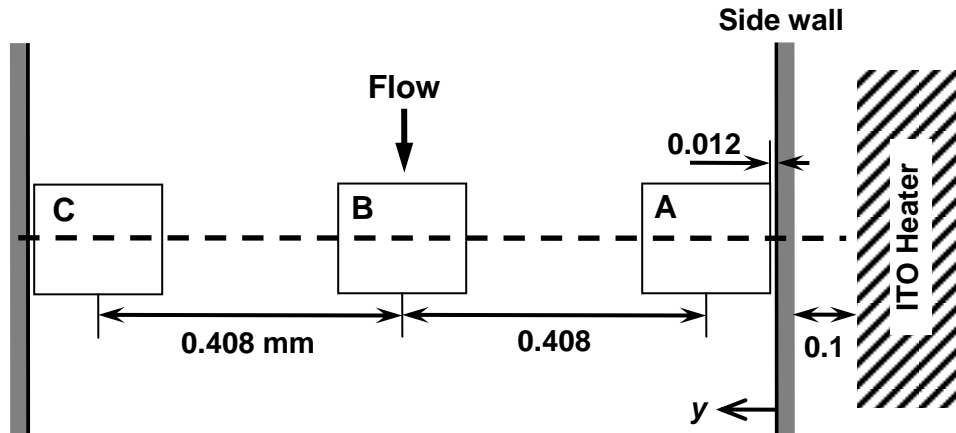


Figure 4.8. The three different regions, A, B, and C, imaged by the TIR microscope next to the bottom surface of the channel. The edge of region A is about $12\ \mu\text{m}$ from the channel wall near heater, while the edge of C is about $12\ \mu\text{m}$ from the opposite channel wall. Region B is in the center of the channel, and $0.408\ \text{mm}$ from regions A and C. The flow goes from top to bottom, as shown, and all dimensions are given in mm.

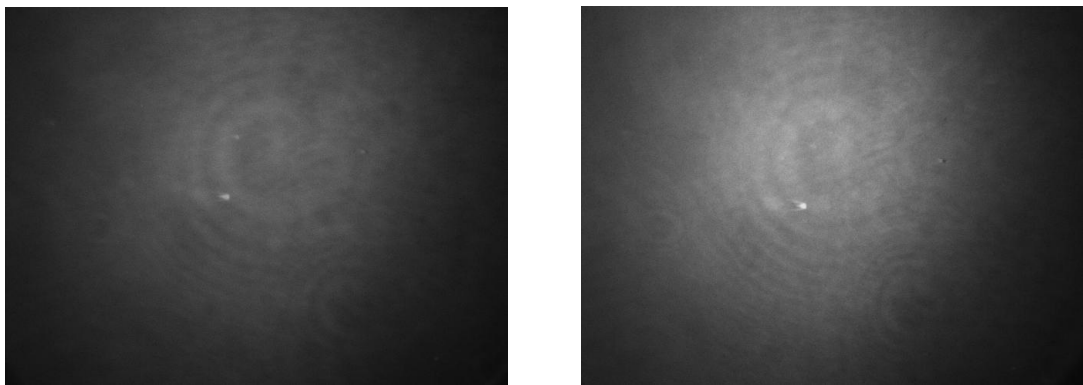


Figure 4.9. Average images of FI emissions excited by evanescent wave at $T_{\text{ref}} = 20.2\ \text{°C}$ [left] and with a temperature gradient imposed by supplying $330\ \text{mW}$ of electrical power to the ITO heater at $Re = 3.3$ [right]. Flow goes from top to bottom in the images.

The images were corrected for camera nonlinearities using Eq. (3-8), then averaged over all 100 images in the sequence. Figure 4.9 shows typical average images of the emissions from the 30 μM FI solution at $T_{\text{ref}} = 20.2$ $^{\circ}\text{C}$ and at $Re = 3.3$ with an applied temperature gradient from the ITO heater. The temperature field over the physical region imaged was then determined using Eq. (4-6) from the ratio of the average image with an applied temperature gradient to that obtained at T_{ref} .

Figure 4.10 and Figure 4.11 show pseudocolor temperature maps over regions (a) A, (b) B, and (c) C at a spatial resolution of 1 μm (*i.e.*, averaged over a 4 pixel square region) at $Re = 3.3$ and 8.3, respectively. As expected, the temperatures in region A nearest the heater are higher than those in regions B and C. At $Re = 3.3$ the majority of the data in A are at temperatures of 46–50 $^{\circ}\text{C}$, *vs.* 30–40 $^{\circ}\text{C}$ in B and C, and the temperatures decrease away from the heater. Similar characteristics are observed at $Re = 8.3$, although the actual temperatures are lower than those at the lower Re because of enhanced convection.

The uncertainty in the temperatures measured by EFT was determined from the standard deviation of the FI data using the method of Kline and McClintock (1953). The average uncertainties for regions A, B, and C varied from 1.02 $^{\circ}\text{C}$ to 1.16 $^{\circ}\text{C}$ and from 1.04 $^{\circ}\text{C}$ to 1.35 $^{\circ}\text{C}$ at $Re = 3.3$ and $Re = 8.3$, respectively, at a spatial resolution of 1 μm (4 pixels). As mentioned previously, the temperature gradient along the horizontal dashed line passing through the center of the three regions (and the heater) was compared with the values predicted by numerical simulations of this flow, and used to determine the volumetric heat generation input into the numerical simulations (*cf.* section 4.4).

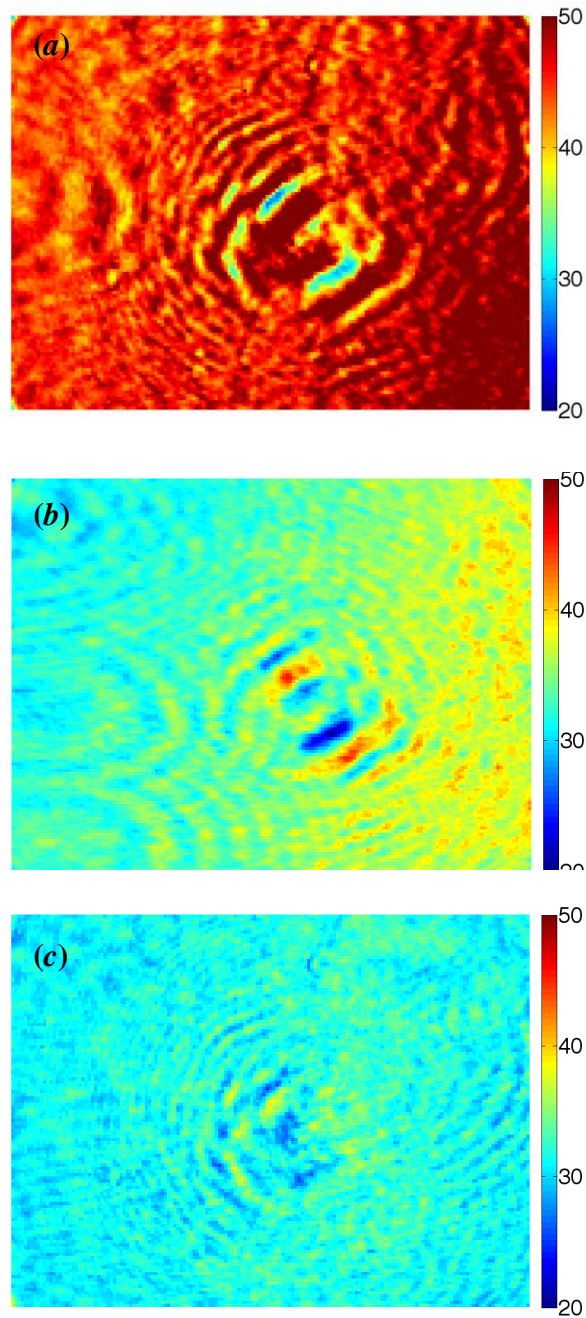


Figure 4.10. Pseudocolor temperature maps over regions (a) A, (b) B, and (c) C obtained in the PDMS-glass channel at $Re = 3.3$ at a spatial resolution of $1 \mu\text{m}$. The physical dimensions of all the regions are $120 \mu\text{m} \times 160 \mu\text{m}$.

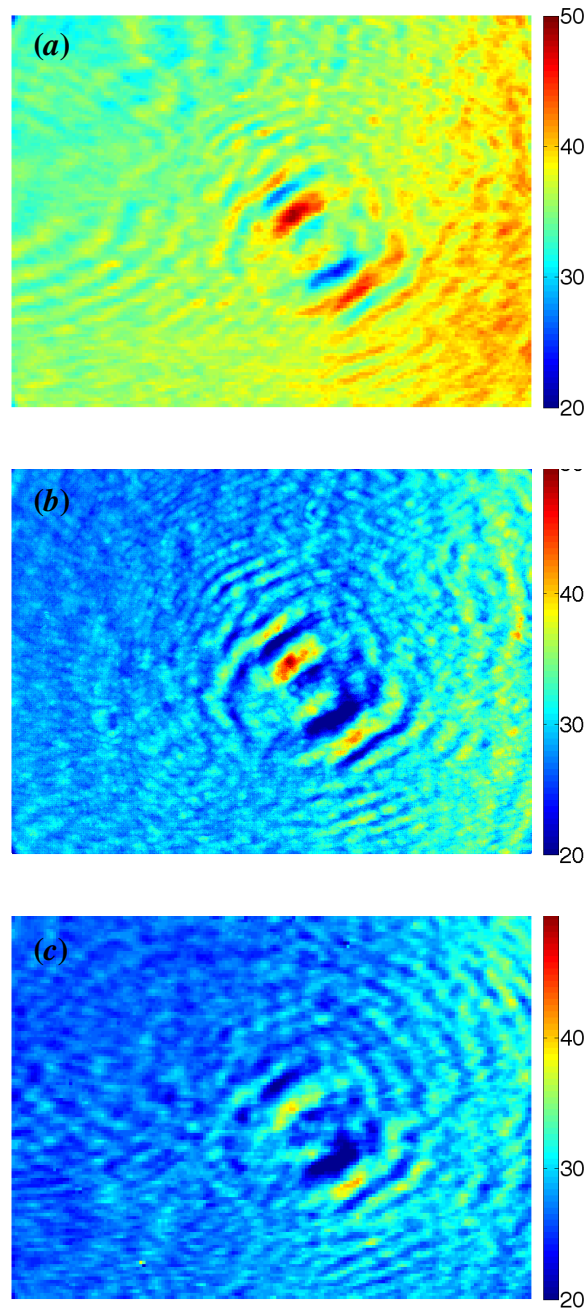


Figure 4.11. Similar to the previous Figure, but at $Re = 8.3$.

4.3.2 Acrylic-Glass Channels

A temperature gradient was applied across the acrylic-glass channels by supplying 300 mW (20 V at 15 mA) to the ITO thin-film heater. The input power to the heater was

chosen to be 10% lower than that used in the PDMS-glass channels because this level of heating gave a maximum fluid temperature of ~ 40 °C similar to that observed in the PDMS-glass cases. A 300 μm diameter hypodermic TC probe (HYP1-30-1/2-T-G-60-SMPW-M, Omega Engineering) was inserted into the tube attached to the exit port to monitor the temperature of the fluid as it exited the channel. The flow temperature field was defined to have reached steady-state once the temperature reading from the varied by no more than 0.2 °C over 2 min.

The emissions from a 30 μM FI solution flowing through the channel and illuminated by evanescent waves at 514 nm were again imaged over regions A, B and C and processed to estimate temperatures near the glass bottom wall as described previously. Figure 4.12 and Figure 4.13 show pseudocolor temperature maps for regions (a) A, (b) B, and (c) C at $Re = 3.3$ and 8.3, respectively. The circular arcs in the upper right and left corners of the images of regions A and B are due to the microscope settings, where a fraction of the fluorescence was monitored through the eyepieces (*vs.* being imaged by the EMCCD). This region of the image was not used to obtain temperature data. Although the actual temperature values are smaller at a given location than those observed in the PDMS-glass channel because less power is supplied to the ITO heater, the temperature fields are qualitatively similar to those measured in the PDMS-glass channels. The average uncertainties for regions A, B, and C varied from 0.89 °C to 1.07 °C and from 0.97 °C to 1.11 °C at $Re = 3.3$ and $Re = 8.3$, respectively, at a spatial resolution of 1 μm (4 pixels).

The EFT results over regions A, B, and C were compared with temperature predictions from numerical simulations of the flow through the heated PDMS-glass and acrylic-glass. Specifically, the temperature data along across the center of the regions were averaged over 40 pixels, corresponding to a spatial resolution of 10 μm , and compared with numerical predictions of wall and near-wall surface temperatures at a

spatial resolution of $50\ \mu\text{m}$. The next section details these numerical simulations.

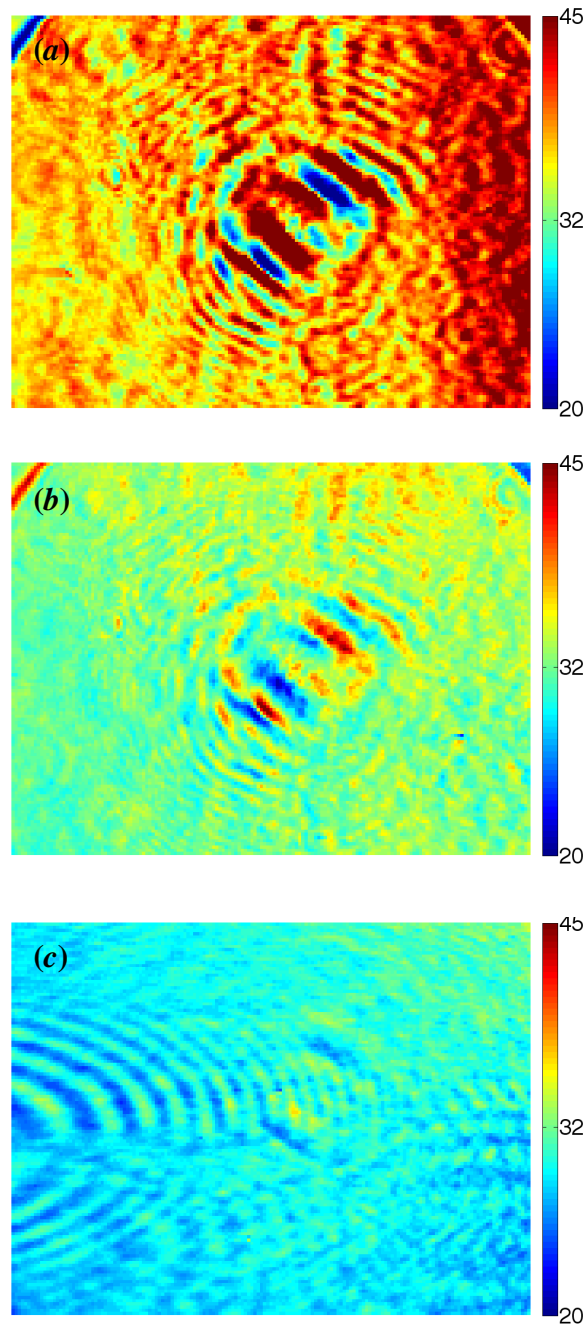


Figure 4.12. Pseudocolor temperature maps over $120\ \mu\text{m} \times 160\ \mu\text{m}$ region at $12\ \mu\text{m}$ apart from the wall near heater (a), at the center (b), and at $12\ \mu\text{m}$ apart from the wall opposite to the heater (c) at a spatial resolution of $1\ \mu\text{m}$ at $Re = 3.3$ in the acrylic-glass channel. The ring-like feature in the upper right and left corner in the image A and B is

because the window for the light path to the camera port is not fully opened.

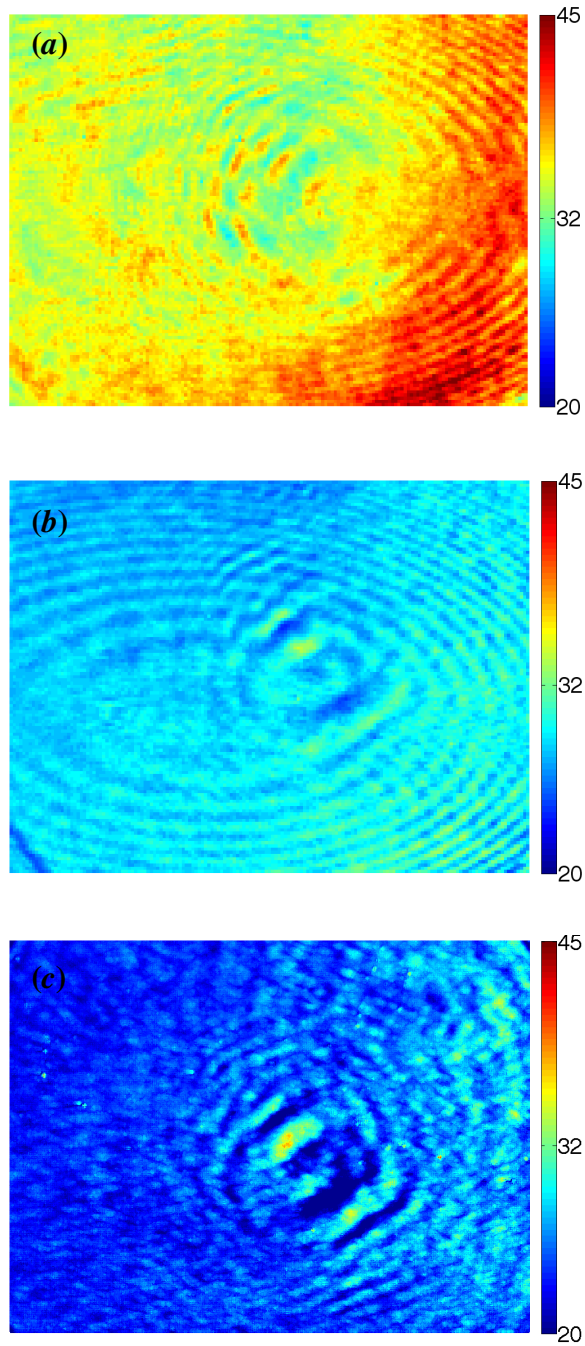


Figure 4.13. Similar to the previous Figure, but at $Re = 8.3$.

4.4 Numerical Simulation

This section describes the numerical simulations performed with the CFD software package FLUENT[®] v6.2 on a numerical model generated with Gambit v2.2.30 to validate the EFT and DFT results. Three-dimensional finite-volume simulations were carried out for numerical models of both the PDMS-glass and acrylic-glass channels used in the experiments.

4.4.1 PDMS-Glass Channels

4.4.1.1 Geometry and Grid Generation

Two different numerical models were constructed using Gambit. Both models included the 25 mm × 25 mm × 5 mm PDMS block containing the 1 mm × 1 mm square channel, and the 30 mm × 40 mm × 0.17 mm borosilicate glass substrate that forms the bottom wall of the channel including the 300 nm thick ITO heater on the glass, but the model shown in Figure 4.6(a) also included the steel microscope stage, while that shown in Figure 4.14 (b) excluded the stage. Initial simulation results showed that the temperature distribution inside of the channel was nearly identical for both models under otherwise identical conditions, with a temperature difference of less than 0.1 °C. This result suggests that very little of the heat output by the heater is transferred to the microscope stage, and that most of the power input to the heater is transferred to the working fluid, presumably because of the low thermal conductivities k of the channel materials, borosilicate glass and PDMS with $k = 1.14$ and 0.15 W/(m·K), respectively.

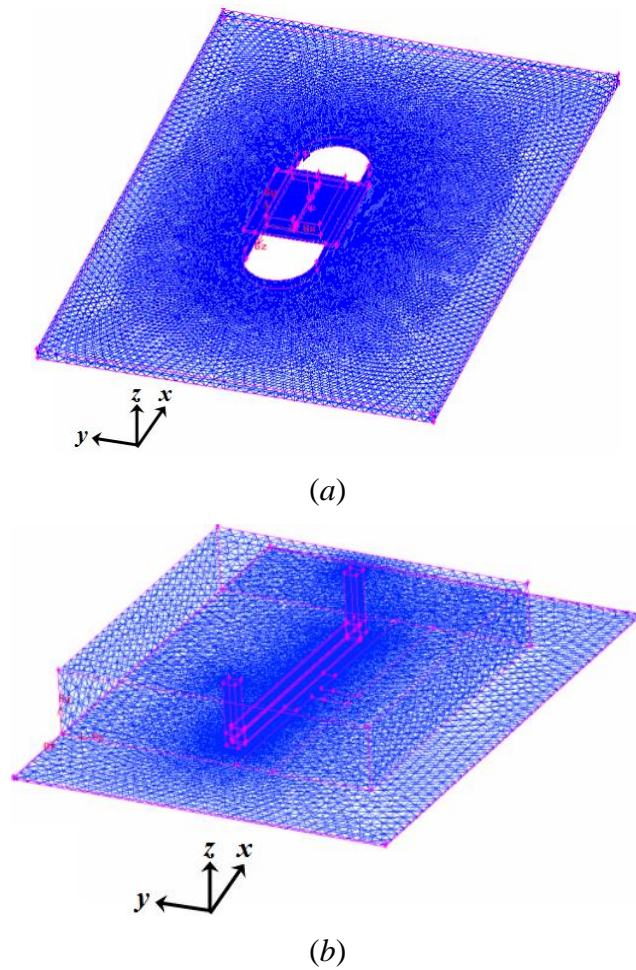


Figure 4.14. Numerical models meshed in Gambit 2.2.30 of (a) the PDMS block, glass substrate and microscope stage and (b) just the PDMS block and glass substrate. Note that the magnification of (b) is greater than that for (a).

Based on these results, further simulations were carried out on the smaller numerical model of only the PDMS block and the glass substrate to minimize computational times. As shown in Figure 4.15, the numerical model used includes the ITO heater and the Ti/Cu/Au conductive layers with an overall thickness of $5\ \mu\text{m}$ that transmit the current from the power supply to the actual heater. The dimensions of the numerical model, which are identical to the experimental test section, are given in Table 4.2.

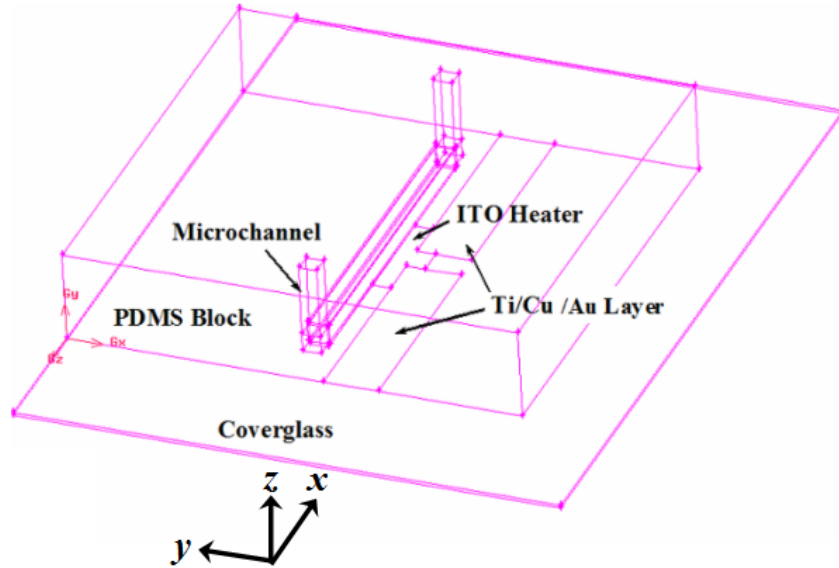


Figure 4.15. Detailed drawing of the numerical model consisting of the PDMS block and the glass substrate with the ITO heater and the Ti/Cu/Au conductive layer.

Table 4.2. Nominal dimensions of the numerical model. All dimensions are in mm.

Geometry	Dimension (L × W × H)
Borosilicate glass substrate	40 × 30 × 0.17
PDMS block	25 × 25 × 5
Channel - main	20 × 1 × 1
Channel - side	1 × 1 × 4
ITO heater	6 × 1 × ~0.0003
Ti/Cu/Au layer	8 × 3 × ~0.005

The tetrahedral mesh, built using Gambit[®], consists of 1.7×10^6 cells and 6.1×10^5 nodes. The grid is finest in the region of interest, namely the channel and the PDMS and glass surfaces near to the channel, with a resolution of 50 μm , and becomes coarser

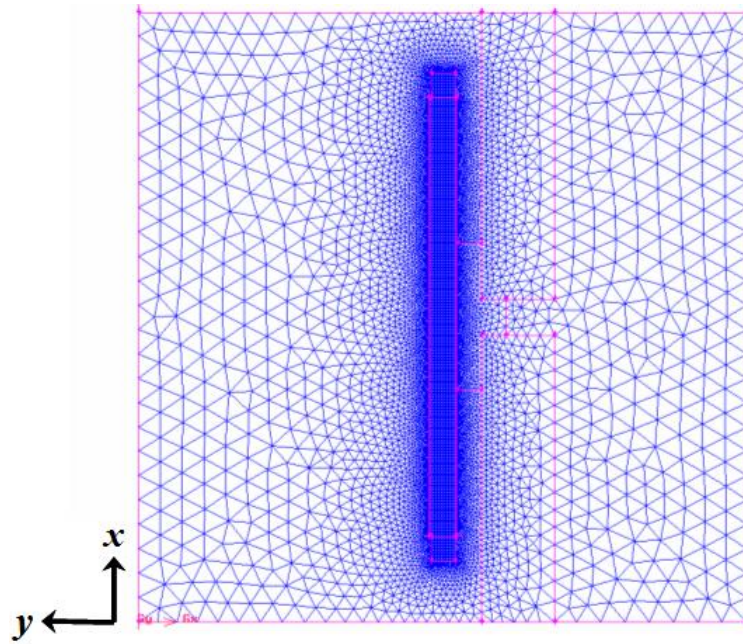
towards the outer boundaries of the PDMS block and glass substrate, where the spatial resolution gradually increases from 100 μm to 1 mm. Figure 4.16 (a), which shows a top view of the model, illustrates the variations in the mesh size along a cross-section.

Constructing a grid for the glass substrate was challenging, in part because of its high aspect ratio (width of 45 mm, vs. a thickness of 0.17 mm), and because this high aspect ratio resulted in highly skewed mesh elements, and hence diverging numerical solutions, near the edges at larger mesh sizes. The mesh for the glass substrate was therefore generated after meshing the channel and the PDMS block to minimize the number of skewed elements.

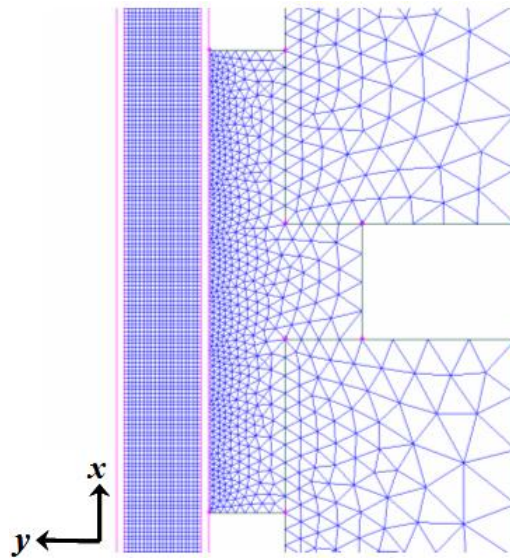
When modeling the ITO heater in Gambit, it is initially assumed that the heater is a planar (2D) surface. Since the 300 nm thickness of the heater is much less than the smallest mesh dimension of 50 μm , it was impractical given the limited computational resources available to generate a mesh that could transition between these two dimensions without divergence of the solution. A face mesh composed of tetrahedral elements was therefore generated over the entire surface of the heater. After importing the Gambit model into FLUENT, the ITO heater was modeled as a thin layer of material on the glass surface in FLUENT with a specified thickness of 300 nm. In the heat transfer calculations in FLUENT, the material type, the thickness, and the heat generation rates of the heater were specified as boundary conditions

Figure 4.16 (b) shows a magnified view of the channel, the ITO heater, and the Ti/Cu/Au conducting layer. Note that the mesh on the inside of the channel is hexagonal, while the remainder of the mesh is tetrahedral; the nodes within the channel are therefore evenly spaced 50 μm apart. Because the ITO heater and the Ti/Cu/Au conductive layer are very thin, with thicknesses of 300 nm and 5 μm , respectively, and these values are both much less than the thickness of the glass slide, the elements used to mesh these parts of the model were surface elements that were changed to volumetric elements by

imposing a finite thickness along a specific direction.



(a)



(b)

Figure 4.16. (a) A top view of the numerical model and (b) a magnified view of the central portion of the channel, the ITO heater, and the conducting layer. The flow direction is from top to bottom in both views.

4.4.1.2 Simulation

There were three major sets of inputs for the FLUENT simulations: the temperature of the fluid at the channel inlet T_{in} , the convective heat transfer coefficient h at the boundaries of the numerical model, and the volumetric heat generation rate \dot{q} of the ITO heater. The fluid temperature was measured by a TC 6 or 10 mm upstream of the imaged region in the experiments, and found to be 20.2 °C and 19.98 °C in the PDMS-glass and acrylic-glass channels, respectively. These measured temperatures were taken to be T_{in} in the simulations.

Standard free-convection boundary conditions from empirical correlations for external flows (*e.g.* Incropera and DeWitt 2002), were imposed on the surfaces exposed to ambient conditions. Such empirical correlations typically have an accuracy of 5–10% (Lloyd and Morgan, 1974 and Hatfield and Edwards, 1981, among others). As mentioned previously, the ambient temperature was measured by a TC during each experiment, and this temperature varied from 18 °C to 20 °C. Since this 2 °C variation in the room temperature had a negligible effect on h at the boundaries (less than 2% in all cases, or well below the typical accuracy of the empirical correlations for h) and the numerical predictions of fluid temperatures (less than 0.01 °C), all boundary surfaces were assumed to be at a constant and uniform temperature of 18 °C. At this temperature, the heat transfer coefficients were 6.69 W/(m²·K) over the bottom of the glass substrate, 7.6 W/(m²·K) over the top of the glass substrate, 4.22 W/(m²·K) over the top and bottom of the microscope stage, 4.14 W/(m²·K) over the sides of the microscope stage, 5.0 W/(m²·K) over the sides of the PDMS block, and 4.66 W/(m²·K) over the top of the PDMS block. These values were derived using the correlations detailed in the next few paragraphs.

The Churchill-Chu correlation for the average Nusselt number \overline{Nu}_L for free convection from a vertical wall based on the average surface temperature was used for

the sides of the PDMS block (and the microscope stage) at typical Rayleigh numbers $Ra_L = O(10^2)$ for the PDMS block and $Ra_L = O(10^7)$ for the microscope stage:

$$\overline{Nu}_L = 0.68 + \frac{0.67 Ra_L^{1/4}}{\left[1 + \left(\frac{0.492}{Pr} \right)^{9/16} \right]^{4/9}} \quad (4-7)$$

where Pr is the Prandtl number. An adiabatic boundary condition was imposed on the (vertical) side surfaces of the glass lid since the heat transfer through the 1 mm thick lid was, as verified by FLUENT simulations, negligible compared to that through the top and bottom surfaces of the lid.

For the upper surfaces of the glass lid, the PDMS block, and microscope corresponding to $Ra_L = O(10^5)$, $Ra_L = O(10^6)$, and $Ra_L = O(10^7)$, respectively, the standard power-law correlation for free convection from the upper surface of a heated horizontal plate was used:

$$\overline{Nu}_L = 0.54 Ra_L^{1/4} \quad (4-8).$$

Finally, for the bottom surface of the glass lid (*i.e.*, that contacting the microscope stage) and the microscope stage with $Ra_L = O(10^6)$ and $Ra_L = O(10^5)$, respectively, the correlation for a lower surface of a heated plate was used:

$$\overline{Nu}_L = 0.27 Ra_L^{1/4} \quad (4-9).$$

Because heat was generated over the entire volume of the ITO heater, a constant heat-generation rate boundary condition was imposed over the entire ITO layer except for the portion covered by the Ti/Cu/Au layers. In the experiments, some of the power supplied to the heater by the dc power supply will be dissipated in the solid portions of the channel such as the PDMS block or glass lid (*vs.* transferred to the fluid) and the surroundings. Given that the Cu conductive layer has a high thermal conductivity ($k \approx$

400 W/(m·K)) compared with glass or PDMS and a large surface area in contact with glass and PDMS surfaces, it is also likely that some of the heat from the heater will be transferred to the glass and PDMS through the Ti/Cu/Au layer.

Given that the actual power supplied to the ITO heater, and hence the volumetric heat generation rate for this heater, \dot{q} , are unknown, simulations were performed at different values of \dot{q} to estimate its value based on the EFT temperature data. It was assumed in these simulations that 80–100% of the electrical power is used by the ITO heater to heat the fluid (and the remainder is dissipated to the surroundings). The results from these simulations at different corresponding values of \dot{q} were compared with the experimental data, and the value of \dot{q} that best matched the EFT data was then taken to be the actual volumetric heat generation rate for the ITO heater.

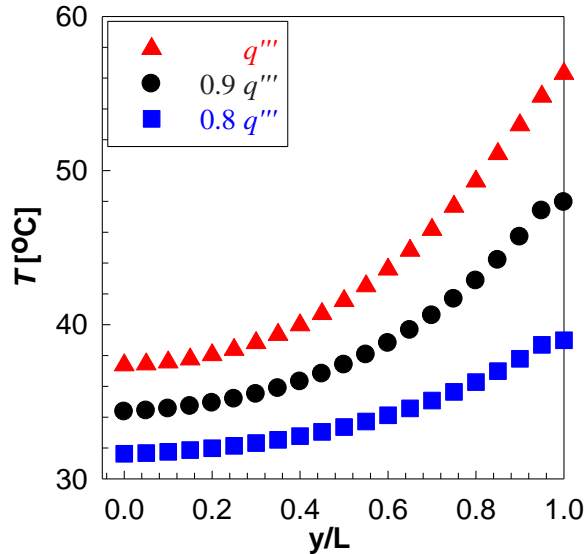


Figure 4.17. Wall surface temperature T as a function of normalized channel coordinate y/L predicted by FLUENT at different heat generation rates corresponding to 100% (*triangles*), 90% (*circles*), and 80% (*squares*) of the electric input power at $Re = 3.3$.

The volumetric heat generation rate was simply the ratio of the heater power (which was no more than the electrical input power of 330 mW) to the minimum nominal

volume of the heater of $3.24 \times 10^{-12} \text{ m}^3$. Figure 4.17 shows wall surface temperature profiles T (at $z = 0 \text{ }\mu\text{m}$) along the dashed line shown in the pseudocolor temperature map of Figure 4.8 as a function of the normalized coordinate across the channel y/L at three different values of \dot{q} corresponding to heater powers of 80%, 90% and 100% of the input electrical power. As expected, the temperatures increase as \dot{q} increases. The average differences in the wall surface temperature from the temperature profile for a heater power equal to the input electrical power at a given y/L were $1.9 \text{ }^\circ\text{C}$ and 4.8°C for the temperature profiles calculated for heater powers of 90% and 80% of the input power,.

In summary, the volumetric heat generation rate \dot{q} was the only input parameter that was “adjusted” in the numerical simulations to match the experimental data. The major source of error in the numerical predictions is likely due to errors in estimating the fraction of the input power transferred to the fluid.

In terms of the material properties used in the simulations, the properties of solids including glass, PDMS, Cu, and ITO heater at $25 \text{ }^\circ\text{C}$ were used and assumed to be constant in the simulation. Table 4.3 summarizes the other material properties used in the numerical simulations, which are derived from the literature. For the properties of water, the changes in density ρ and specific heat c_p were 0.5 and 0.1%, respectively, while thermal conductivity k and viscosity μ change up to +8.2% and -52.7%, respectively, for temperatures ranging from $20 \text{ }^\circ\text{C}$ to $60 \text{ }^\circ\text{C}$ (Incropera and DeWitt, 2002). Given their small changes over the temperature range of interest, the density and the specific heat were assumed to be constant ($\rho = 998.2 \text{ kg/m}^3$ and $c_p = 4182 \text{ J/(kg}\cdot\text{K)}$), in the simulations. The values for thermal conductivity and viscosity were assumed to vary with temperature, and were determined using the third-order polynomial curve-fit given in Eqs. 4-10 and Eq. 4-11 with $R^2 = 99.9\%$ to known values over a temperature range of $0\text{--}100 \text{ }^\circ\text{C}$ (Incropera and DeWitt, 2002). The predictions of Eqs. 4-10 and 4-11 for μ and k were in all cases

within 0.15 °C of the values given by FLUENT.

$$k = -2 \times 10^{-8} T^3 + 2 \times 10^{-5} T^2 - 0.0019 T + 0.3437 \text{ [W/(m}\cdot\text{K)]} \quad (4-10).$$

$$\mu = -2 \times 10^{-9} T^3 + 2 \times 10^{-6} T^2 - 0.0008 T + 0.0994 \text{ [N}\cdot\text{s/m}^2\text{]} \quad (4-11).$$

Table 4.3. Material properties at 25 °C used in the numerical simulations.

Material	ρ	k	c_p	Source
	[kg/m ³]	[W/(m·K)]	[J/(kg·°C)]	
Borosilicate glass	2230	1.14	750	Matsunami Glass Co.
Indium tin oxide (ITO)	7120	8.7	230	Indium Corporation
Polydimethyl siloxane (PDMS)	970	0.15	1460	Dow Corning®
Copper (Cu)	8940	401	0.38	Incropera and DeWitt (2002)

Figure 4.18 compares the wall surface temperatures at $z = 0 \text{ }\mu\text{m}$ (*cf.* Figure 4.5) predicted by FLUENT as a function of y/L at $Re = 3.3$ when (a) the properties of water were assumed to be constant (*i.e.*, independent of temperature) and those at a temperature of ?? °C and (b) the thermal conductivity k and viscosity μ of water varied with temperature (the other properties were assumed to be constant) under otherwise identical conditions. The Figure shows that having temperature-dependent values of k and μ in water reduces the maximum wall surface temperature by as much as ~3 °C; the average temperature difference ΔT across channel between two cases was 1.3 °C. These properties were therefore allowed to vary with temperature in the simulations shown in chapters 4 and 5.

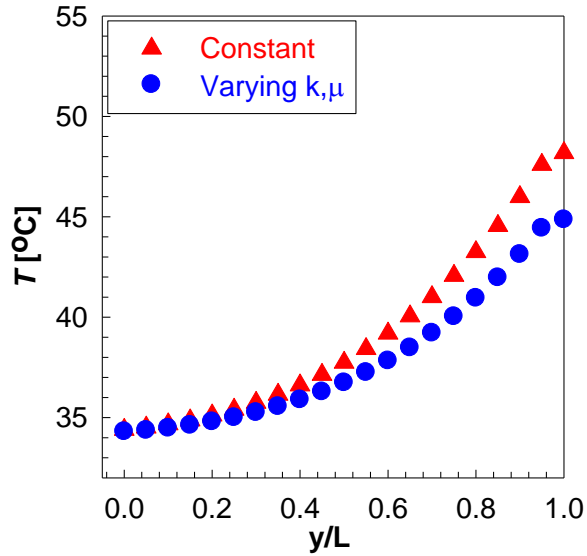


Figure 4.18. Wall temperature T as a function of normalized channel coordinate y/L in the numerical predictions at $Re = 3.3$ with constant properties of water (*triangles*) and with only varying k and μ (*circles*).

Simulations were carried out to determine how the calculated temperatures varied with the spatial resolution of the numerical grid for the PDMS-glass channel. Three different meshes, with spacings of 50 μm , 100 μm , and 200 μm , were generated in the region of interest near the channel; as described previously, the resolution gradually increased, becoming as large as 1 mm near the outer boundaries of the PDMS-glass channel. The average differences between the wall ($z = 0 \mu\text{m}$) and fluid ($z = 50 \mu\text{m}$) temperatures at $Re = 3.3$ and 8.3 compared with the values computed for the 50 μm mesh are shown in the Table 4.4. As expected, the average discrepancy decreases as the grid resolution decreases (*i.e.*, become finer). The average discrepancy between the temperatures computed on the 50 μm and 100 μm meshes is no more than 0.3 $^{\circ}\text{C}$, a value within the range of experimental uncertainty (at a spatial resolution of 10 μm) for EFT data. Given that the 50 μm mesh was the finest mesh possible within computational limitations (*i.e.*, the limitations on the RAM of the PC imposed by the operating system), the numerical simulations were performed on the 50 μm mesh..

Table 4.4. Average wall and fluid at $z = 0$ and $50 \mu\text{m}$, respectively) temperature discrepancies between the $50 \mu\text{m}$ mesh and the 100 or $200 \mu\text{m}$ spatial resolution meshes in the channel near the ITO heater.

Grid resolution [μm^3]	Average Discrepancy [$^{\circ}\text{C}$]			
	$Re = 3.3$		$Re = 8.3$	
	$z = 0 \mu\text{m}$	$z = 50 \mu\text{m}$	$z = 0 \mu\text{m}$	$z = 50 \mu\text{m}$
100	0.17	0.27	0.27	0.30
200	0.60	0.74	0.88	0.91

The numerical convergence of the temperature predictions was evaluated over a maximum of 10^4 iterations at several different locations in the numerical model such as the side wall of the channel near the heater, the bottom wall of the channel at the center, and within the inlet/outlet ports. In most cases, the temperatures at each location converged within about 100 iterations, and so the temperatures were assumed to achieve steady-state after a conservative number of $O(10^3)$ iterations.

4.4.1.3 Simulation Results: Temperature Profiles

Figure 4.19 shows the temperature distribution ranging from $18 \text{ }^{\circ}\text{C}$ to $112 \text{ }^{\circ}\text{C}$ (291K to 385K) over the entire numerical model at $Re = 3.33$ ($Q = 3.33 \mu\text{L/s}$) at a nominal \dot{q} corresponding to $1.83 \times 10^{11} \text{ W/m}^3$. As expected, the central region of the heater, which has a constant heat generation rate, has the highest temperature, $\sim 112 \text{ }^{\circ}\text{C}$, while the temperatures over the glass substrate away from the heater are at room temperature, or $18 \text{ }^{\circ}\text{C}$. Figure 4.20 shows a magnified view of the temperature field over the channel walls near the heater under the same conditions (note the different temperature scale). The bottom surface of the channel near the heater (and presumably

the fluid next to this surface) reaches a maximum temperature of about 56 °C, while the temperature over the top surface is a nearly constant 40 °C. Over a channel height of 1 mm, these simulations suggest that the maximum temperature gradient along the vertical exceeds 16 °C/mm.

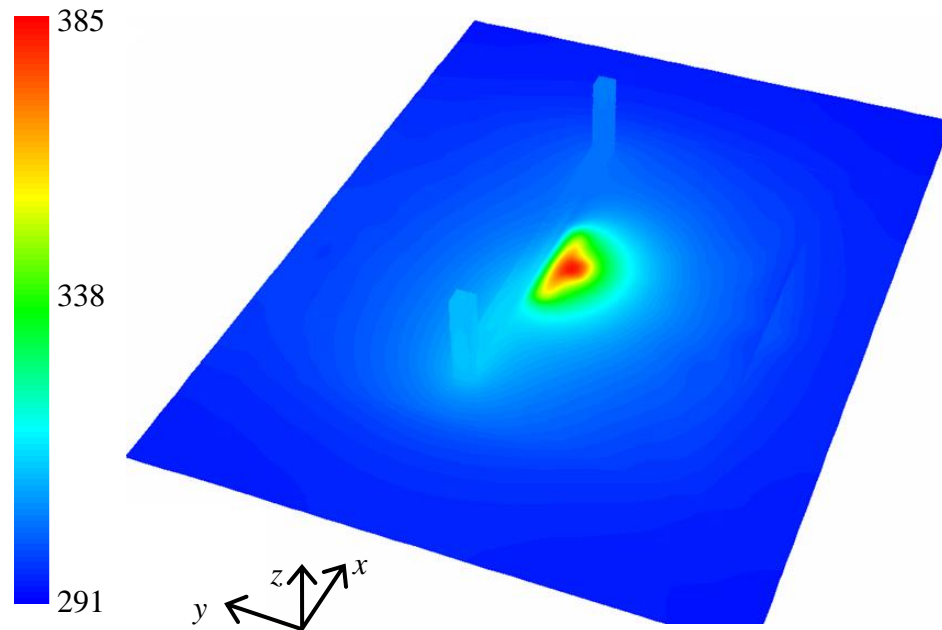


Figure 4.19. Pseudocolor temperature map of the channel, ITO heater, and the surface of the glass substrate at $Re = 3.33$ for the PDMS-glass channel. The highest temperatures are in the region near the heater, while the edges of the glass substrate remain at room temperature.

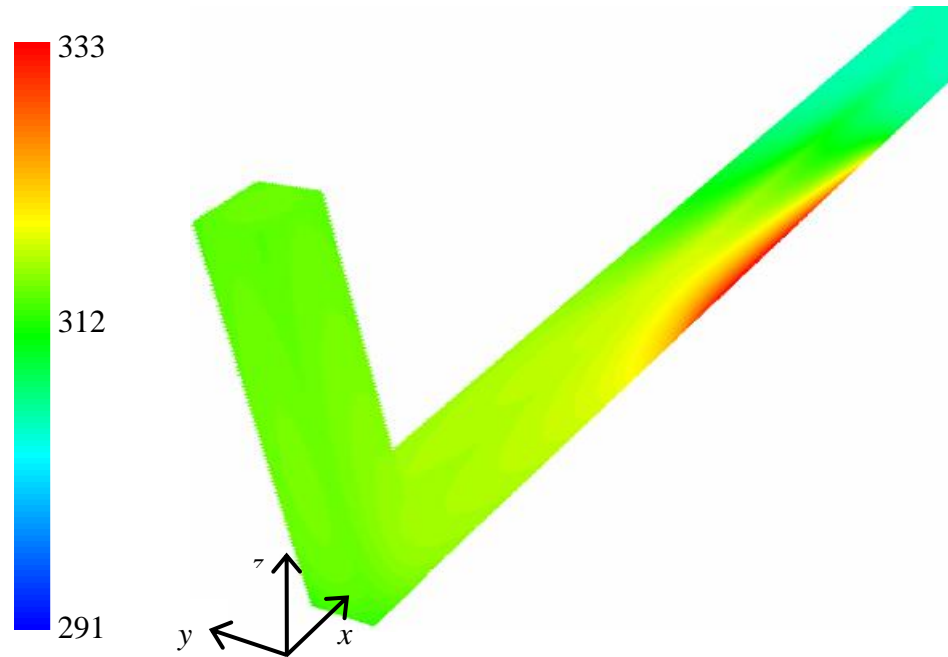


Figure 4.20. Temperature distribution on the channel walls near the ITO heater at $Re = 3.33$ in the PDMS-glass channel. The temperatures at the bottom and top surfaces of the channel are about 50 °C and 33 °C, respectively.

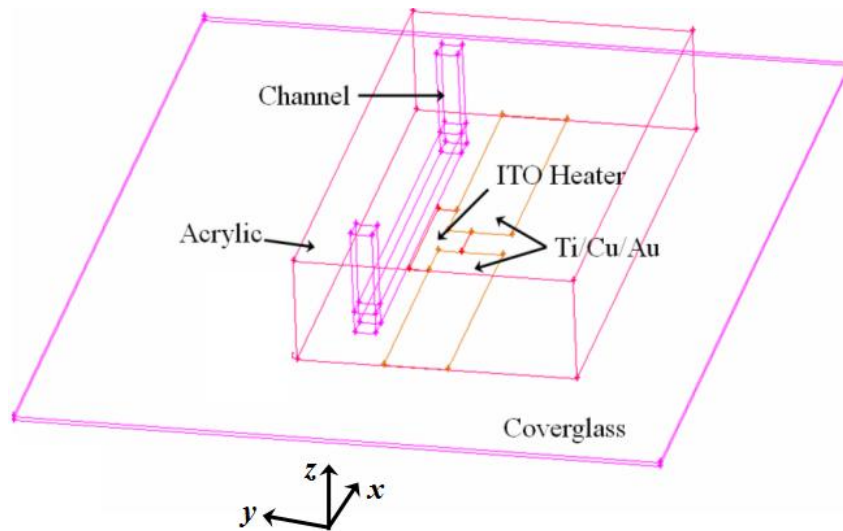


Figure 4.21. Detailed drawing of the numerical model of the acrylic-glass channel consisting of the acrylic block and the glass substrate with the ITO heater, the Ti/Cu/Au conductive layers, and the SiO_2 layer. In the view shown, the channel trench is 4 mm to the left of the center of the acrylic block.

4.4.2 Acrylic-Glass Channels

As shown in Figure 4.22, the numerical model of the acrylic-glass channels consists of the 13 mm × 25 mm × 5 mm acrylic block containing the 1 mm × 1 mm square channel and the 30 mm × 40 mm × 0.17 mm borosilicate glass substrate with a 300 nm thick ITO heater that forms the bottom wall of the channel. All the dimensions of this numerical model are identical to those for the PMDS-glass model except for the overall dimensions of the acrylic block.

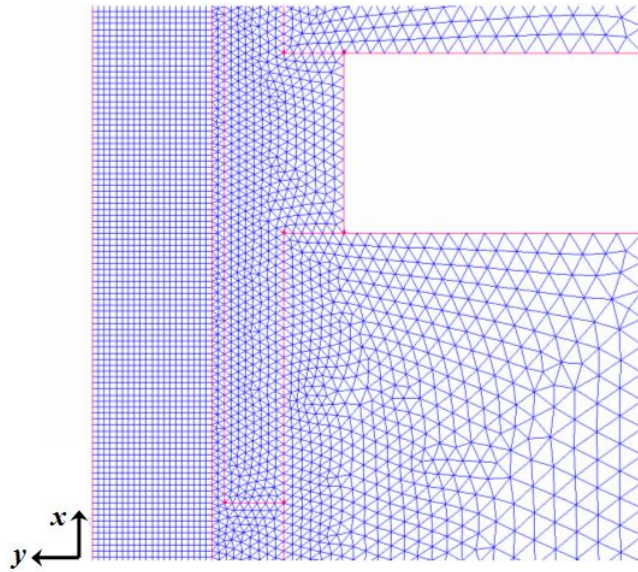


Figure 4.22. A magnified view of the central portion of the channel, the ITO heater and the conducting layer. The flow direction is from top to bottom in both views.

The tetrahedral mesh, built again using Gambit[®], consists of 2.3×10^6 cells and 6.2×10^5 nodes. As discussed in the previous section, the grid is finest in the channel, with a spatial resolution of 50 μm and becomes coarser towards the outer boundaries, where the spatial resolution is 1 mm (Figure 4.22). Similar to the PDMS-glass model, the mesh inside the channel consists of hexagonal elements, all 50 μm across, while the remainder of the mesh consists of tetrahedral elements of varying size.

The inputs to the simulations of the flow in the acrylic-glass channels are identical

to those detailed for the simulations of the PDMS-glass channels, specifically T_{in} , h at the boundaries of the numerical model, and \dot{q} of the ITO heater (for further details, *cf.* Sec. 4.4.1.2). The density and specific heat of acrylic were taken to be constant, and specifically the values at 25 °C: $\rho = 1400 \text{ kg/m}^3$ and $c_p = 1470 \text{ J/(kg}\cdot\text{K)}$ (source: Parsglass products Co.). As in the PDMS-glass channel models, all solid properties were assumed to be constant, while k and μ of water vary with temperatures. The solution again converged after about 100 iterations, so the temperatures were conservatively assumed to achieve steady-state after $O(10^3)$ iterations.

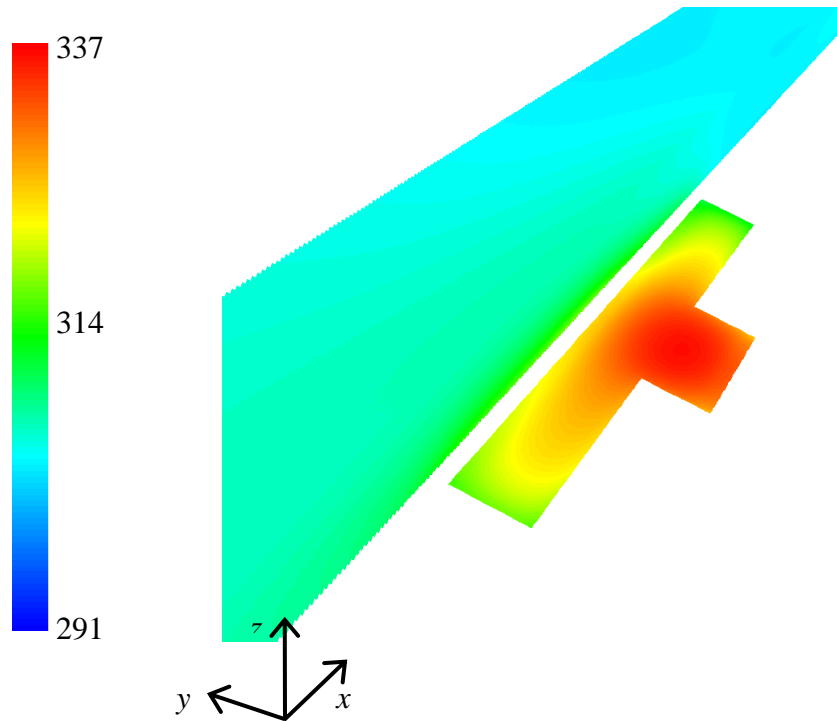


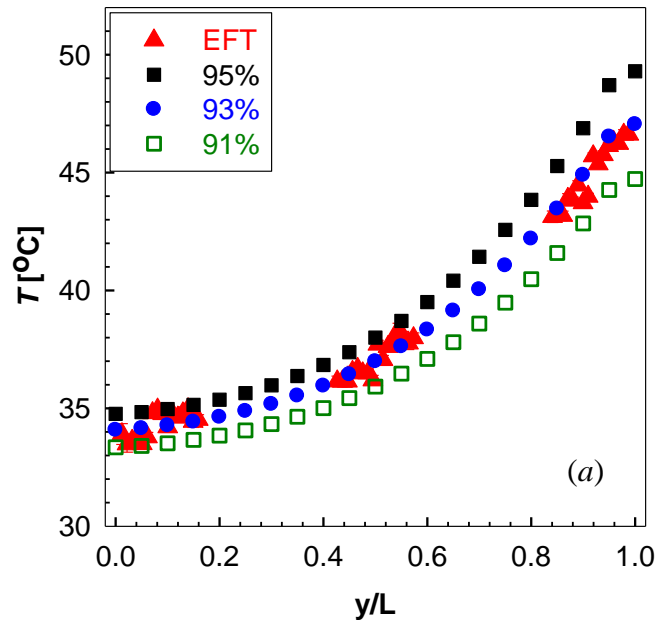
Figure 4.23. Temperature distribution over the channel wall near the ITO heater at $Re = 3.33$ in the acrylic-glass channel.

Figure 4.23 shows the temperature distribution over the channel walls in the section of the channel near the heater at $Re = 3.33$ in the acrylic-glass channel over a temperature range of 291K to 337K (18 °C to 64 °C). The bottom surface of the channel near the heater, and presumably the fluid next to this surface, reach a maximum temperature of about 44 °C, while the temperature over the top surface is nearly constant at about 34 °C.

These simulations suggest that the maximum temperature gradient along the vertical exceeds $10\text{ }^{\circ}\text{C}/\text{mm}$, a value less than that observed in the PDMS-glass channels in part because less power was supplied to the heater.

4.4.3 Comparison of EFT Results with Numerical Predictions

Figure 4.24 compares temperature profiles T along the dashed line shown in Figure 4.8 as a function of the normalized coordinate across the channel y/L obtained near the wall using EFT (*triangles*) at $Re = 3.3$ (*a*) and 8.3 (*b*) for the PDMS-glass channels. The EFT data, which are averaged over 40 pixels and hence have a spatial resolution of $10\text{ }\mu\text{m}$ in the plane of the image along y , are compared with wall surface temperatures ($z = 0\text{ }\mu\text{m}$) predicted by FLUENT at a spatial resolution of $50\text{ }\mu\text{m}$ at volumetric heat generation rates corresponding to 95% (*closed squares*), 93% (*circles*), and 91% (*open squares*) of the input electrical power. As expected, the numerically predicted temperatures decrease as \dot{q} decreases.



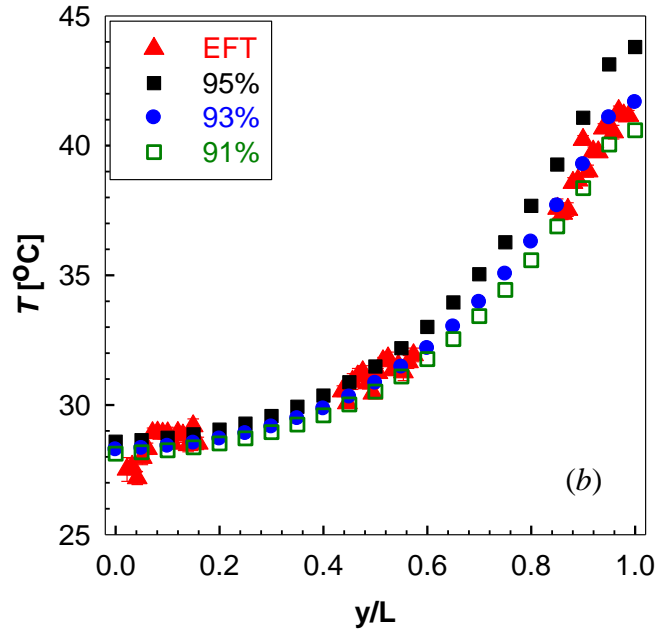


Figure 4.24. Temperature profiles T across the channel as a function of the normalized channel coordinate y/L measured by EFT (*triangles*) compared with FLUENT predictions at three different values of \dot{q} corresponding to 95% (*closed squares*), 93% (*circles*), and 91% (*open squares*) of the input electrical power. for $Re = 3.3$ (*a*) and 8.3 (*b*). The error bars on the EFT data, which are for the most part comparable to the size of the symbols, represent the experimental uncertainty.

The EFT data, which have a spatial resolution of about $0.3 \mu\text{m}$ along z (*i.e.*, normal to the image plane), have spatial fluctuations due to the diffraction patterns typically observed when using evanescent-wave illumination. The average uncertainties of the EFT results were 0.19 , 0.23 , and $0.23 \text{ }^\circ\text{C}$ in regions C, B, and A (corresponding to increasing y/L), respectively, at both Re . As expected, the steepest temperature gradients are near region A next to the ITO heater.

The effect of the diffraction patterns in the evanescent-wave illumination on the accuracy of the EFT results was evaluated by analyzing the ratio of calibration images obtained at two constant temperatures, specifically $T = 20 \text{ }^\circ\text{C}$ and $40 \text{ }^\circ\text{C}$. In theory, the only spatial variations in these calibration images should be due to spatial variations in

the illumination, including the diffraction patterns. As shown in Figure 4.25, the ratio of these two calibration images had a maximum deviation (at a spatial resolution of 40 pixels) of 3.8% from the mean value. Based on Eq. 4-6, the maximum offset of the temperature due to the diffraction patterns from the TC readings is then ± 1.1 °C.

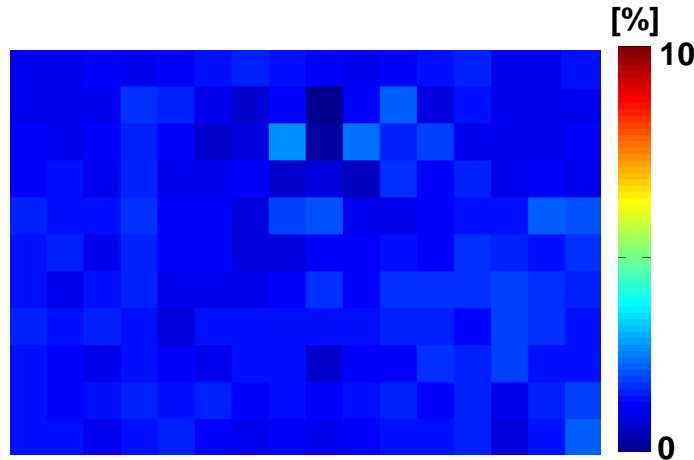


Figure 4.25. Pseudocolor map of ratio of two calibration images at 20 and 40 °C at a spatial resolution of 10 μm (40 pixels).

The largest fluctuations in the EFT data are observed in region C (*cf.* Figure 4.8), or in the region with the lowest fluid temperatures near the wall away from the heater. These variations are likely due to the relatively low level of FI emissions at these lower temperatures. A temperature variation of 0.5 °C corresponds to a variation of 0.009 in the I' , or 90 in grayscale value, where a typical grayscale value at a temperature of 20 °C is 10000 (*vs.* a maximum grayscale value of 65536). Since fluorescence intensity in the FI images increases with temperature, the fluid temperatures is quite sensitive to small variations in grayscale values due, for example, to noise or diffraction, at lower temperatures.

Given the difference in the spatial resolutions of the EFT data and FLUENT predictions, the EFT results were compared with results at the same y/L interpolated from a fifth order polynomial curve-fit with $R^2 = 99.9\%$ to the numerical predictions at of

the three different values of \dot{q} . The average discrepancies in regions A, B, and C (cf. Figure 4.8) at both Re are summarized in Table 4.5 .

Table 4.5. Average temperature discrepancies in regions A, B, and C (cf. Figure 4.8) between EFT data and the numerical predictions at values of \dot{q} .

Fraction of input electrical power transferred to the fluid [%]	Average Discrepancy [°C]					
	$Re = 3.3$			$Re = 8.3$		
	A	B	C	A	B	C
95	2.44	2.36	2.48	2.27	2.25	2.36
93	0.38	0.30	0.41	0.38	0.36	0.47
91	2.50	2.42	2.54	2.31	2.29	2.40

At both Re , the average discrepancy is minimized at a volumetric heat generation rate corresponding to 93% of the input electrical power, suggesting that approximately 7% of this power is dissipated to the surroundings, vs. transferred to the ITO heater. Based on this comparison, \dot{q} in the numerical simulations used to validate the EFT results in the PDMS-glass channels was taken to be 93% of the input electrical power divided by the nominal volume of the ITO heater of $1.8 \times 10^{-12} \text{ m}^3$, giving $\dot{q} = 1.83 \text{ W/m}^3$. In all cases, the average discrepancy is greatest in region C, presumably because this region has the greatest fluctuations in the EFT results. As seen in Figure 4.24a, the EFT results are in all cases bounded by the numerical predictions obtained at 91% and 95% of the input electrical power at $Re = 3.3$. At $Re = 8.3$, however, some of the EFT results in region C are beyond these bounds.

In this thesis, the experimental results from the DFT studies in PDMS-glass channels

were compared with FLUENT results where the heat generation rate at the ITO heater was adjusted to best match the EFT data because it was unclear how much of the input power is dissipated to the surroundings. As shown in Figure 4.24, the best match was obtained by assuming that 7% of the input electrical power was dissipated to the surroundings. We can also, however, directly estimate this dissipation, which is presumably loss due to Joule heating. To do so, the thermal resistances of the electrical wires connecting the DC power meter to the conductive layer and of the conductive layer itself were calculated. The overall thermal resistance of both components is then the sum of these individual resistances since the wires are in series with the conductive layer. For conductive layer, which is composed of Ti, Cu, and Au, the resistance of each layer:

$$R = \frac{t}{kA_s} \quad (4- 12)$$

where t is the thickness, k is the thermal conductivity, and A_s is the area of the layer. The dimensions for the Ti/Cu/Au layers is given in Table 4.2 and the values for the thermal conductivities of these three metals were those given by Incropera and DeWitt (2002). The net resistance of these three layers, which was the sum of the resistances of each layer, was 2 m Ω . This value is negligible compared with the resistance of the electrical wires of 1.4 Ω , which was measured using a multimeter (HHM93, Omega). For an, overall resistance of 1.402 Ω and an input current of 110 mA (*cf.* section 4.3.1), the estimated loss due to Joule heating was 16.9 mW, or 5.1% of the input electrical power of 330mW. This is 1.9% less than the value that gave the best match with the EFT results. This discrepancy may be due to: *i*) degradation of the ITO film over time, *ii*) imperfect adhesion between the conductive layers, *iii*) contact resistance between the conductive layer and ITO film and/or the electrical wire, and *iv*) variations in the thickness of the Ti, Cu and Au layers.

Table 4.6. Similar to Table 4.5, but for acrylic-glass channels.

Fraction of input electrical power transferred to the fluid [%]	Average Discrepancy [°C]					
	$Re = 3.3$			$Re = 8.3$		
	A	B	C	A	B	C
97.5	2.84	2.64	2.40	2.30	2.41	2.40
95.5	0.43	0.23	0.33	0.19	0.31	0.29
93.5	2.92	2.72	2.48	2.09	2.20	2.19

Figure 4.26, like Figure 4.24, compares the temperature profiles measured with EFT with those predicted by FLUENT, albeit for the acrylic-glass channels. The average uncertainties in the EFT data were 0.20 and 0.27 °C at $Re = 3.3$ and 8.3, respectively. Table 4.6, like Table 4.4, summarizes the average discrepancies over the three regions at $Re = 3.3$ and 8.3 for different values of \dot{q} . The trends observed for the acrylic-glass channel cases are qualitatively similar to those observed for the PDMS-glass channels, but the temperatures observed in the PDMS-glass channels are about 7 °C higher, and the average discrepancy is minimized at a volumetric heat generation rate corresponding to 95.5% of the input electrical power, suggesting that approximately 4.5% of this power is dissipated to the surroundings, vs. transferred to the ITO heater. Based on this comparison, \dot{q} for the FLUENT simulations used to validate the EFT data in the acrylic-glass channels was taken to be 95.5% of the input electrical power divided by the ITO heater volume, giving $\dot{q} = 1.67 \times 10^{11} \text{ W/m}^3$.

As shown in Figure 4.25, the best match to the EFT results in the acrylic-glass channels was obtained by assuming that 4.5% of the input electrical power was dissipated to the surroundings. This value was compared with an estimate of this dissipation due to

Joule heating following the procedures outlined earlier and assuming that the properties of the electrical wires and conductive layers are identical to those for the PDMS-glass channels. The result, 0.3 mW, is much less than 13.5 mW, or 4.5% of the total electrical input power of 300 mW. This large discrepancy may be due to degradation of the ITO heater and conductive layer, which were fabricated 6 months before the channel were fabricated.

Figure 4.27 shows a pseudocolor map of the wall surface temperature distribution (at $z = 0$) predicted by FLUENT at a spatial resolution of 50 μm at $\dot{q} = 1.83 \times 10^{11} \text{ W/m}^3$ over a 1 mm \times 0.75 mm region over the bottom (glass) wall of the PDMS-glass channel at $Re = 3.3$ (a) and 8.3 (b). Flow goes from top to bottom and the ITO heater is to the right of these images. As expected, the maximum temperatures are observed near the heater (at $Re = 3.3$ and 8.3 these maximum temperatures are about 47 $^{\circ}\text{C}$ and 41 $^{\circ}\text{C}$, respectively), and then gradually decrease moving away from the heater. The dotted line across image (a) denotes the location of the temperature profile shown in Figure 4.26. Figure 4.28 displays a similar surface temperature distribution over the bottom glass surface of the acrylic-glass channel at $Re = 3.3$ (a) and 8.3 (b). Again, the absolute temperatures observed in the acrylic-glass channels are lower than those in the PMDS-glass channels, but the trends observed in these channels are qualitatively similar to those observed in the PDMS-glass channels.

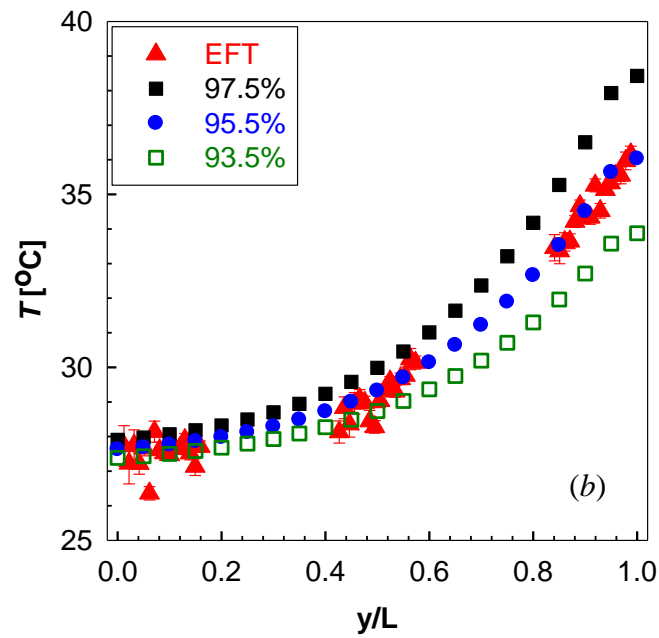
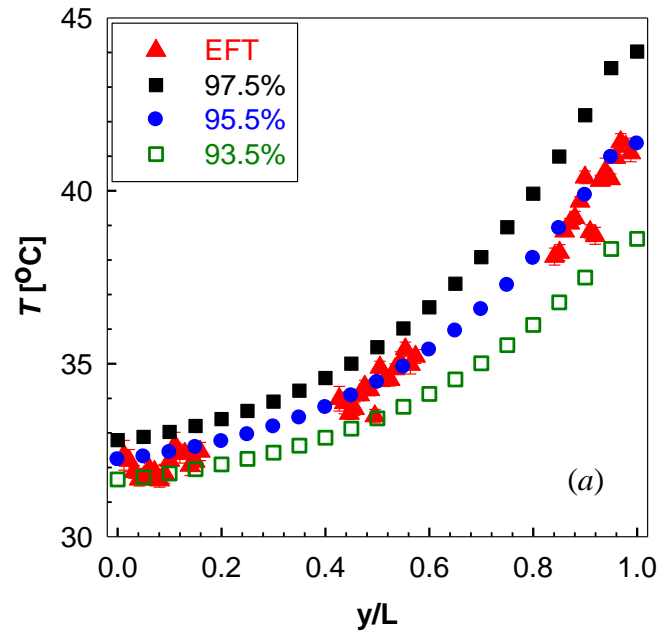


Figure 4.26. Similar to Figure 4.24, but in acrylic-glass channels at values of \dot{q} corresponding to 97.5% (filled squares), 95.5% (circles), and 93.5% (open squares) of the input electrical power.

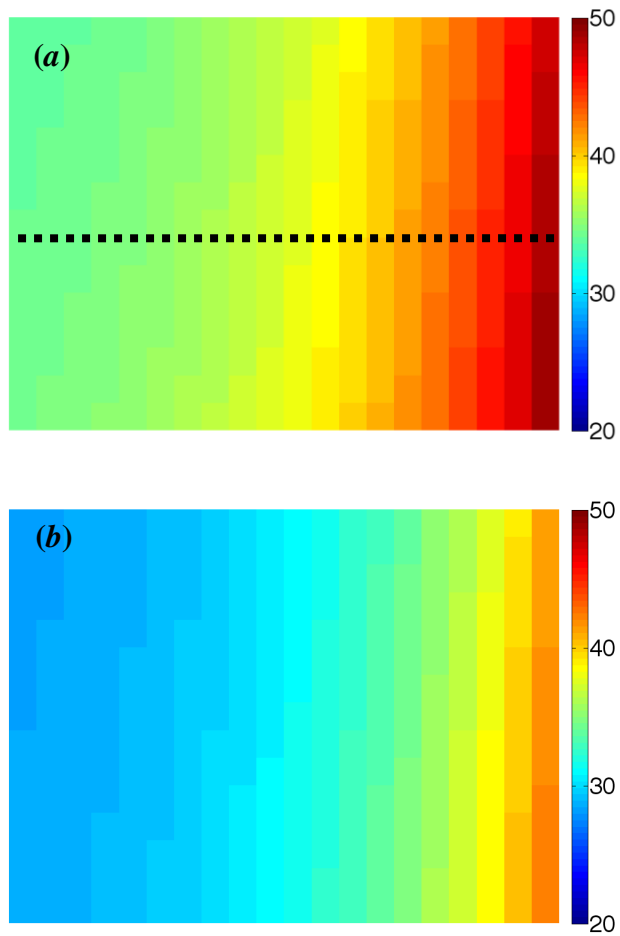


Figure 4.27. Pseudocolor map of wall surface temperatures (*i.e.* $z = 0$) from FLUENT at $0.93 q'''$ over $1 \text{ mm} \times 0.75 \text{ mm}$ region on the bottom surface of the PDMS-glass channel at $Re = 3.3$ (a) and 8.3 (b). Flow goes from top to bottom and the ITO heater is on the right. The dotted line across the image (a) in the center denotes the location of the temperature gradient compared to the EFT data in Figure 4.26.

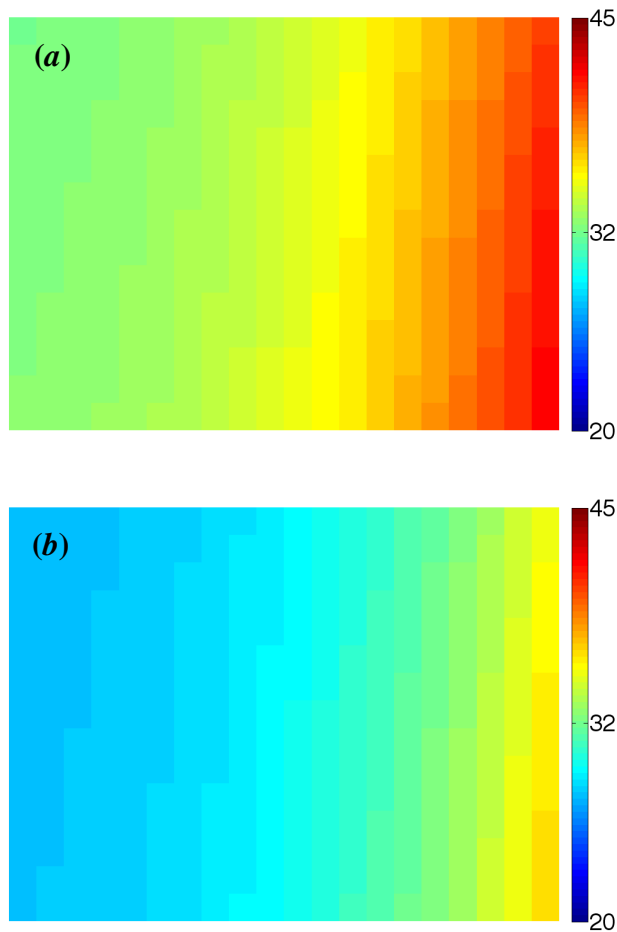


Figure 4.28. Similar to Figure 4.27, but with acrylic-glass channels at $0.935 q'''$.

4.5 Summary

The studies in this chapter describe the wall surface temperature thermometry technique in steady fully-developed Poiseuille flow at $Re = 3.3$ and 8.3 through 1 mm square channels using EFT. For that, a fluorescent dye solution Fl in DDI water was chosen as a temperature tracer and the temperature dependence of the emissions from Fl solution was determined to be 1.8% per $^{\circ}\text{C}$. The channel trenches were fabricated in PDMS and acrylic, then sealed by a 0.17 mm thick glass coverslip with a 300 nm thick ITO film heater. The fluid temperature distributions at three different locations on the bottom surface (averaged over first 300 nm next to the wall) across the channel were

measured with EFT. The experimental data shows that the EFT technique can map the temperatures with the maximum uncertainty of 0.27 °C at $Re = 8.3$ in both PDMS-glass and acrylic-glass channels.

Three-dimensional finite-volume simulations were performed using the CFD software package FLUENT[®] v6.2 and Gambit 2.2.30 to validate the EFT and DFT results. actual heat generation rate associated with the ITO heater in the Since some of the electrical input power is dissipated before it reaches the heater, the experiments \dot{q} was estimated by performing simulations at various values of volumetric heat generation rate, and taking \dot{q} to be the value that gave a numerical prediction of the temperature distribution across the channel at the center of the heater that gave the best match to the experimental data in terms of minimizing the average discrepancy between the experimentally measured and numerically predicted temperatures. The next chapter discusses the DFT experiments and results obtained under flow conditions identical to the EFT experiments on fluid temperatures in the bulk flow at different locations in the channel, specifically, along the optical axis, and compares these results to the FLUENT predictions.

CHAPTER 5

Dual-Tracer Fluorescence Thermometry

This chapter describes dual-tracer fluorescence thermometry (DFT) measurements. Section 5.1 summarizes the calibration studies of how the fluorescent emissions from Fl and SrB excited by volumetric illumination depend on solution temperature. Section 5.2 details of the temperature distributions obtained using DFT and compares them to the FLUENT[®] predictions with the volumetric heat generation rate determined from the EFT data. The section discusses the results for both the PDMS-glass and acrylic-glass channels. Section 5.3 summarizes the chapter.

5.1 Temperature Calibration for DFT Technique

This section describes the preparation of the Fl and SrB solution, and the calibration studies carried out to determine how the Fl and SrB emissions depend upon the solution temperature. The section concludes with a brief discussion of the calibration results and the experimental uncertainty in the DFT data.

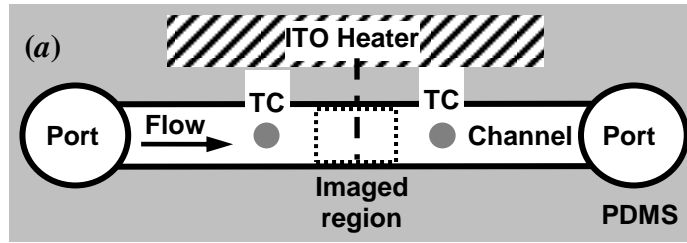
5.1.1 Preparation of the working fluid

For the DFT studies, an aqueous solution of two temperature-sensitive fluorophores, Fl and SrB, was prepared using procedures similar to those used to prepare the Fl solution for the EFT studies. As discussed previously, SrB had slight absorption onto PDMS and glass surfaces over a pH range from about 2 to 10, precluding its use as a temperature tracer for EFT. This small absorption had a negligible effect on the accuracy of FT when the fluorophores were excited by volume illumination, however. Given the improvement in accuracy of the temperature results from using a ratiometric approach discussed in Chapter 3, SrB was used as the second fluorophore in the DFT studies.

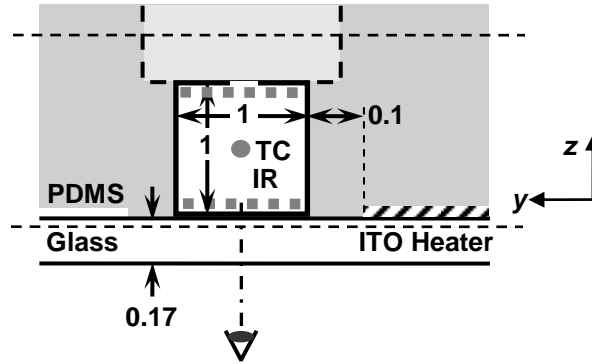
First, a stock solution consisting of 1 mmol/L Fl, 1 mmol/L SrB, and 100 mmol/L phosphate buffer was prepared using DDI water following the same procedures described in Section 4.2.1. The pH value of the stock solution was 8.5. This stock solution was then diluted with DDI water to prepare the working fluid at its final concentrations of 5 $\mu\text{mol/L}$ Fl and 5 $\mu\text{mol/L}$ SrB. The molar concentrations of the fluorophores were lower than that used in the EFT studies because of the higher excitation intensities used in the DFT studies. The pH value of the diluted solution was re-adjusted to 8.5 by adding appropriate amounts of the sodium phosphate dibasic dihydrate and sodium phosphate monobasic monohydrate salts. After thoroughly mixing the solution with a magnetic stirrer, the pH of the Fl-SrB-phosphate buffer solution was measured at solution temperatures $T = 20\text{--}60$ °C to ensure that the pH remained at 8.5 over this range of temperatures. Finally, the working fluid, after filtration as described in Sec. 4.2.1 to remove particulates and impurities, was degassed by placing the solution under a vacuum for at least 2 h.

5.1.2 Experimental Setup and Procedures

Figure 5.1 illustrates the heated PDMS-glass channels used for both the temperature calibration and the DFT measurements. The channels, fabricated as described in Section 4.2, were 1 mm square in cross-section and 20 mm in length, with the edge of the ITO heater edge 100 μm from the sidewall of the channel. Nearly all the experimental setup used in the DFT calibrations and studies was identical to that used in the EFT studies (*cf.* Chap. 4)—*i.e.*, the syringe pump, the temperature-controlled water bath, the copper heat exchanger, the two TCs, and tubing. The DFT setup differed from that used for the EFT studies, however, in two aspects: first, in terms of the illumination, and second, in terms of the imaging optics.



(a) Top view



(b) Cross-sectional View

Figure 5.1. Top (a) and cross-sectional (b) views of the channels with thin-film ITO heaters. The dotted rectangle in the top view and two thick dotted lines the cross-sectional view represent the imaged region (IR) by the microscope objective. The thick dashed line in (a) denotes the centerline of the heater. Two parallel thin dashed lines in (b) represent the vertical extent of the laser light sheet used to illuminate the entire channel. Flow goes from left to right in the top view, and out of the page in the side view, as indicated. All dimensions are given in mm.

Specifically, the channels were mounted on the stage of an inverted microscope (DM IL, Leica), and the entire channel was volumetrically illuminated by a light sheet at $\lambda = 514 \text{ nm}$ formed from an air-cooled argon-ion laser (543-MA-A03, Melles Griot) beam passing through an excitation filter (z514/10x, Chroma Tech) (two dashed lines in Figure 5.1b) which was directly incident on the side of the channel opposite the ITO heater. The output power of the 514 nm laser beam was 60 mW, as measured by a laser power meter (Lasermate Q, Coherent), and varied by no more than 0.02% over 8 h. The FI fluorescent emissions were isolated by a bandpass filter (NT48-083, Edmund Optics)

that passed light at $\lambda = 529\text{--}555$ nm while rejecting the 514 nm illumination. The SrB emissions were isolated by a longpass filter (NT47-618, Edmund Optics) that only passed light at $\lambda \geq 600$ nm while reflecting the 514 nm illumination. The fluorescence was imaged by a $10\times/\text{NA } 0.25$ microscope objective (506084, N Plan, Leica) through a $0.5\times$ camera adaptor onto the same electron multiplying CCD (EMCCD) camera (Cascade 650, Photometrics) used in the EFT studies, and recorded as 16-bit 653×492 pixel images on a PC HD.

5.1.3 DFT Calibration Results

To calibrate the DFT technique, the temperature response of the FI-SrB solution at temperatures $T = 20$ °C to 60 °C was measured in the same PDMS-glass channel with the same optical system as those used in the DFT experiments. The temperature of the working fluid in the channel was kept at a constant value by passing the fluid through a copper-coil heat exchanger consisting of 15 m of 1.5 mm ID copper tubing immersed in a constant-temperature circulating water bath before entering the channel. The Reynolds number for the laminar Poiseuille flow Re based on the channel cross-sectional dimension of 1 mm and average speed was 67, corresponding to a volume flow rate $Q = 0.067$ mL/s, to minimize thermal losses. Since no power was supplied to the heater during these calibrations, the fluid temperature T was determined by the set point temperature of the water bath. Data were acquired at least 20 min after flow startup when the TC readings were within 0.2 °C (*i.e.*, the measurement accuracy of the TC) of the set point temperature of the water bath.

A sequence of 100 images spanning 5.7 s of the emissions from FI and SrB was recorded at a framing rate of 16.2 Hz and an exposure of 20 ms. Both sequences were recorded within a few seconds of each other by switching between the appropriate filters which were next to each other in a translating filter holder. The depth of field of the

objective was about 14 μm . The magnification of the imaging system, determined from a scale with 20 μm divisions, was measured to be 5.06, corresponding to 1.46 $\mu\text{m}/\text{pixel}$ for the 7.4 μm CCD pixels as explained in chapter 3. The physical dimensions of the 653 \times 492 pixel images were therefore 954 $\mu\text{m} \times$ 718 μm .

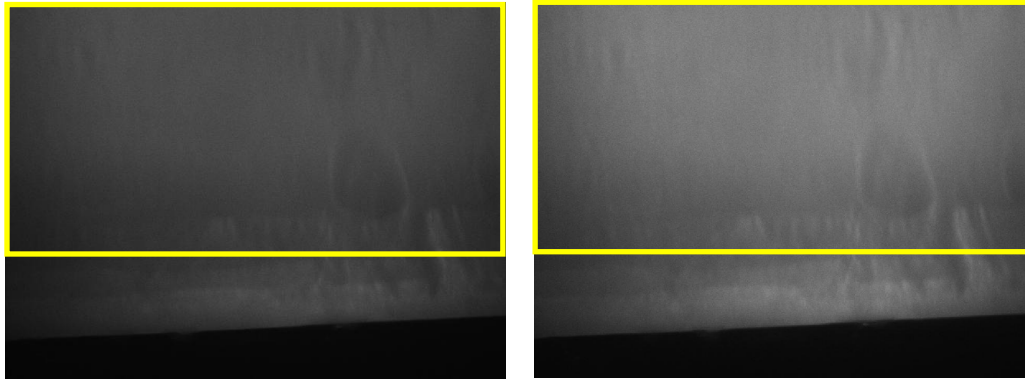


Figure 5.2. Typical 653 \times 492 pixel (954 $\mu\text{m} \times$ 718 μm) grayscale images at an exposure of 20 ms of Fl [left] and SrB [right] at $T = 20\text{ }^\circ\text{C}$ from the temperature calibrations. Note that these images, obtained within a few s of each other, are of the same solution imaged through different filters. The rectangle indicates the 650 \times 300 pixel (950 $\mu\text{m} \times$ 440 μm) region processed in these images. The black region on the bottom of the images is the sidewall of the channel.

Figure 5.2 shows representative images of the Fl and SrB emissions at a solution temperature $T = 20\text{ }^\circ\text{C}$. Both images are mapped to the same grayscale map, and, as expected, the Fl emission is weaker than that of SrB when excited at 514 nm. A 650 \times 300 pixel (950 $\mu\text{m} \times$ 440 μm) portion of the image (denoted by the rectangle in the Figure) in the center of the channel was used to determine the grayscale values corresponding to a given solution temperature. As described previously, two sequences, each consisting of 100 of these 650 \times 300 pixel regions, were corrected for camera nonlinearities using Eq. (3-6), then temporally and spatially averaged over all 19.5×10^6 pixels to obtain an average grayscale value, or intensity, \bar{I} .

Figure 5.3 shows \bar{I} , normalized by that at 20 $^\circ\text{C}$, \bar{I}_{20} , as a function of solution

temperature T measured by the TCs at $T = 20\text{ }^{\circ}\text{C}$ to $60\text{ }^{\circ}\text{C}$ for Fl (red triangles) and SrB (blue circles). The error bars denote the standard deviation of the data. The fluorescence from Fl and SrB increase by about 2.41 % and decrease by about -1.51% , respectively, as the solution temperature increases from $T = 20\text{ }^{\circ}\text{C}$ to $60\text{ }^{\circ}\text{C}$. These values are in good agreement with the temperature sensitivities of 2.43 % per $^{\circ}\text{C}$ and -1.55% per $^{\circ}\text{C}$ reported by Coppeta and Rogers (1998) for Fl and SrB, respectively, although Figure 5.3 suggests that the emission intensities do not vary linearly with T . These calibration results for Fl and SrB were consistent over multiple independent experiments.

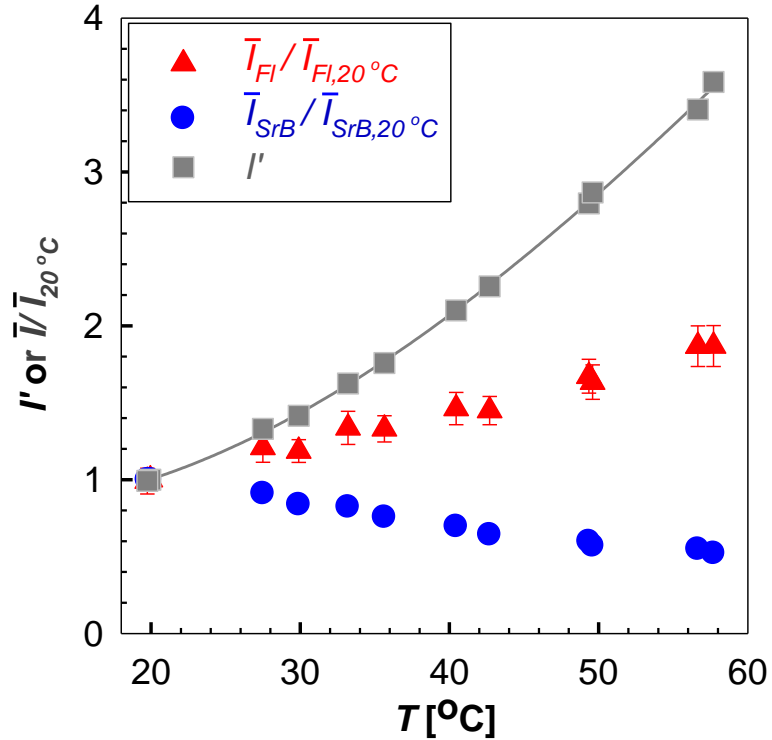


Figure 5.3 Average normalized fluorescence intensity \bar{I} / \bar{I}_{20} as a function of solution temperature T for Fl (triangles) and SrB (circles). The ratio of these two normalized intensities I' (squares) is also given as a function of T , along with a fifth-order polynomial curve-fit to these data (solid line), given by Eq. (5-1).

The ratio of these two normalized signals, I' (grey squares), clearly has much greater variation with temperature than either the normalized Fl or SrB emissions,

increasing from 1 at $T = 20$ °C to about 3.6 at $T = 60$ °C. A fifth-order polynomial curve-fit ($\bar{R}^2 = 99.7\%$, RMSE = 0.06%) to I' (solid line, Figure 5.3) gave:

$$I' = -[1.64 \times 10^{-7} (\text{°C})^{-5}]T^5 - [3.21 \times 10^{-5} (\text{°C})^{-4}]T^4 + [2.41 \times 10^{-3} (\text{°C})^{-3}]T^3 - [8.49 \times 10^{-2} (\text{°C})^{-2}]T^2 + [1.44 (\text{°C})^{-1}]T - 8.52 \quad (5-1)$$

where the temperature T is measured in °C. Differentiation of Eq. (5-1) gives temperature sensitivities dI' / dT ranging from 4.0% per °C at $T = 20$ °C to 12 % per °C at $T = 60$ °C, suggesting that this technique has greater sensitivity at higher temperatures. These values are significantly higher than the -2.7% per °C reported by Natrajan and Christensen (2009) in their microscale DFT studies. A fifth-order polynomial curve-fit ($\bar{R}^2 = 99.6\%$, RMSE = 0.6 °C) to the inverse relation, namely the temperature as a function of I' , gave:

$$T = -(47.83 \text{°C})(I')^5 + (250.8 \text{°C})(I')^4 - (476 \text{°C})(I')^3 + (384.7 \text{°C})(I')^2 - (85.41 \text{°C})I' + (14.64 \text{°C}) \quad (5-2)$$

Eq. (5-2) was used to determine liquid-phase temperatures for the results presented in Section 5.4.

The absorption and emission spectra shown in chapter 3 suggest that there may be some “cross-talk” between the Fl and SrB emissions, and that a small amount of the Fl emissions may be imaged through the longpass ($\lambda \geq 600$ nm) filter. Moreover, the emission band of Fl and the absorption band of the SrB have some overlap, suggesting that some of the emissions from Fl may excite the SrB, resulting in “spectral conflict.” Both of these phenomena are often issues for DFT with a single illumination source.

To evaluate the effects of cross-talk and spectral conflict, three 100-image sequences were acquired of the flow of three different solutions at $T = 55$ °C: 1) the working fluid described previously; 2) a 5 $\mu\text{mol/L}$ Fl and 0.1 mol/L phosphate solution with no SrB; and 3) a 5 $\mu\text{mol/L}$ SrB and 0.1 mol/L phosphate solution with no Fl. The

temperature of 55 °C, near the upper end of the temperature range studied here, was chosen to maximize cross-talk and spectral conflict, since the Fl emissions will be stronger, and the SrB emissions weaker, at higher T . All three sequences were acquired in the same setup used for the DFT calibrations under identical experimental conditions within a single experimental run over ~90 min by switching the syringes in the syringe pump. In all cases, the emission intensities recorded for the three solutions through the appropriate filters were identical within the standard deviations of the images, suggesting that both cross-talk and spectral conflict are negligible. These results are in agreement with those reported by Shafii *et al.* (2009) who reported that the effects of cross-talk and spectral conflict were negligible for their 0.5 $\mu\text{mol/L}$ Fl and 0.5 $\mu\text{mol/L}$ SrB solutions over optical pathlengths exceeding 1 cm.

5.2 DFT Results and Discussion

5.2.1 DFT Results in PDMS-Glass Channels

The PDMS-glass and acrylic-glass channels used for the EFT studies were also used in the DFT experiments to measure bulk fluid temperatures across the channel at different heights in the channel z . This section details the experimental results with PDMS-glass channels using DFT. As in the EFT studies, fluid temperature fields were measured in the steady Poiseuille flow of the working fluid through a 1 mm square channel at $Re = 3.3$ and 8.3. A temperature gradient was created across the channel by heating the channel on one side with the ITO heater; 330 mW and 300 mW of electrical power were supplied to the PDMS-glass and the acrylic-glass channels, respectively.

The fluorophore solution was volumetrically illuminated through the side wall of the channel (*cf.* Figure 5.1*b*) at $\lambda = 514$ nm. The emissions from the Fl and SrB were isolated using the appropriate filters and recorded as sequences of 100 653×492 pixel ($953 \mu\text{m} \times 718 \mu\text{m}$) images at 16.2 Hz (exposure 20 ms) by the EMCCD camera. By

vertically translating the microscope objective, images were recorded with the focal plane of the image near the bottom (glass) wall of the channel, and near the top (PDMS) wall of the channel. The z -location of the center of the focal plane for the images near the bottom wall of the channel (where z was measured from and normal to the glass bottom wall of the channel) was estimated to be at $z = 14 \mu\text{m}$, based on the depth of field of the objective. That of the images near the top wall of the channel were estimated to be at $z = 950 \mu\text{m}$, based on calibrations of the knob used to vertically translate the microscope objective. The images were corrected for camera nonlinearities, again using Eq. (3-6), and temporally averaged over all 100 images. Figure 5.4 shows typical average grayscale images of the FI and the SrB emissions in the heated channel. The black region on the right of the images is the sidewall of the channel. The FI emissions are somewhat weaker than those of SrB: the maximum grayscale values in these FI and SrB images are 14885 and 21119 (out of a maximum possible grayscale of ~ 53000) respectively, while the average grayscale values are 10301 and 13987, respectively.

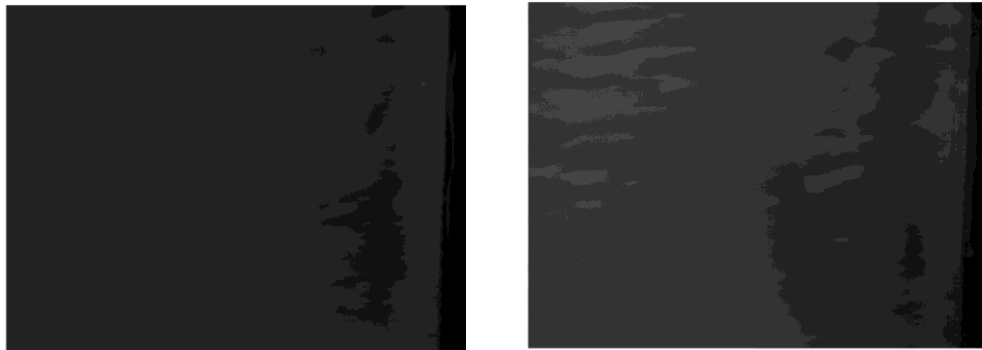


Figure 5.4. Temporally averaged images of the emissions from $5 \mu\text{M}$ FI [left] and SrB [right] volumetrically illuminated at $\lambda = 514 \text{ nm}$ in the heated PDMS-glass channels at $Re = 3.3$. Flow goes from top to bottom in the images.

Figure 5.5 shows a pseudocolor fluid temperature map obtained at $z = 14 \mu\text{m}$ using DFT at $Re = 3.3$ at a spatial resolution of $1.46 \mu\text{m}$ (1 pixel). Flow again goes from top to bottom in the images. Note that the grey region on the right represents the channel

sidewall visible in Figure 5.4. The solution temperature reaches its maximum value of $\sim 43^\circ\text{C}$ at the wall near the heater, then decreases to its minimum value of $\sim 34^\circ\text{C}$ away from the heater, giving a temperature change of 9°C over a y -distance of 1 mm in this portion of the channel. The temperature also increases slightly along the flow direction (opposite to the x -direction) as the fluid continues to be heated by the ITO heater.

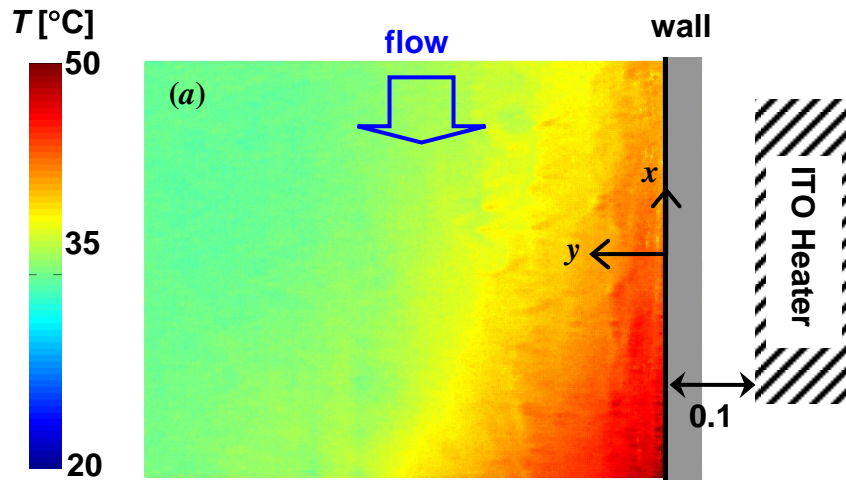


Figure 5.5. Pseudocolor temperature map at $z = 14\ \mu\text{m}$ over a $953\ \mu\text{m}$ (y) \times $718\ \mu\text{m}$ (x) region at a spatial resolution of $1.462\ \mu\text{m}$ (1 pixel) at $Re = 3.3$ in the PDMS-glass channel. The flow goes from top to bottom in the images.

Figure 5.6 compares pseudocolor maps of fluid temperatures measured by DFT near the bottom (glass) wall at $z = 14\ \mu\text{m}$ across the channel (a) and near the top at $z = 950\ \mu\text{m}$ (b) at $Re = 3.3$. Both images have been spatially averaged over regions 34 pixels square and hence have a spatial resolution of $50\ \mu\text{m}$. The flow goes from top to bottom in the images. Overall, the temperatures measured by DFT at $z = 950\ \mu\text{m}$ at a given in-plane location are within 2°C from those at $z = 14\ \mu\text{m}$ —an unexpected result given that the temperature change across the channel near the top wall should be much less than that near the bottom wall since the heater is at the bottom wall. Overall, it appears that DFT can measure in-plane temperature gradients exceeding $10^\circ\text{C}/\text{mm}$, but is unable to resolve

temperatures along the optical, or z -, axis when the entire channel height is illuminated, even for two measurements acquired with the focal plane of the imaging system spaced 0.9 mm apart (*vs.* a depth of focus of 14 μm). This observation suggests that the out-of-plane spatial resolution of DFT is determined by the illumination, and not by the imaging system.

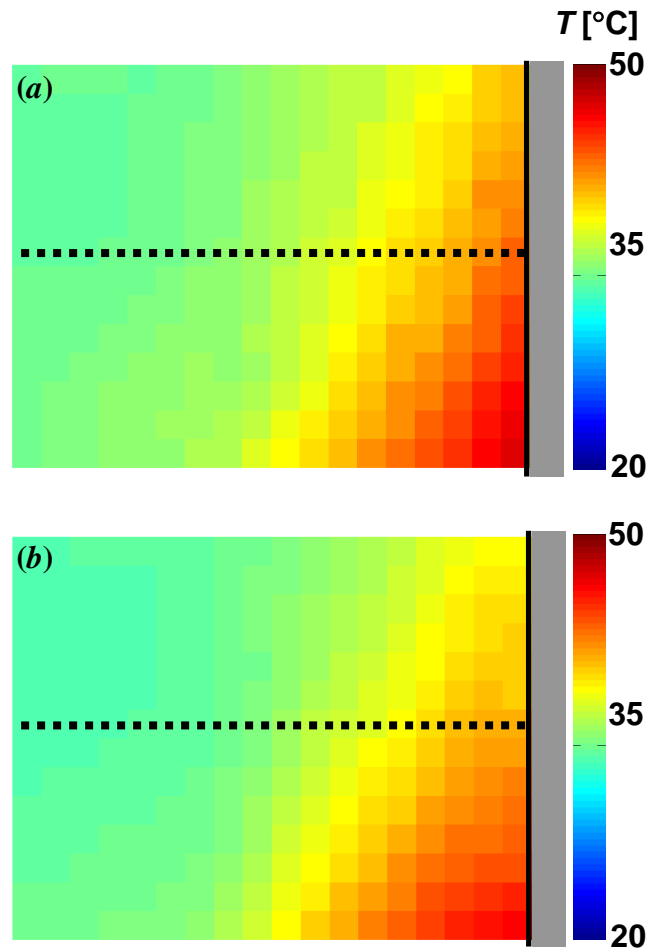


Figure 5.6. Pseudocolor maps of fluid temperatures measured by DFT at the depth of $z = 14 \mu\text{m}$ (*a*) and $z = 950 \mu\text{m}$ (*b*) at $Re = 3.3$ in the PDMS-glass channel. Both images are at a spatial resolution of 50 μm (34 pixels) and flow goes from top to bottom in the images. Note that the map shown in (*a*) is a spatial average of the previous Figure. The dotted line across these images and subsequent images in this Chapter denotes the location of the temperature profile compared to numerical predictions in Sec. 4.4.1.

The numerical simulations carried out with the CFD software packages FLUENT[®] v6.2 and Gambit 2.2.30 to predict the bulk fluid temperature fields were identical to those described in Chapter 4. The predictions where 93% of the electrical input power was converted to the volumetric heat generation rate \dot{q} at the ITO heater in the PDMS-glass channels, which gave the best match to the EFT results (with average temperature differences of 0.36 °C and 0.40 °C at $Re = 3.3$ and 8.3, respectively) were compared with the DFT results. As discussed in Chapter 4, the primary source of error in the FLUENT predictions is due to difficulties in estimating this heat generation rate.

Figure 5.7 shows pseudocolor maps of the fluid temperatures predicted by FLUENT (a) near the bottom (glass) wall at $z = 50 \mu\text{m}$ across the channel and (b) near the top at $z = 950 \mu\text{m}$ at $Re = 3.3$ at a spatial resolution of 50 μm in the PDMS-glass channels at $z = 50 \mu\text{m}$ for this case. The flow goes from the top to the bottom of the image. At $Re = 3.3$, the maximum and minimum predicted temperatures are ~ 47 and ~ 35 °C, giving a temperature difference of more than 12 °C/mm along a y -distance of 1 mm. The predicted fluid temperatures increase more slowly in the streamwise direction than those measured by DFT (Fig. 5.5b), suggesting that the temperature gradient along the flow (x) direction is greater in the DFT data. On the other hand, the maximum and minimum temperatures are ~ 36 and ~ 32 °C at $Re = 8.3$, producing a temperature difference of 4 °C over a y -distance of 1 mm. Obviously, the temperature changes across the channel near the bottom is greater than that near the top because the heater on the bottom wall transfers heat to the fluid nearby.

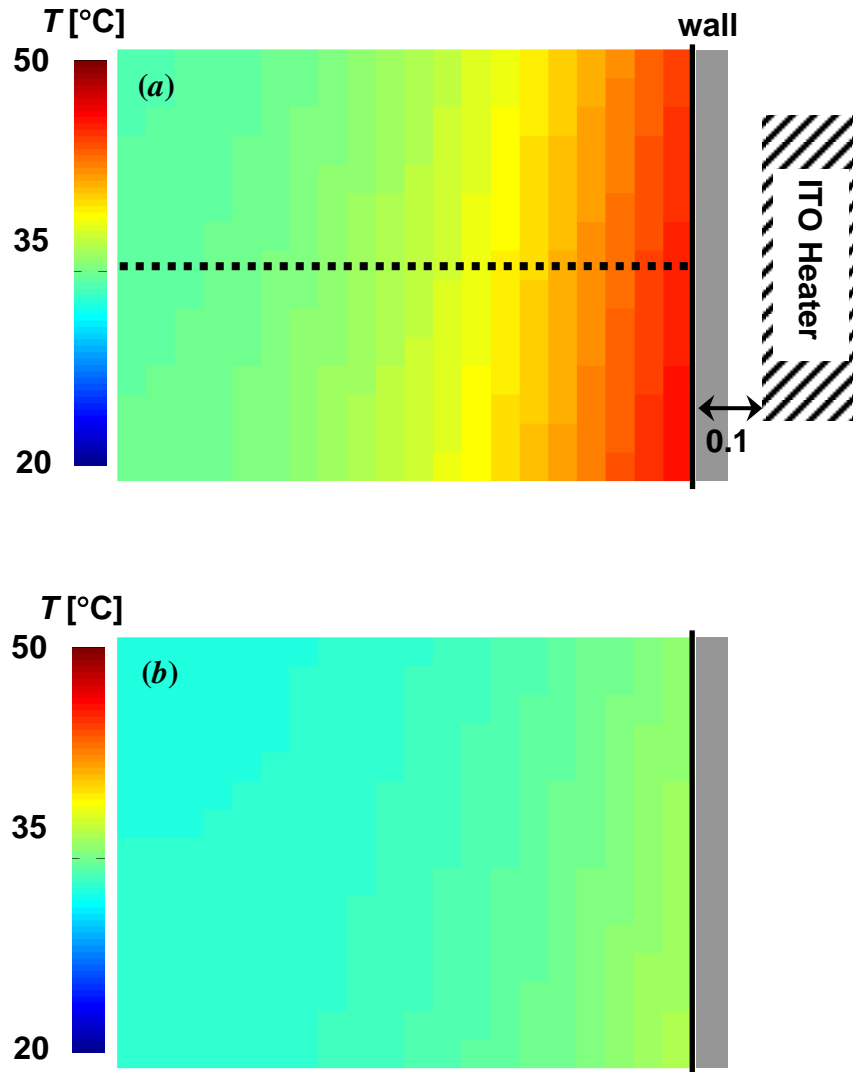
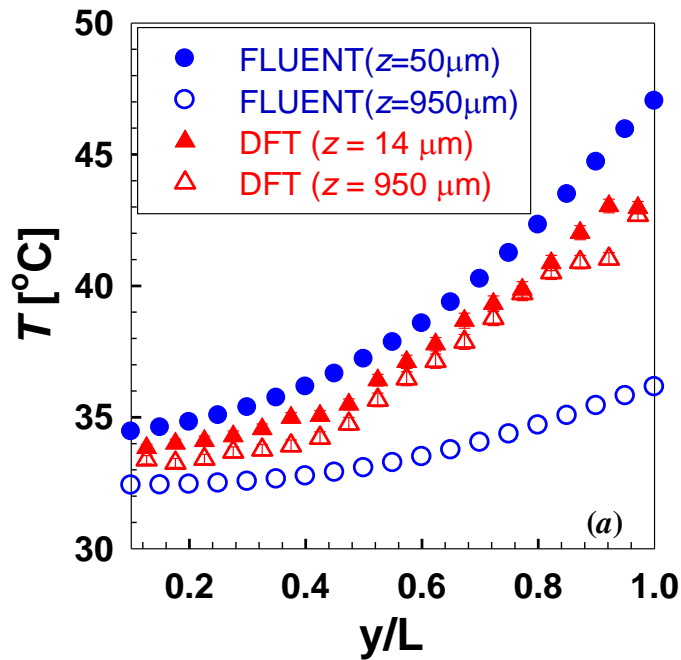


Figure 5.7. Pseudocolor map of the fluid temperature field at $z = 50 \mu\text{m}$ (a) and $z = 950 \mu\text{m}$ (b) predicted by FLUENT in PDMS-glass channels at $Re = 3.3$ with a heat generation rate corresponding to 93% of the input electrical power at a spatial resolution of $50 \mu\text{m}$. The ITO heater is on the right side of the image and the flow goes from top to bottom.

Figure 5.8 compares the temperature profile T near the bottom (glass) wall measured by DFT (*filled triangles*) at $z = 14 \mu\text{m}$ with that predicted by FLUENT (*filled circles*) at $z = 50 \mu\text{m}$ as a function of the normalized coordinate y/L along the dotted line shown in Figure 5.5, 5.6, and 5.7 at $Re = 3.3$ (a) and 8.3 (b). Note that since the

numerical model used to simulate the channel had a spatial resolution of $50\ \mu\text{m}$, the experimentally measured temperatures at $z = 14\ \mu\text{m}$ could only be compared to predictions of the fluid temperature at the location nearest the wall in the simulations, or $z = 50\ \mu\text{m}$. Here, y is again measured across the channel from the side wall nearest the ITO heater (*cf.* Figure 5.5a), and $L = 1\ \text{mm}$ is the channel width. Both temperature profiles are at a spatial resolution of $50\ \mu\text{m}$. The error bars represent one standard deviation in the DFT results.

The Figure also compares temperature profiles near the top (PDMS) wall in the same flow at $z = 950\ \mu\text{m}$ measured by DFT (*open triangles*) with those predicted by FLUENT (*open circles*). This Figure shows that the temperature profiles measured by DFT near the top and bottom walls are nearly identical, while the temperature profiles predicted by FLUENT are very different, with a temperature difference of more than $10\ ^\circ\text{C}$ near the heater.



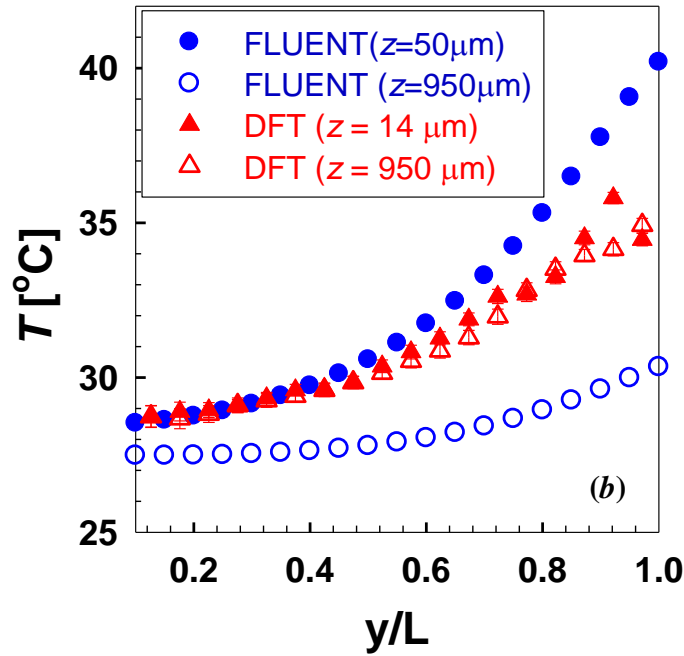


Figure 5.8. Fluid temperatures T as a function of normalized channel coordinate y/L measured by DFT (*triangles*) compared with the predictions from FLUENT (*circles*) at $Re = 3.3$ (a) and 8.3 (b) in the PDMS-glass channel. Filled symbols denote fluid temperatures near the bottom wall at $z = 14 \mu\text{m}$ (DFT) and at $z = 50 \mu\text{m}$ (FLUENT), while open symbols represent fluid temperatures near the top wall at $z = 950 \mu\text{m}$. Both the numerical predictions and the DFT data are presented at a spatial resolution of $50 \mu\text{m}$. The error bars represent one standard deviation in the DFT results.

In contrast, the DFT results near the top and bottom walls have an average discrepancy of $0.7 \text{ }^\circ\text{C}$. The uncertainty in the DFT results, determined from Eq. (5-2) and the standard deviations of the FI and SrB data using standard methods for uncertainty propagation, were $0.22\text{--}0.24 \text{ }^\circ\text{C}$ at a spatial resolution of $50 \mu\text{m}$. So, although the difference in the DFT results obtained near the bottom and top walls is greater than the experimental uncertainty, the difference is nevertheless much less than that predicted by FLUENT. Specifically, the temperature changes at $Re = 3.3$ predicted by FLUENT are $13 \text{ }^\circ\text{C}$ and $4 \text{ }^\circ\text{C}$ across the channel y -dimension of 1 mm at $z = 50 \mu\text{m}$ and $950 \mu\text{m}$, respectively, which suggests that there is a much larger temperature gradient in y near the

bottom wall of the channel, presumably because the ITO heater is 0.1 mm from the channel sidewall on the glass wall. Given that the inlet temperature was measured to be 20 °C, vs. minimum temperatures of 34°C and 32°C at $z = 50 \mu\text{m}$ and $950 \mu\text{m}$, the fluid temperature increases by at least 12 °C from the inlet as it flows through the portion of the heated channel upstream of the region of interest. Similarly, the temperature change across the channel at the higher flow rate corresponding to $Re = 8.3$ in the FLUENT predictions are 12 °C and 3 °C over a y -distance of 1 mm at $z = 50 \mu\text{m}$ and $950 \mu\text{m}$, respectively and the minimum temperatures are 28°C and 27°C at $z = 50 \mu\text{m}$ and $950 \mu\text{m}$, respectively.

The temperature difference is much smaller near the top PDMS wall of the channel, presumably because there is less conduction in this case since PDMS has a thermal conductivity of 0.15 W/(m·K) that is an order of magnitude smaller than that of glass, which is 1.14 W/(m·K). The temperature differences along the 1 mm z -dimension (height) of the channel are, however, comparable for both flow rates: 11 °C and 10 °C at $Re = 3.3$ and 8.3, respectively. These results suggest that convection through the fluid is greater than conduction through the fluid or the PDMS. This is expected, given that that channel Nusselt number Nu ($Nu = hL/k$, where h is the convective heat transfer coefficient of water, $L = 1 \text{ mm}$ is the characteristic length, and k is the thermal conductivity of water) for laminar flow at constant wall temperature and constant heat flux is $O(1)$, suggesting that convection is more significant than conduction.

The inability of these DFT experiments to resolve different temperature fields at different z -locations when the entire z -extent, or height, of the channel is illuminated suggests that fluorescence thermometry with volume illumination has poor spatial resolution along the optical axis. Since the volume illumination excites emissions over the entire depth, or z -extent, of the channel, it is likely that the emissions near the bottom wall of the channel—which have the highest ratio of Fl to SrB emissions because the

fluid temperatures are greatest there—“corrupt” the DFT results, irrespective of the z -location of the focal plane of the imaging system (*i.e.*, microscope objective) within the channel. Even when the focal plane is centered about $z = 950 \mu\text{m}$, the out-of-focus FI and SrB emissions around $z = 50 \mu\text{m}$, a distance corresponding to more than 70 times the depth of field of the imaging system, still effectively overwhelm the in-focus signal with its much weaker temperature gradient and lower temperatures.

The next section describes DFT experiments performed in heated acrylic-glass channels of the same geometry as the PDMS-glass channels to investigate whether these effects are, as hypothesized, due to the volume illumination of the entire channel cross-section. By using acrylic-glass channels, which have much less scattering, DFT is used to measure the fluid temperature fields averaged over the upper and lower portions of the channel cross-section (*i.e.*, $z \approx 0\text{--}400 \mu\text{m}$ and $z \approx 600\text{--}1000 \mu\text{m}$), *vs.* over the entire z -extent of the channel, by only illuminating these portions of the channel.

5.2.2 DFT Results in Acrylic-Glass Channels

Based on the DFT results with volume illumination in PDMS-glass channels, it was hypothesized that DFT could not resolve temperature fields with strong variations along the optical (z) axis, even when changing the z -position of the focal plane of the imaging system, because emissions from the working fluid beyond the focal plane “corrupted” the DFT results. To prove this hypothesis, additional experiments were performed in heated acrylic-glass channels, which were fabricated as described in section 4.2.2.1. Like the PDMS-glass channels, the acrylic-glass channel had a 1 mm square cross-section, and were heated by a thin-film ITO heater on the glass bottom wall which was at an edge distance of 0.1 mm from the side wall of the channel (Figure 5.9a). Acrylic had much less optical scattering than PDMS, both in side the bulk material and at the refractive index-interfaces with air and the working fluid. To further minimize

optical scattering in the bulk acrylic, the thickness of the side wall of the acrylic-PDMS channel away from the heater was reduced to 2 mm, the smallest value that prevented leaking of the working fluid at the acrylic-glass joint.

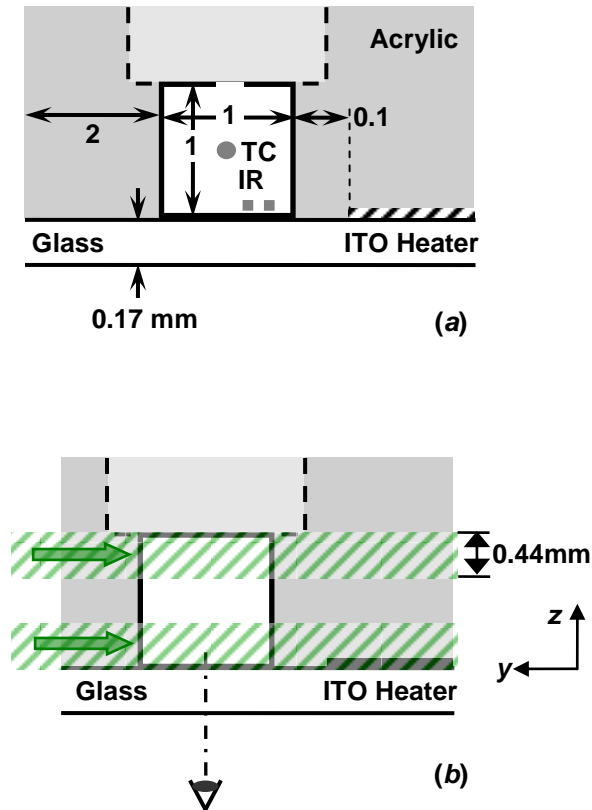


Figure 5.9 (a) A sketch of the acrylic-glass channel used in the DFT experiments and (b) a sketch illustrating how the channel was illuminated by the laser light sheet over the lower and upper portions of the channel over nominal locations $z \approx 0-400 \mu\text{m}$ and $z \approx 600-1000 \mu\text{m}$, respectively, as denoted by the hatched regions. As indicated by the arrows, the light sheet enters the channel through the side wall opposite the heater.

A laser light sheet with a thickness of 0.4 mm was then used to illuminate the channel over the lower and upper portions of the channel, over a nominal range of z -positions of $z \approx 0-400 \mu\text{m}$ and $z \approx 600-1000 \mu\text{m}$, respectively (Figure 5.9b). The beam from a multiline argon-ion laser (543-MA-A03, Melles Griot) with cross-sectional dimensions of 1.4 mm and 1.5 mm along the horizontal and vertical directions, respectively (Sec. 3.2.1.1) was passed through an excitation filter to isolate about 60 mW

of light at $\lambda = 514$ nm, a plano-convex spherical lens (LPX-25.0-207.5-C, Melles Griot) with a focal length of 400 mm, then a plano-concave cylindrical lens (LK1087L2, Thorlabs, Inc.) to produce a light sheet whose thickness was estimated to be 0.4 mm by the knife-edge method (*cf.* Sec. 3.2.1.1). The width of the light sheet was about 0.4 mm just before the light sheet entered the acrylic.

The numerical models for the acrylic-glass channels, as detailed in section 4.4.2, were again calibrated using the results from the EFT studies. Based on the EFT data, the heat generation rate at the ITO heater was taken to be that corresponding to 95.5% of the total electrical input power. Comparing the numerical predictions with the DFT results presents some challenges, however. First, the DFT data are a weighted average of all the emissions excited by the entire 0.4 mm z -extent of the laser light sheet, with presumably the greatest weight on the emissions from the focal plane. Second, there is significant uncertainty in both the actual location of the DFT data and the z -extent of the actual region illuminated by the laser light sheet in the channel due to scattering and refraction of the laser light sheet in the acrylic and the working fluid, as well as optical interference from the glass bottom and acrylic top walls. Because of these issues, the temperature fields measured with DFT in the acrylic-glass channels at a spatial resolution of $50 \mu\text{m}$ were *qualitatively* compared with a “simple” unweighted average of the FLUENT results at the same spatial resolution from $0 \mu\text{m} \leq z \leq 400 \mu\text{m}$ and $600 \mu\text{m} \leq z \leq 1000 \mu\text{m}$.

Figure 5.10a shows the FLUENT predictions for the temperature field as a function of y -position normalized by the channel y -dimension L along the dotted line shown in Figure 5.10 for $z = 0 \mu\text{m}$ (*open diamonds*), $50 \mu\text{m}$ (*open squares*), $100 \mu\text{m}$ (*open triangles*), $150 \mu\text{m}$ (*open circles*), $200 \mu\text{m}$ (*crosses*), $250 \mu\text{m}$ (*filled diamonds*), $300 \mu\text{m}$ (*filled squares*), $350 \mu\text{m}$ (*filled triangles*) and $400 \mu\text{m}$ (*filled circles*). The temperature change across the channel along the y -direction decreases as z increases moving away from the ITO heater, from about $9 \text{ }^\circ\text{C}$ at $z = 0 \mu\text{m}$ to less than $4 \text{ }^\circ\text{C}$ at $z =$

400 μm Clearly, varying the weighting of these temperature profiles when calculating an “average” temperature profile will significantly affect the result.

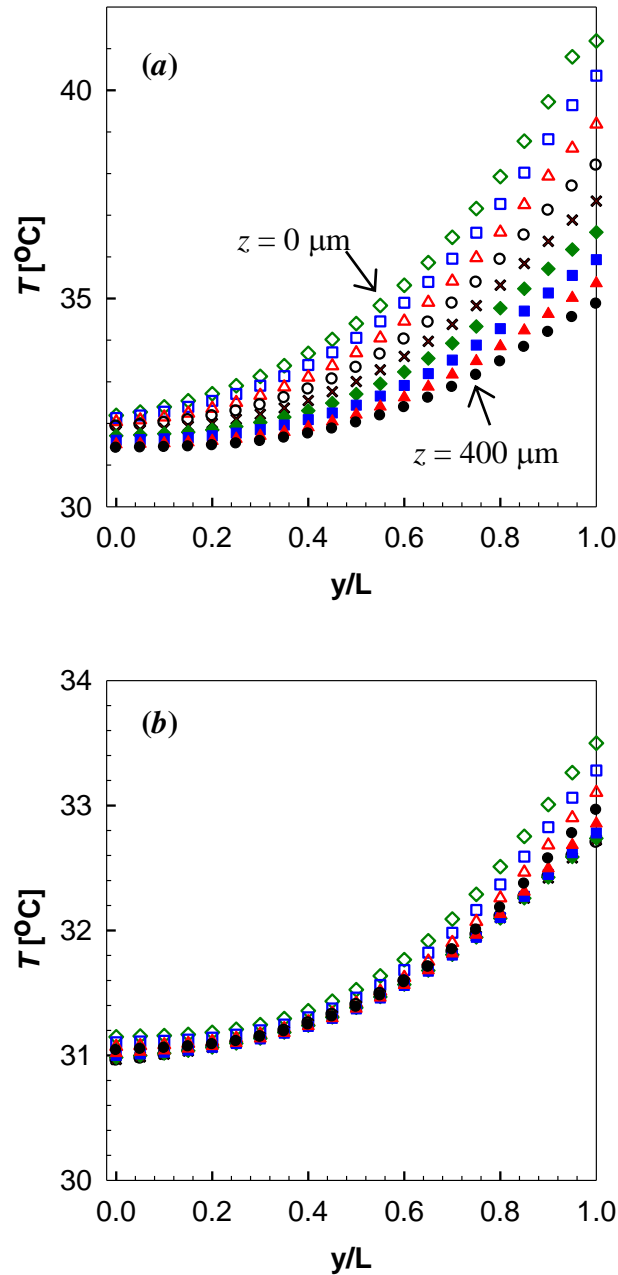


Figure 5.10. Temperatures predicted by FLUENT over the z -positions corresponding to the DFT results, or (a) from $z = 0$ to 400 μm and (b) from $z = 600$ μm to 1000 μm , as a function of y/L at a spatial resolution of 50 μm at $Re = 3.3$.

Figure 5.10b shows temperature profiles obtained with FLUENT for $z = 600$ μm

(*open diamonds*), 650 μm (*open squares*), 700 μm (*open triangles*), 750 μm (*open circles*), 800 μm (*crosses*), 850 μm (*filled diamonds*), 900 μm (*filled squares*), 950 μm (*filled triangles*) and 1000 μm (*filled circles*). Not surprisingly, there is much less variation in the temperature profile with z -position over the upper portion of the channel, suggesting that an unweighted average temperature profile over this region will give a good estimate of the DFT results.

Figure 5.11 and 5.12 compare pseudocolor temperature maps with different temperature scales measured by DFT with those predicted by FLUENT at different z locations for $Re = 3.3$. The flow goes from top to bottom in all images. Figure 5.11 compares (a) the temperature field obtained by DFT over the lower portion of the channel with the focal plane of the objective at $z = 14 \mu\text{m}$ with (b) an unweighted average of the temperature profiles predicted by FLUENT for $z = 0\text{--}400 \mu\text{m}$ shown in Figure 5.10a at $Re = 3.3$. In this comparison, the DFT data starting about 44 μm (30 pixels) away from the side wall next to the heater are compared with averaged FLUENT results starting 50 μm from the same side wall because optical interference from the side wall precluded obtaining accurate DFT results any closer to the wall. In the DFT results, the temperatures gradually decrease from about 37 $^{\circ}\text{C}$ near the heater to 32 $^{\circ}\text{C}$ at $y/L \approx 0.5$. There appears to be a slight increase—about 1 $^{\circ}\text{C}$ —in the fluid temperature near the side wall of the channel opposite the heater, which is likely due to errors associated with the reduced SNR of the FI emissions (and hence the ratio of the FI and SrB signals) at low temperatures. The temperature fields predicted by FLUENT are qualitatively similar, with a gradual and monotonic decrease from about 37 $^{\circ}\text{C}$ near heater to 32 $^{\circ}\text{C}$ near the wall opposite the heater. We emphasize that the comparison between the DFT results and the averaged predictions over the lower portion of the channel are qualitative, since the signal from the focal plane should have a greater weight than signals from z -locations beyond the focal plane and the experimental data are being compared with an unweighted

average of the temperature profiles predicted by FLUENT.

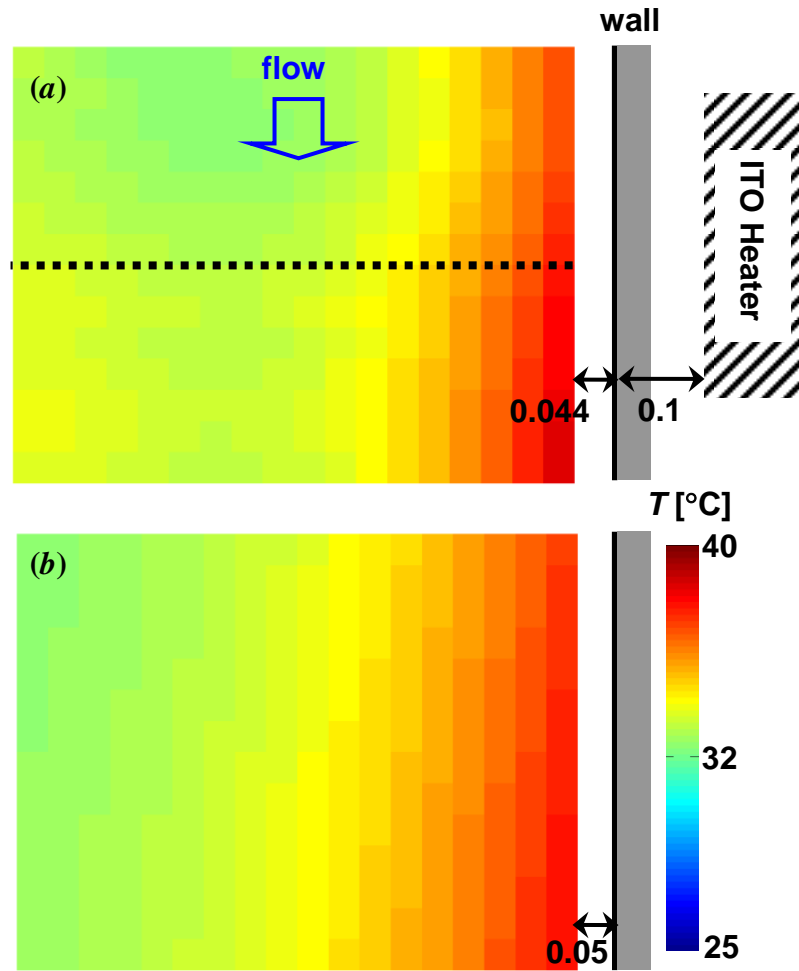


Figure 5.11. Pseudocolor temperature maps measured by DFT (a) at $z = 14 \mu\text{m}$ compared to (b) the predictions of FLUENT averaged over $z = 0\text{--}400 \mu\text{m}$ at $Re = 3.3$ in the acrylic-glass. Both DFT and FLUENT results have a spatial resolution of $50 \mu\text{m}$. Flow goes from top to bottom and the heater is on the right in the images. The dotted line across image a in the center represents the location of the temperature profile compared to the numerical predictions later in this Section.

Figure 5.12 shows similar comparisons, albeit over the top portion of the channel. The temperatures measured by DFT over the top portion of the channel with the focal plane at $z = 950 \mu\text{m}$ are within $1 \text{ }^\circ\text{C}$ of the temperatures predicted by FLUENT at a

similar location averaged over $z = 600\text{--}1000\ \mu\text{m}$, and the average discrepancy between the temperature fields measured by DFT and predicted by FLUENT is 0.56°C . Given that the FLUENT predictions in this region are at most weakly dependent on z , as discussed previously, this discrepancy of $0.56\ ^\circ\text{C}$ is a conservative estimate of the accuracy of the DFT measurements.

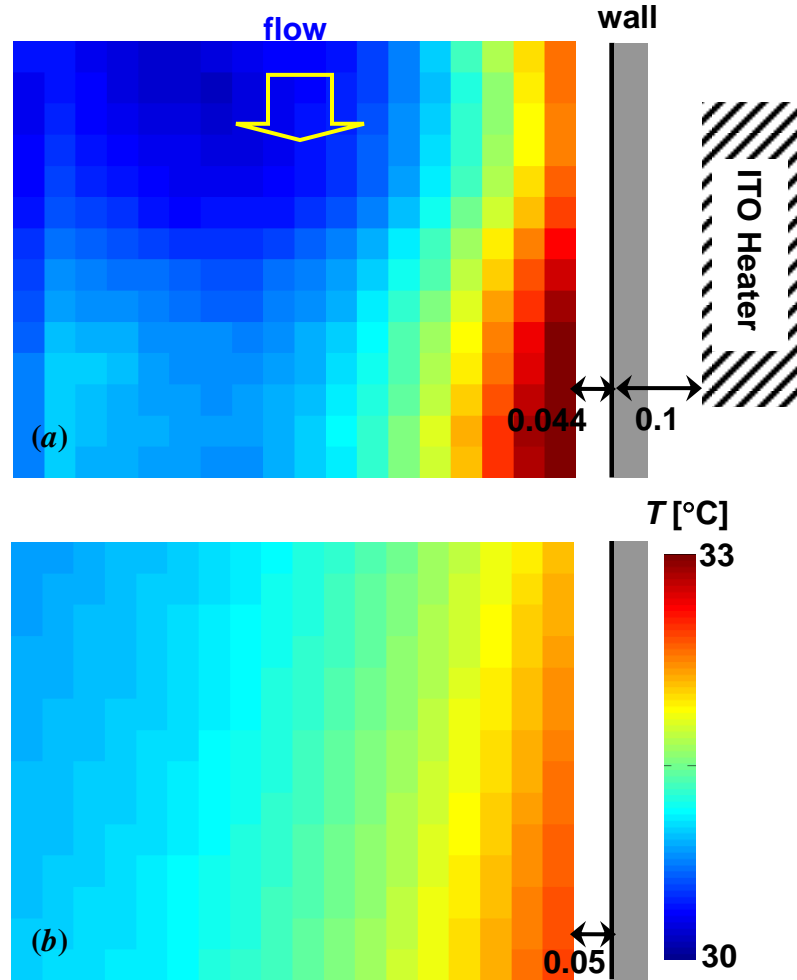


Figure 5.12. Pseudocolor temperature across the acrylic-glass channel (a) measured by DFT channel at $z = 950\ \mu\text{m}$ compared to (b) the predictions of FLUENT averaged over $z = 600\text{--}1000\ \mu\text{m}$ at a spatial resolution of $50\ \mu\text{m}$ at $Re = 3.3$. The flow goes from top to bottom and the heater is on the right in the images. Note that the temperature scale for this Figure differs from that of the previous Figure.

Figure 5.13 compares fluid temperature profiles T along the dotted line in Figure 5.11a as a function of normalized channel coordinate $y/L = 100\text{--}966\ \mu\text{m}$ measured by DFT with illumination over the lower portion of the channel and the objective focal plane at $z = 14\ \mu\text{m}$ (*filled triangles*) and with illumination over the upper portion of the channel and the objective focal plane at $z = 950\ \mu\text{m}$ (*open triangles*) with the predictions from FLUENT averaged over $z = 0\text{--}400\ \mu\text{m}$ (*filled circles*) and $z = 600\text{--}1000\ \mu\text{m}$ (*open circles*) at (a) $Re = 3.3$ and (b) $Re = 8.3$. At $Re = 3.3$, the FLUENT predictions averaged over $z = 0\text{--}400\ \mu\text{m}$ decrease by about $6\ ^\circ\text{C}$ over the $\sim 0.9\ \text{mm}$ y -distance shown, while those averaged over $z = 600\text{--}1000\ \mu\text{m}$ decrease by about $2\ ^\circ\text{C}$. At $Re = 8.3$, those averaged over the lower and upper portions of the channel decrease by about $6\ ^\circ\text{C}$ and $1.5\ ^\circ\text{C}$, respectively, over the $\sim 0.9\ \text{mm}$ distance along the y -axis. The actual fluid temperatures are, however, significantly lower at $Re = 8.3$. These results suggest that heat transfer occurs primarily via convection through water (*vs.* conduction through acrylic), as expected.

The fluid temperatures measured by DFT over the lower and upper portions of the channel are, on average, within $0.53\ ^\circ\text{C}$ and $0.46\ ^\circ\text{C}$, respectively, of the corresponding FLUENT predictions averaged over $z = 0\text{--}400\ \mu\text{m}$ and $z = 600\text{--}1000\ \mu\text{m}$, respectively, at $Re = 3.3$. These discrepancies were determined by interpolating the FLUENT predictions, with its coarser spatial resolution of $50\ \mu\text{m}$, using a curve-fit of a fifth-order polynomial ($R^2 = 99\%$) through the FLUENT values. At $Re = 8.3$, the average discrepancies between the DFT results and the FLUENT predictions were $0.54\ ^\circ\text{C}$ and $0.20\ ^\circ\text{C}$ over the lower and upper portions of the channel, respectively. These discrepancies, at least for the upper portion of the channel, are comparable to the uncertainties in the fluid temperatures measured by DFT. These uncertainties, which were again determined from Eq. (5-2) and the standard deviations of the FI and SrB data (calculated over all 100 images) were, at $Re = 3.3$, $1.1\ ^\circ\text{C}$ and $0.28\ ^\circ\text{C}$ at spatial resolutions of $3\ \mu\text{m}$ (2 pixels) and $50\ \mu\text{m}$ (34

pixels), respectively, and 1.3 °C and 0.30 °C at spatial resolutions of 3 μm and 50 μm, respectively, at $Re = 8.3$ (Kline and McClintock 1953).

Clearly, the DFT measurements of fluid temperature obtained by illuminating only the lower and upper portions of the channel are in much better agreement with the FLUENT results. This result supports our hypothesis that the spatial resolution of DFT along the optical axis is determined by the illumination—and can, as demonstrated in the previous Section, be as great as 70 times the depth of field of the imaging system. In other words, the temperature fields measured by DFT in a microchannel where the entire cross-section of the channel is volumetrically illuminated will be the temperature field averaged over the entire extent of the channel along the optical axis. Improving the spatial resolution of DFT along the optical axis will therefore require illuminating thinner “slices” of the channel.

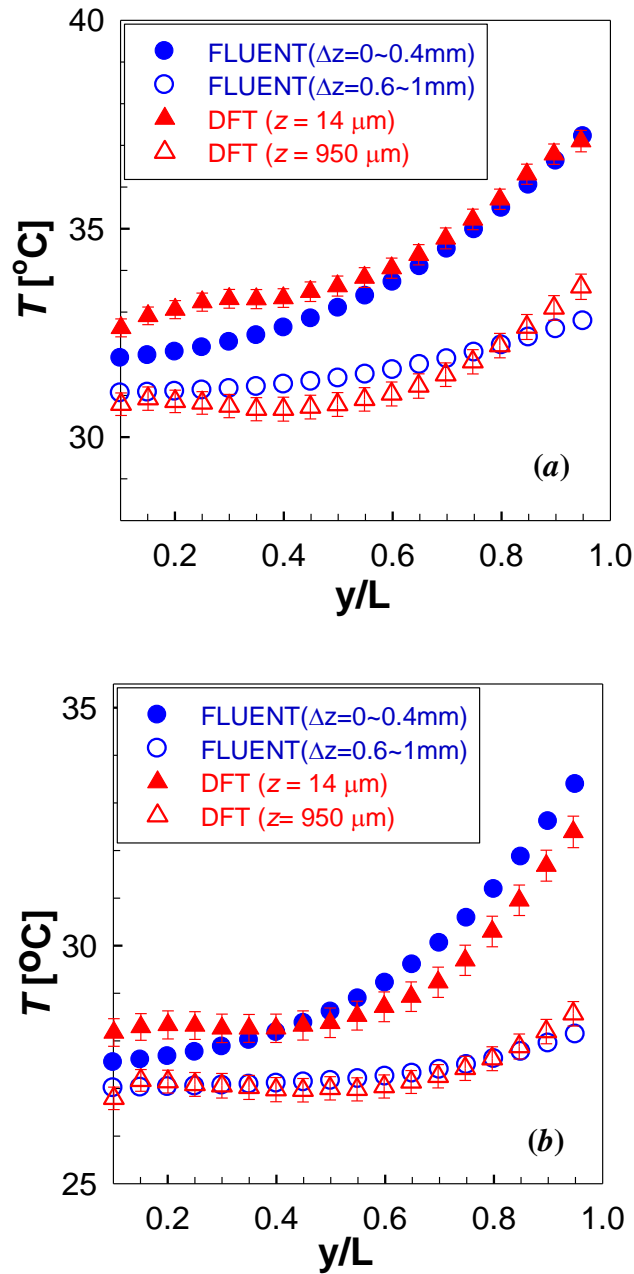


Figure 5.13. Fluid temperatures T as a function of normalized channel coordinate y/L measured by DFT at $z = 14 \mu m$ (filled triangles) and $z = 950 \mu m$ (open triangles) compared with the predictions from FLUENT averaged over $z = 0\text{--}400 \mu m$ (filled circles) and $z = 600\text{--}1000 \mu m$ (open circles) at (a) $Re = 3.3$ and (b) $Re = 8.3$ in the acrylic-glass channel. All results are at a spatial resolution of $50 \mu m$. The error bars represent a standard deviation in the DFT results.

5.3 Summary

This chapter described the use of dual-tracer fluorescence thermometry to measure bulk fluid temperatures in fully-developed incompressible Poiseuille flow at $Re = 3.3$ and 8.3 through 1 mm square PDMS-glass and acrylic-glass channels. To improve sensitivity, two temperature-sensitive fluorophores, Fl and SrB, whose emission intensities increased and decreased, respectively, as temperature increased were used. Calibrations of the temperature sensitivity of ratio of the signals from Fl and SrB showed that the sensitivity of this ratio varied from 4% per $^{\circ}\text{C}$ at $T = 20\text{ }^{\circ}\text{C}$ to 12% per $^{\circ}\text{C}$ at $T = 60\text{ }^{\circ}\text{C}$, suggesting that this technique has greater sensitivity at higher temperatures. These values over this temperature range are, however, also significantly higher than the -2.7% per $^{\circ}\text{C}$ reported by Natrajan and Christensen (2009) for RhB and SrB101 in their microscale DFT studies.

The results of numerical simulations using the CFD software package FLUENT were calibrated using the EFT measurements to estimate the volumetric heat generation rate at the ITO heater. The temperatures predicted by these simulations were then compared with the DFT measurements. Fluid temperatures were first measured by DFT when the entire PDMS-glass channel was illuminated and the focal plane of the imaging system was near the glass bottom wall and PDMS top wall of the channel, or $z = 14\text{ }\mu\text{m}$ and $z = 950\text{ }\mu\text{m}$, respectively. The DFT results obtained at these two different focal plane locations were found to be within $0.7\text{ }^{\circ}\text{C}$ of each other (on average), a result that was not supported by the FLUENT predictions, which showed that the temperature gradients along y were maximum near the bottom wall of the channel, and monotonically decreased as z increased, corresponding to moving towards the top wall of the channel.

Based on these observations, it was hypothesized that DFT could not resolve temperature fields with strong variations along the optical (z) axis, even when changing the z -position of the focal plane of the imaging system, because emissions from the

working fluid beyond the focal plane “corrupted” the DFT results, and that the spatial resolution of DFT along the optical axis is determined by the properties of the illumination, vs. the imaging system.

To test this hypothesis, further DFT experiments were performed in acrylic-glass channels where a ~0.4 mm thick laser light sheet was used to illuminate the lower and upper portions of the channel with the focal plane of the imaging system at $z = 14 \mu\text{m}$ and $950 \mu\text{m}$, respectively. These DFT data were compared with the FLUENT predictions averaged over $z = 0\text{--}400 \mu\text{m}$ and $z = 600\text{--}1000 \mu\text{m}$. Given the experimental difficulties in determining the exact position of the illumination or its spatial extent, an unweighted average of the numerical predictions was calculated, although basic imaging theory would suggest that the signal from the focal plane would have a greater weight than signals from z -locations beyond the focal plane.

The fluid temperatures measured by DFT over the lower and upper portions of the channel are, on average, within $0.53 \text{ }^\circ\text{C}$ and $0.46 \text{ }^\circ\text{C}$, respectively, of the corresponding FLUENT predictions at $Re = 3.3$, and within $0.54 \text{ }^\circ\text{C}$ and $0.20 \text{ }^\circ\text{C}$, respectively, at $Re = 8.3$. These values are comparable to the experimental uncertainties in the DFT results at a spatial resolution of $50 \mu\text{m}$ of $0.28 \text{ }^\circ\text{C}$ and $0.30 \text{ }^\circ\text{C}$ at $Re = 3.3$ and 8.3 , respectively. This result supports the hypothesis that the spatial resolution of DFT along the optical axis is determined by the illumination. The temperature fields measured by DFT in a microchannel where the entire cross-section of the channel is volumetrically illuminated will therefore be averaged over the entire dimension of the channel along the optical axis. Advanced imaging techniques such as confocal microscopy will most likely be required to improve the spatial resolution of dual-tracer fluorescence thermometry in microchannels.

CHAPTER 6

Conclusions and Recommendations

This chapter presents the conclusions of this thesis based on experimental and numerical studies of wall surface and bulk fluid temperatures. The contributions of this work and recommendations for future work are also presented.

6.1 Conclusions

6.1.1 Evanescent Wave Fluorescence Thermometry (EFT)

The feasibility and accuracy of the EFT technique to measure wall surface temperatures were investigated in fully-developed and incompressible Poiseuille flow at $Re = 3.3$ and 8.3 through channels with a 1 mm square cross-section. The emissions from a solution of 30 $\mu\text{mol/L}$ fluorescein (Fl) in DDI were found in calibration studies to increase linearly, when excited at 514 nm, by 1.8 % per $^{\circ}\text{C}$ increase in the solution temperature at temperatures ranging from 20 $^{\circ}\text{C}$ to 60 $^{\circ}\text{C}$. The maximum uncertainty in the EFT measurements of temperature was found to be 0.27 $^{\circ}\text{C}$ based on the standard deviation at a spatial resolution of 10 μm . Two different channels made of PDMS and acrylic were both bonded to a 0.17 mm thick glass substrate with a 300 nm thick ITO heater on the surface facing the fluid. In both channels, the temperature fields in the fluid within 300 nm of the glass wall were obtained at three different locations near the side walls and in the middle of the channel using EFT.

Three-dimensional finite-volume simulations were performed using the CFD software packages FLUENT[®] v6.2 and Gambit 2.2.30 to validate the EFT and DFT results. Since a portion of electrical power input to the heater is dissipated to the surroundings before it reaches the heater, the actual volumetric heat generation rates \dot{q} at

the heater for the simulations were estimated using the value of \dot{q} (corresponding to values less than the actual electrical input power) that best matched the EFT measurements. Comparisons between the EFT measurements and the numerical predictions (which are, admittedly, “tuned” to the EFT data by adjusting \dot{q}) suggest that the EFT measurements are, on average, within 0.47 °C of the wall surface temperature, even in the presence of strong temperature gradients both across and normal to the bottom wall of the channel. These results suggest that EFT can be used to nonintrusively estimate wall surface temperature fields with reasonably good accuracy.

6.1.2 Dual-Tracer Fluorescence Thermometry (DFT)

The accuracy and spatial resolution of DFT for measuring bulk fluid temperatures were evaluated again in fully-developed and incompressible Poiseuille flow at $Re = 3.3$ and 8.3 through of the same 1 mm square PDMS-glass or acrylic-glass channels. Two temperature-sensitive fluorophores, Fl and sulforhodamine B (SrB), with emissions that increased and decreased, respectively, as temperature increased, were used to improve the temperature sensitivity of the technique. The ratio of the Fl to SrB signals from an aqueous solution of 5 μM Fl, 5 μM SrB and 100 mM phosphate buffer was found in calibration studies to increase by about 4–12% per °C increase in the solution temperature T for $T = 20\text{--}60$ °C. This sensitivity is significantly greater the -2.7% per °C for the pair of rhodamine B (RhB) and sulforhodamine 101 reported by Natrajan and Christensen (2009) or -2% per °C for the combination of RhB and rhodamine 110 reported by Sakakibara and Adrian (2004).

The results from the FLUENT simulations at the values of \dot{q} that best matched the EFT data were then used to validate the DFT results obtained in independent experiments in the same flows as those used for the EFT studies. The numerical predictions were compared the DFT measurements obtained near the top and bottom of the channel. For

studies of the Poiseuille flow through the PDMS-glass channels with the entire channel volumetrically illuminated, the temperature fields measured by DFT when the focal plane of the imaging system was at $z = 14 \mu\text{m}$ and $z = 950 \mu\text{m}$ were within $0.7 \text{ }^\circ\text{C}$ on average, vs. an average difference exceeding $3 \text{ }^\circ\text{C}$ in the simulations. Given that the heater is at the bottom of the channel, and the temperature field near the top wall of the channel should be significantly different from that near the bottom, this result suggested that DFT with volume illumination has an extremely poor spatial resolution along the optical axis, and that emissions from the fluid beyond the focal plane contaminate the DFT results.

To prove this hypothesis, fluid temperatures were measured by DFT in acrylic-glass channels illuminated over the lower and upper portions of the channel by a ~ 0.4 mm thick laser light sheet. The focal plane of the imaging system was again placed at $z = 14 \mu\text{m}$ and $950 \mu\text{m}$, respectively. Since the exact z location and extent, of the illuminated region are unknown, an unweighted average of temperatures predicted by the FLUENT simulations was compared with these DFT data. The fluid temperatures measured by DFT over the lower and upper portions of the channel are, on average, within $0.53 \text{ }^\circ\text{C}$ and $0.46 \text{ }^\circ\text{C}$, respectively, of the corresponding averaged FLUENT predictions at $Re = 3.3$, and within $0.54 \text{ }^\circ\text{C}$ and $0.20 \text{ }^\circ\text{C}$, respectively, at $Re = 8.3$. This result supports the hypothesis that the spatial resolution of DFT along the optical axis is determined by the illumination. Given that the temperature field is essentially independent of z over the upper portion of the channel, we conservatively estimate that the DFT technique has an accuracy of $0.46 \text{ }^\circ\text{C}$ and $0.20 \text{ }^\circ\text{C}$ at $Re = 3.3$ and 8.3 , respectively, based on these comparisons.

The temperature fields measured by DFT when the entire cross-section of the channel is illuminated will therefore be averaged over the entire channel along the optical axis. Improving the spatial resolution of fluorescence thermometry along the optical axis in microfluidic devices will therefore likely require advanced imaging techniques such as

confocal microscopy thermometry.

6.2 Contributions

The main contributions of this thesis include the:

1. First, to our knowledge, development and application of non-intrusive fluorescence thermometry using evanescent-wave illumination to measure water temperature fields within the first 300 nm of the wall. The evanescent-wave fluorescence thermometry results, when compared with numerical predictions from the CFD software package FLUENT, demonstrate that these data are a good estimate of the wall surface temperature, with an accuracy of 0.47 °C at a spatial resolution of 10 μm.
2. Extension of dual-tracer fluorescence thermometry using Fl and SrB illuminated at 514 nm to micron-scale flows and demonstration that this combination gives better temperature sensitivities (4–12% per °C) than other fluorophore pairs reported in the literature.
3. First (to our knowledge) demonstration that the spatial resolution of DFT along the optical axis is determined by the illumination, and can easily exceed 70 times the depth of field of the imaging system.
4. Evaluation of the accuracy of the DFT, albeit based on somewhat qualitative comparison of DFT measurements with averaged numerical predictions.

6.3 Recommendations for Future Work

This research has developed non-intrusive fluorescence thermometry techniques to measure wall surface and bulk fluid temperature fields with $O(1 \mu\text{m})$ spatial resolution. In terms of further work on this topic:

1. The current studies show that the spatial resolution of DFT along the optical axis

is determined by the illumination, and is, in the case of volume illumination, quite poor. To obtain spatially resolved temperature fields along the optical axis, advanced illumination and imaging techniques such as confocal microscopy and using beams of light with waists as small as 100 μm will be required.

2. Dual-tracer thermometry using EFT could potentially further improve the accuracy of wall surface temperature data. Although we were unable to find a second temperature-sensitive fluorescent species that did not adsorb on borosilicate glass, water-soluble CdSe/ZnS quantum dots may be a possibility for a second temperature tracer. Guasto and Breuer (2008) reported that these tracers had a temperature sensitivity of -0.85% per $^{\circ}\text{C}$.
3. The accuracy of EFT was significantly affected by diffraction patterns that were inherent to the objective-based TIRF system used in these studies. The objective-based TIRF system was also limiting in that it had a relatively small field of view ($160\ \mu\text{m} \times 120\ \mu\text{m}$) and could only be used to image through an optical medium with a thickness of 170 μm and a refractive index of 1.51, *i.e.*, a coverslip of borosilicate glass. Using a prism-based evanescent-wave illumination system would probably improve the capabilities of EFT.
4. One of the major potential applications for this work is in developing heat sinks consisting of a three-dimensional network of up to several hundred microchannels connected by numerous manifolds for microelectronic cooling. As reviewed in the Introduction, accurate temperature data are important in evaluating and designing new thermal management technologies.

More specifically, measurements of the wall and coolant temperatures could be used to develop local heat transfer correlations in geometries that include the effects of thermal coupling at these small scales that could be used in reduced-order models. Computational analysis of the thermal transport through a channel network of this geometric complexity, even for laminar flows, is quite time-

consuming. Moreover, at these spatial scales, it is likely that there will be significant thermal coupling between individual channels, and so classic macroscale heat transfer correlations developed for individual channels are unlikely to give accurate results for such configurations.

Finally, we note that there are significant inconsistencies between previous studies of the heat transfer characteristics of microchannels in single- and two-phase flow. Accurate, well-validated thermometry techniques—such as the EFT technique developed here, which can estimate wall surface temperatures with an accuracy of about 0.5 °C at a spatial resolution of 10 μm and the DFT technique developed in this thesis which can measure liquid temperatures at accuracy of 0.5 °C at a spatial resolution of 50 μm—could improve our fundamental understanding of thermal transport in such flows, and lead to improved correlations for these flows that are valid at the microscale.

REFERENCES

Adams, T. M., Abdel-Khalik, S. I., Jeter, S. M., and Qureshi, Z. H., "An experimental investigation of single-phase forced convection in microchannels," *Int J Heat Mass Tran*, vol. 41, no. 6–7, pp. 851–857, 1998.

Adams, T. M., Ghiaasiaan, S. M. and Abdel-Khalik, S. I., "Enhancement of liquid forced convection heat transfer in microchannels due to the release of dissolved noncondensables," *Int J Heat Mass Tran*, vol. 42, no. 19, pp. 3563–3573, 1999.

Ajami, A. H., Banerjee, K.B., and Pedram M., "Modeling and analysis of nonuniform substrate temperature effects on global ULSI interconnect," *IEEE T Comput Aid D*, vol. 24, no. 6, pp. 849–861, 2005.

Alivisatos, A. P., "Semiconductor clusters, nanocrystals, and quantum Dots," *Science*, vol. 271, pp. 933–937, 1996.

Allen, P. B., Rodriguez, I., Kuyper, C. L., Lorenz, R. M., Spicar-Mihalic, P., Kuo J. S., and Chiu, D. T., "Selective electroless and electrolytic deposition of metal for applications in microfluidics: Fabrication of a microthermocouple," *Anal Chem*, vol. 75, no. 7, pp. 1578–1583, 2003.

Allison, S. W., Gillies, G. T., Rondinone, A. J., and Cates, M. R., "Nanoscale thermometry via the fluorescence of YAG:Ce phosphor particles: measurements from 7 to 77 °C," *Nanotechnology*, vol. 14, no. 8, pp. 859–863, 2003.

Arakawa, A., Saito, K., and Gruver, W. A., "Automated infrared imaging temperature measurement with application to upward flame spread studies. Part I," *Combust Flame*, vol. 92, no. 3, pp. 222–230, 1993.

Aranyosi, A., Bolle, L. M. R. and Buyse, H. A., "Compact air-cooled heat sinks for power packages," *IEEE T Compon Pack A*, vol. 20, pp.442–451, 1997.

Axelrod, D., "Total internal reflection fluorescence microscopy in cell biology," *Traffic*, vol. 2, no. 11, pp. 764–774, 2001.

Banerjee, A. and Kihm, K. D., "Experimental verification of near-wall hindered diffusion for the Brownian motion of nanoparticles using evanescent wave microscopy," *Phys Rev E*, vol. 72, no. 4, 042101, 2005.

Beckman, P., Roy, R. P., Whitfield, K., and Hasan, A., "A fast-response microthermocouple," *Rev Sci Instrum*, vol. 64, no. 10, pp. 2947–2950, 1993.

Biju, V., Makita, Y., Sonoda, A., Yokoyama, H., Baba, Y., and Ishikawa, M., "Temperature-sensitive photoluminescence of CdSe quantum dot clusters," *J Phys Chem*

B, vol. 109, no. 29, pp. 13899–13905, 2005.

Blanks, H. S., “The temperature dependence of component failure rate,” *Microelectron Reliab*, vol. 20, no. 3, pp. 297–307, 1980.

Bowers, M. B. and Mudawar, I., “High flux boiling in low flow rate, low pressure drop mini-channel and micro-channel heat sinks,” *Int J Heat Mass Tran*, vol. 37, no. 2, pp. 321–332, 1994.

Bruchhausen, M., Guillard, F., and Lemoine, F., “Instantaneous measurement of two-dimensional temperature distributions by means of two-color planar induced fluorescence (PLIF),” *Exp Fluids*, vol. 38, no. 1, pp. 123–131, 2005.

Camci, C., Kim, K., and Hippensteele, S. A., “A new hue capturing technique for the quantitative interpretation of liquid crystal images used in convective heat transfer studies,” *J Turbomach*, vol. 114, no. 4, pp. 765–775, 1992.

Camci, C., Kim, K., Hippensteele, S. A., and Poinatte, P. E., “Evaluation of a hue capturing based transient liquid crystal method for high-resolution mapping of convective heat transfer on curved surfaces,” *J Heat Trans*, vol. 115, no. 2, pp. 311–318, 1993.

Castanet, G., Lavieille, P., Lebouche, M., and Lemoine, F., “Measurement of the temperature distribution within monodisperse combusting droplets in linear streams using two-color laser-induced fluorescence,” *Exp Fluids*, vol. 35, no. 6, pp. 563–571, 2003.

Castanet, G., Maqua, C., Orain, M., Grisch, F., Lemoine, F., “Investigation of heat and mass transfer between the two phases of an evaporating droplet stream using laser-induced fluorescence techniques: Comparison with modeling,” *Int J Heat Mass Trans*, vol. 50, no. 17–18pp. 3670–3683, 2007.

Chamarthy, P., Garimella, S. V., and Wereley, S. T., “Non-intrusive temperature measurement using microscale visualization techniques,” *Exp Fluids*, vol. 47, no. 1, pp. 159–170, 2009.

Chan, W. C. W. and Nie S., “Quantum dot bioconjugates for ultrasensitive nonisotropic detection,” *Science*, vol. 281, no. 5385, pp. 2016–2018, 1998.

Cheng, Y. –K, Raha, P., Teng, C. –C, Rosenbaum, E., and Kang, S. –M., “ILLIADS-T: An electrothermal timing simulator for temperature-sensitive reliability diagnosis of CMOS VLSI chips,” *IEEE T Comput Aid D*, vol. 17, no. 8, pp. 668–681, 1998.

Chronis, N. and Lee L. P., “Total internal reflection-based biochip utilizing a polymer-filled cavity with a micromirror sidewall,” *Lap Chip*, vol. 4, no. 2, pp. 125–130, 2004.

Chung, J., Grigoropoulos, C. P., and Greif, R., “Infrared thermal velocimetry in MEMS-based fluidic devices,” *J Microelectromech S*, vol. 12, no. 3, pp. 365–372, 2003.

Ciofalo, M., Signorino, M., and Simiano, M., “Tomographic particle-image velocimetry

and thermography in Rayleigh-Bénard convection using suspended thermochromic liquid crystals and digital image processing,” *Exp Fluids*, vol. 34, no. 2, pp. 156–172, 2003.

Coolen M. C. J., Kieft, R. N., Rindt, C. C. M., and Steenhoven, A. A. V., “Application of 2-D LIF temperature measurements in water using a Nd:YAG laser,” *Exp Fluids*, vol. 27, no. 5, pp. 420–426, 1999.

Coppeta, J. and Rogers, C., “Dual emission laser induced fluorescence for direct planar scalar behavior measurements,” *Exp Fluids*, vol. 25, no. 1, pp. 1–15, 1998.

Crimaldi, J. P., “The effect of photobleaching and velocity fluctuations on single-point LIF measurements,” *Exp Fluids*, vol. 23, no. 4, pp. 325–330, 1997.

Dabiri, D. and Gharib, M., “The effects of forced boundary conditions on flow within a cubic cavity using digital particle image thermometry and velocimetry (DPITV),” *Exp Therm Fluid Sci*, vol. 13, no. 4, pp. 349–363, 1996.

Deprédurand, V., Miron, P., Labergue, A., Wolff, M., Castanet, G., and Lemoine, F., “A temperature-sensitive tracer suitable for two-colour laser-induced fluorescence thermometry applied to evaporating fuel droplets,” *Meas Sci Technol*, vol. 19, no. 10, 105403, 2008

Ekkad, S. V. and Han J. C., “A transient liquid crystal thermography technique for gas turbine heat transfer measurements,” *Meas Sci Technol*, vol. 11, no. 7, pp. 957–968, 2000.

Erickson, D., Liu, X., Venditti, R., Li, D., and Krull, U. J., “Electrokinetically based approach for single-nucleotide polymorphism discrimination using a microfluidic device,” *Anal Chem*, vol. 77, no. 13, pp. 4000–4007, 2005.

Fan, C. H. and Longtin, J. P., “Laser-based measurement of liquid temperature or concentration at a solid-liquid interface,” *Exp Therm Fluid Sci*, vol. 23, no. 1–2, pp. 1–9, 2000.

Fang, C., Steinbrenner, J. E., Wang, F. –M. and Goodson, K. E., “Impact of wall hydrophobicity on condensation flow and heat transfer in silicon microchannels,” *J Micromech Microeng*, vol. 20, no. 4, pp. 045018, 2010. Impact of wall hydrophobicity on condensation flow and heat transfer in silicon microchannels

Farina, D. J., Hacker, J. M., Moffat, R. J., and Eaton, J., “Illuminant invariant calibration of thermochromic liquid crystals,” *Exp Therm Fluid Sci*, vol. 9, no. 1, pp. 1–12, 1994.

FLIR systems, “The ultimate infrared handbook for R&D professional,” Version 1.

Fogg, D., David, M., and Goodson, K., “Non-invasive measurement of void fraction and liquid temperature in microchannel flow boiling,” *Exp Fluids*, vol. 46, no. 4, pp. 725–736, 2009.

Fu, R. and Li, D., "Study of the temperature field in microchannels of a PDMS chip with embedded local heater using temperature-dependent fluorescent dye," *Int J Therm Sci*, vol. 45, no. 9, pp. 841–847, 2006.

Fujisawa, N. and Funatani, S., "Simultaneous measurement of temperature and velocity in a turbulent thermal convection by the extended range scanning liquid crystal visualization technique," *Exp Fluids*, vol. 29, no. 1, pp. s158–s165, 2000.

Fujisawa, N., Funatani, S., and Katoh, N., "Scanning liquid-crystal thermometry and stereo velocimetry for simultaneous three-dimensional measurement of temperature and velocity field in a turbulent Rayleigh-Bénard convection," *Exp Fluids*, vol. 38, no. 3, pp. 291–303, 2005.

Gao, P., Person, S. L., and Favre-Marinet, M., "Scale effect on hydrodynamics and heat transfer in two-dimensional mini and microchannels," *Int J Therm Sci*, vol. 41, no. 11, pp. 1017–1027, 2002.

Gerion, D., Pinaud, F., Williams, S. C., Parak, W. J., Zanchet, D., Weiss, S., and Alivisatos, A. P., "Synthesis and properties of biocompatible water-soluble silica-coated CdSe/ZnS semiconductor quantum dots," *J Phys Chem B*, vol. 15, no. 37, pp. 8861–8871, 2001.

Gillot, C., Schaeffer, C. and Bricard, A., "Integrated micro heat sink for power multichip module," *IEEE T Compon Pack A*, vol. 36, no. 1, pp. 217–321, 2000.

Gualous, H., Louahli-Gualous, H., and Bocus, S., "Realization and thermal characterization of thin-film optothermal microsensor," *Eur Phys J - Appl Phys*, vol. 14, no. 2, pp. 147–152, 2001

Guasto, J. S. and Breuer, K. S., "Simultaneous, ensemble-averaged measurement of near-wall temperature and velocity in steady micro-flows using single quantum dot tracking," *Exp Fluids*, vo. 45, no. 1, pp. 157–166, 2008.

Guasto, J. S. and Breuer, K., "High-speed quantum dot tracking and velocimetry using evanescent wave illumination," *Exp Fluids*, vol. 47, no. 6, pp. 1059–1066, 2009.

Guasto, J. S. and Breuer, K., "Simultaneous, ensemble-averaged measurement of near-wall temperature and velocity in steady micro-flows using single quantum dot tracking," *Exp Fluids*, vol. 45, no. 1, pp. 157–166, 2008.

Guilbault, G, *Practical Fluorescence: Theory Methods and Techniques*, Marcel Dekker, New York, 1973.

Gurram, S. P., Suman, S. K., Joshi, Y. K. and Fedorov, A. G., "Thermal issues in next-generation integrated circuits," *IEEE T Device Mater Reliab*, vol. 4, no. 4, pp. 709–714, 2004.

Han, G. and Breuer, K. S., "Infrared PIV for measurement of fluid and solid motion

inside opaque silicon microdevices,” 4th Int Sym Particle Image Velocimetry, PTVGö ttingen, Germany, September 17–19, 2001.

Han, I. Y. and Kim S. J., “Diode temperature sensor array for measuring micro-scale surface temperatures with high resolution,” *Sensors Actuators A*, vol. 141, no. 1, pp. 52–58, 2008.

Harms, T. M., Kazmierczak, M. J., Gerner, F. M., “Developing convective heat transfer in deep rectangular microchannels,” *Int J Heat Fluid Flow*, vol. 20, no. 2, pp. 149–157, 1999.

Hidrovo, C. H., Kramer, T. A., Wang, E. N., Vigneron, S., Steinbrenner, J. E., Koo, J., Wang, F., Fogg, D. W., Flynn, R. D., Lee, E. S., Cheng, C., Kenny, T. W., Eaton, J. K., and Goodson, K. E., “Two-phase microfluidics for semiconductor circuits and fuel cells,” *Heat Transfer Eng*, vol. 27, no. 4, pp. 53–63, 2006.

Hiller, W. J., Koch, S. T., Kowalewski, T. A., and Stella, F., “Onset of natural convection in a cube,” *Int J Heat Mass Trans*, vol. 36, no. 13, pp. 3251–3263, 1993

Hines, M. A. and Scholes, G. D., “Colloidal PbS nanocrystals with size-tunable near-infrared emission: observation of post-synthesis self-narrowing of the particle size distribution,” *Adv Mater*, vol. 15, no. 21, pp. 1844–1849, 2003.

Hippensteele, S. A., Russell, L. M., and Stepka, F. S., “Evaluation of a method for heat transfer measurements and thermal visualization using a composite of a heater element and liquid crystals,” *J Heat Trans*, vol. 105, no. 1, pp.184–189, 1983.

Hishida, H. and Sakakibara, J., “Combined planar laser-induced fluorescence-particle image velocimetry technique for velocity and temperature fields,” *Exp Fluids*, vol. 29, suppl. 1, pp. s129–s140, 2000.

Hohreiter, V., Wereley, S. T., Olsen, M. G., and Chung, J. N., “Cross-correlation analysis for temperature measurement,” *Meas Sci Technol*, vol. 13, no. 7, pp. 1072–1078, 2002.

Hollingsworth, D. K., Boehman, A. L., Smith, E. G., and Moffat, R. J., “Measurement of temperature and heat transfer coefficient distributions in a complex flow using liquid crystal thermography and true-color image processing,” *ASME Collected papers in Heat Trans*, pp. 35–42, 1989.

Hu, H. and Koochesfahani, M. M., “A novel technique for quantitative temperature mapping in liquid by measuring the lifetime of laser induced phosphorescence,” *J Visual*, vol. 6, no. 2, pp. 143–153. 2003.

Hu, H., Koochesfahani, M. M., and Lum, C., “Molecular tagging thermometry with adjustable temperature ,” *Exp Fluids*, vol. 40, no. 5, pp. 753–763, 2006.

Huang, T. and Pawliszyn, J., “Microfabrication of a tapered channel for isoelectric focusing with thermally generated pH gradient,” *Electrophoresis*, vol. 23, no. 20, pp.

3504–3510, 2002.

Incropera FP, DeWitt DP (2002) *Fundamentals of Heat and Mass Transfer*, 5th Ed.: John Wiley & Sons, Inc

Ireland, P. T. and Jones, T. V., “The response time of a surface thermometer employing encapsulated thermochromic liquid crystals,” *J Phys E: Sci Instrum*, vol. 20, no. 10, pp. 1195–1199, 1987.

Ireland, P. T. and Jones, T. V., “Liquid crystal measurements of heat transfer and surface stress,” *Meas Sci Technol.*, vol. 11, no. 7, pp. 969–986, 2000.

Jang, S. P., Kim, S. J. and Paik, K. W., “Experimental Investigation of Thermal Characteristics for a Microchannel Heat Sink Subject to an Impinging Jet, Using a Micro-Thermal Sensor Array,” *Senser Actuator A-Phys*, vol. 105, no. 2, pp. 211–224, 2003.

Jeong, D. W., Lee, C. Y., and Lee, S. Y., “Measurement of fluid temperature across microscale gap using two-color ratiometric laser-induced fluorescence technique in combination with confocal microscopy,” *J Heat Trans*, vol. 131, no. 9, 091601, 2009

Jiang, L., Wong, M., and Zohar, Y., “Forced convection boiling in a microchannel heat sink,” *J Microelectromech S*, vol. 10, no. 10, pp. 80–87, 2001.

Jiang, L., Wong, M., and Zohar, Y., “Phase change in microchannel heat sinks with integrated temperature sensors,” *J Microelectromech S*, vol. 8, no. 4, pp. 358–365, 1999.

Jiang, P. –X, Fan, M. –H, Si, G. –S, Ren, Z. –P, “Thermal-hydraulic performance of small scale micro-channel and porous-media heat-exchangers,” *Int J Heat Mass Tran*, vol. 44, no. 5, pp. 1039–1051, 2001.

Jorge, P. A., Mayeh, M., Benrashid, R., Caldas, P., Santos, J. L., and Farahi F., “Quantum dots as self-referenced optical fibre temperature probes for luminescent chemical sensors,” *Meas Sci Technol*, vol. 17, no. 5, pp. 1032–1038, 2006.

Joshi, Y., Azar, K., Blackburn, D., Lasance, C. J. M., Mahajan, R., and Rantala, J., “How well can we assess thermally driven reliability issues in electronic systems today? Summary of panel held at the Therminic 2002,” *Microelectr J*, vol. 34, no. 12, pp. 1195–1201, 2003.

Kang, S. –W., Wei, W. –C, Tsai, S. –H, and Yang, S. –Y., “Experimental investigation of silver nano-fluid on heat pipe thermal performance,” *Appl Therm Eng*, vol. 26, no. 17-18, pp. 2377–2382, 2006.

Khanikar, V., Mudawar, I. and Fisher, T. S., “Flow boiling in a micro-channel coated with carbon nanotubes,” *IEEE T Compon Pack T*, vol. 32, no. 3, pp. 639–649, 2009.

Kihm, K. D., Banerjee, A, Choi, C. K., and Takagi, T., “Near-wall hindered Brownian diffusion of nanoparticles examined by three-dimensional ratiometric total internal

reflection fluorescence microscopy (3-D R-TIRFM),” *Exp Fluids*, vol. 37, no. 6, pp. 811–824, 2004.

Kim, H. J., Kihm, K. D., and Allen, J. S., “Examination of ratiometric laser induced fluorescence thermometry for microscale spatial measurement resolution,” *Int J Heat Mass Trans*, vol. 46, no. 21, pp. 3967–3974, 2003.

Kline, S. J. and McClintock, F. A., “Describing uncertainties in single-sample experiments,” *Mech Eng*, vol. 75, no. 1, pp. 3–9, 1953.

Koch, J. D. and Hanson, R. K., “Temperature and excitation wavelength dependencies of 3-pentanone absorption and fluorescence for PLIF applications,” *Appl Phys B*, vol. 76, no. 3, pp. 319–324, 2003.

Konishi, T., Ito, A., and Saito, K., “Transient infrared temperature measurements of liquid-fuel surfaces: results of studies of flames spread over liquids,” *Appl Optics*, vol. 39, no. 24, pp. 4278–4283, 2000.

Koo, J. –M., Im, S., Jiang, L., and Goodson, K. E., “Integrated microchannel cooling for three-dimensional electronic circuit architectures,” *J Heat Trans*, vol. 127, no. 1, pp. 49–58, 2005.

Kopp, M. U., de Mello, A. J., and Manz, A., “Chemical amplification: continuous-flow PCR on a chip,” *Science*, vol. 280, no. 5366, pp. 1046–1048, 1998.

Kowalewski, T. A., “Particle image velocimetry and thermometry using liquid crystal tracers,” 4th Int Sym Particle Image Velocimetry, Göttingen, Germany, pp. 1134.1–1134.10, 2001.

Larsen, L. G. and Crimaldi, J. P., “The effect of photobleaching on PLIF,” *Exp Fluids*, vol. 41, no. 5, pp. 803–812, 2006.

Lavieille, P., Delconte, A., Blondel, D., Lebouché, and Lemoine, F., “Non-intrusive temperature measurements using three-color laser-induced fluorescence,” *Exp Fluids*, vol. 36, no. 5, pp. 706–716, 2004.

Lavieille, P., Lemoine, F., Lavergne, G., and Lebouche, M., “Evaporating and combusting droplet temperature measurements using two-color laser-induced fluorescence,” *Exp Fluids*, vol. 31, no. 1, pp. 45–55, 2001.

Lavieille, P., Lemoine, F., Lavergne, G., Virepinte, J. F., and Lebouché, M., “Temperature measurements on droplets in monodisperse stream using laser-induced fluorescence,” *Exp Fluids*, vol. 29, no. 5, pp. 429–437, 2000.

Le, N. C. H., Dao, D. V., Yokokawa, R., Wells, J., and Sugiyama, S., “Design, simulation and fabrication of a total internal reflection (TIR)-based chip for highly sensitive fluorescent imaging,” *J Micromech Microeng*, vol. 17, no. 6, pp. 1139–1146, 2007.

- Lee, J. and Mudawar, I., "Fluid flow and heat transfer characteristics of low temperature two-phase micro-channel heat sinks–Part 2. Subcooled boiling pressure drop and heat transfer," *Int J Heat Mass Tran*, vol. 51, no. 17–18, 2008.
- Lemoine, F., Antoine, Y., Wolff, M., and Lebouche, M., "Simultaneous temperature and 2D velocity measurements in a turbulent heated jet using combined laser-induced fluorescence and LDA," *Exp Fluids*, vol. 26, no. 4, pp. 315–323, 1999.
- Liu, T. C., Huang, Z. L., Wang, H. Q., Wang, J. H., Li, X. Q., Zhao, Y. D., and Luo Q. M., "Temperature-dependent photoluminescence of water-soluble quantum dots for a bioprobe," *Anal Chem Acta*, vol. 559, no. 1, pp. 120–123, 2006.
- Majumdar, A., "Scanning thermal microscopy ," *Annu Rev Mater Sci*, vol 29, pp. 505–585, 1999.
- Mallik, A. K. and Peterson, G. P., "Steady-state investigation of vapor deposited micro heat pipe arrays," *J Electron Packaging*, vol. 117, no.1, pp. 75–81, 1995.
- Maqua, C., Castanet, G., Lemoine, F., Doué, N., and Lavergne, G., "Temperature measurements of binary droplets using three-color laser-induced fluorescence," *Exp Fluids*, vol. 40, no. 5, pp. 786–797, 2006.
- Mendels, D. A., Graham, E. M., Magennis, S. W., Jones, A. C., and Mendels, F., "Quantitative comparison of thermal and solutal transport in a T-mixer by FLIM and CFD," *Microfluid Nanofluid*, vol.5, no. 5, pp. 605–617, 2008.
- Metzger, D. E., Bunker, R. S., and Bosch, G., "Transient liquid crystal measurement of local heat transfer on a rotating disk with jet impingement," *J Heat Trans*, vol. 113, no. 1, pp. 52–59, 1991.
- Michalet, X., Pinaud, F. F., Bentolila, L. A., Tsay, J. M., Doose, S., Li, J. J., Sundaresan, G., Wu, A. M., Gambhir, S. S., Weiss, S., "Quantum dots for live cells, in vivo imaging, and diagnostics, *Science*, vol. 307, no. 5709, pp. 538–544, 2005.
- Mosier, B. P., Molho, J. I., and Santiago, J. G., "Photobleached-fluorescence imaging of microflows," *Exp Fluids*, vol. 33, no. 4, pp. 545–554, 2002.
- Motosuke, M., Akutsu, D., and Honami, S., "Temperature measurement of microfluids with high temporal resolution by laser-induced fluorescence," *J Mech Sci Technol*, vol. 23, no. 7, pp. 1821–1828, 2009.
- Nakajima, T., Utsunomiya, M., and Ikeda, Y., "Simultaneous measurement of velocity and temperature of water using LDV and fluorescence technique," 5th Int. Symposium on Application of Laser Techniques to Fluid Mechanics, Lisbon, Portugal, 1990.
- Natrajan, V. K. and Christensen, K. T., "Two-color laser-induced fluorescent thermometry for microfluidic systems," *Meas Sci Technol*, vol. 20, no.1, 015401, 2009.

- Olsen, M. G. and Adrian, R. J., "Brownian motion and correlation in particle image velocimetry," *Optic Laser Technol*, vol. 32, no. 7–8 pp. 621–627, 2000.
- Ozawa, M., Müller, U., Kimura, I., and Takamori, T., "Flow and temperature measurement of natural convection in a Hele-Shaw cell using a thermo-sensitive liquid-crystal tracer," *Exp Fluids*, vol. 12, no. 4–5, pp. 213–222, 1992.
- Paik, P. Y., Pamula, V. K., and Chakrabarty, K., "Adaptive cooling of integrated circuits using digital microfluidics," *IEEE T VLSI SYST*, vol. 16, no. 4, pp. 432–443, 2008.
- Pal, A., Joshi, Y. K., Beitelmal, M. H., Patel, C. D., and Wenger, T. M., "Design and performance evaluation of a compact thermosyphon," *IEEE T Compon Pack T*, vol. 25, no. 4, pp. 601–607, 2002.
- Palm, B., "Heat transfer in microchannels," *Microscale Therm Eng*, vol. 5, no. 3, pp. 155–175, 2001.
- Park, H. G., Dabiri, D., and Gharib, M., "Digital particle image velocimetry/thermometry and application of the wake of a heated circular cylinder," *Exp Fluids*, vol. 30, no. 3, pp. 327–338, 2001.
- Park, J. –J. and Taya, M., "Design of micro-temperature sensor array with thin film thermocouples," *J Electron Packaging*, vol. 127, no. 3, pp. 286–289, 2005.
- Park, J. S., Choi, C. K., and Kihm, K. D., "Temperature measurement for a nanoparticle suspension by detecting the Brownian motion using optical serial sectioning microscopy (OSSM)," *Meas Sci Technol*, vol. 16, no. 7, pp. 1418–1429, 2005.
- Patil, V. A. and Narayanan, V., "Spatially resolved temperature measurement in microchannels," *Microfluidics Nanofluidics*, vol. 2, no. 4, pp. 291–300, 2006.
- Pehl, M, Werner, F., and Delgado, A., "First visualization of temperature fields in liquids at high pressure using thermochromic liquid crystals," *Exp Fluids*, vol. 29, no. 3, pp. 302–304, 2000.
- Peng, X. F. and Peterson, G. P., "Convective heat transfer and flow friction for water flow in microchannel structures," *Int J Heat Mass Tran*, vol. 39, no. 12, pp. 2599–2608, 1996
- Peng, X. F. and Peterson, G. P., "The effect of thermofluid and geometrical parameters on convectin of liquids through rectangular microchannels," *Int J Heat Mass Tran*, vol. 38, no. 4, pp. 755–758, 1995.
- Peng, X. F. and Wang, B. –X., "Forced convection and flow boiling heat transfer for liquid flowing through microchannels," *Int J Heat Mass Tran*, vol. 36, no. 14, pp. 3421–3427, 1993.
- Perret, C., Boussey, J., Schaeffer, C. and Coyaud, M., "Analytic modeling, optimization,

and realization of cooling devices in silicon technology,” *IEEE T Compon Pack T*, vol. 23, no. 4, pp. 665–672, 2000.

Peterson, G. P. and Mallik, A. K., “Transient response characteristics of vapor deposited micro heat pipe arrays,” *J Electron Packaging*, vol. 117, no. 1, pp. 82–87, 1995

Pit, R., Hervet, H., and Léger, L., “Direct experimental evidence of slip in hexadecane: solid interfaces,” *Phys Rev Lett*, vol. 85, no. 5, pp. 980–983, 2000.

Pouya, S., Koochesfahani, M., Snee, P., Bawendi, M., Nocera, D., “Single quantum dot (QD) imaging of fluid flow near surfaces,” *Exp Fluids*, vol. 39, no. 4, pp. 784–786, 2005.

Qu, W. Mala, M., and Li, D., “Heat transfer for water flow in trapezoidal silicon microchannels,” *Int J Heat Mass Tran*, vol. 43, no. 21, pp. 3925–3936, 2000

Richards, C. D. and Richards, R. F., “Transient temperature measurements in a convectively cooled droplet,” *Exp Fluids*, vol. 25, no. 5–6, pp. 392–400, 1998.

Rohrbach, A., “Observing secretory granules with a mutliangle evanescent wave microscope,” *Biophys J*, vol. 78, no. 8, pp. 2641–2654, 2000.

Ross, D. and Locascio, L. E., “Microfluidic temperature gradient focusing,” *Anal Chem*, vol. 74, no. 11, pp. 2556–2564, 2002.

Ross, D., Gaitan, M., and Locascio, L. E., “Temperature measurement in microfluidic systems using a temperature-dependent fluorescent dye,” *Anal Chem*, vol. 73, no. 17, pp. 4117–4123, 2001.

Roy S. K. and Avanic, B. L., “A very high heat flux microchannel heat exchanger for cooling of semiconductor laser diode arrays,” *IEEE T Compon Pack B*, vol. 19, no. 2, pp. 444–451, 1996

Rush, R. S., Cohen, A. S., and Karger, B. L., “Influence of column temperature on the electrophoretic behavior of myoglobin and alpha-lactalbumin in high-performance capillary electrophoresis,” *Anal Chem*, vol 63, no. 14, pp. 1346–1350, 1991.

Sadr, R., Li, H., and Yoda, M., “Impact of hindered Brownian diffusion on the accuracy of particle-image velocimetry using evanescent-wave illumination,” *Exp Fluids*, vol. 38, no. 1, pp. 90–98, 2005.

Sadr, R., Yoda, M., Zheng, Z., and Conlisk, A. T., “An experimental study of electro-osmotic flow in rectangular microchannels.” *J Fluid Mech*, vol. 506, pp. 357–367, 2004.

Sadr, R., Hohenegger, C., Li, H., Mucha, P. J., and Yoda, M., “Diffusion-induced bias in near-wall velocimetry,” *J Fluid Mech*, vol. 577, pp. 443–456, 2007.

Sakakibara, J., Hishida, K., and Maeda, M., “Measurements of thermally stratified pipe flow using image-processing techniques,” *Exp Fluids*, vol. 16, no. 2, pp. 82–96, 1993.

- Sakakibara, J., Hishida, K., and Maeda, M., "Vortex structure and heat transfer in the stagnation region of an impinging plane jet (simultaneous measurements of velocity and temperature fields by digital particle image velocimetry and laser-induced fluorescence)," *Int J Heat Mass Trans*, vol. 40, no. 13, pp. 3163–3176, 1997.
- Sakakibrara, J. and Adrian, R. J., "Measurement of temperature field of a Rayleigh-Bénard convection using two-color laser-induced fluorescence," *Exp Fluids*, vol. 37, no. 3, pp. 331–340, 2004.
- Sakakibrara, J. and Adrian, R. J., "Whole field measurement of temperature in water using two-color laser induced fluorescence," *Exp Fluids*, vol. 26, no. 1–2, pp. 7–15, 1999.
- Samy, R., Glawdel, T., and Ren, C. L., "Method for microfluidic whole-chip temperature measurement using thin-film poly(dimethylsiloxane)/RhB," *Anal Chem*, vol. 80, no. 2, pp. 369–375, 2008.
- Santiago, J. G., Wereley, S. T., Meinhart, C. D., Beebe, D. J., and Adrian, R. J., "A particle image velocimetry system for microfluidics," *Exp Fluids*, vol. 25, no. 4, pp. 316–319, 1998.
- Sato, Y., Irisawa, G., Ishizuka, M., Hishida, K., and Maeda, M., "Visualization of convective mixing in microchannel by fluorescence imaging," *Meas Sci Technol*, vol. 14, no. 1, pp. 114–121, 2003.
- Schrum, K.F., Lancaster, J.M., Johnston, S.E., and Gilman, S.D., "Monitoring electroosmotic flow by periodic photobleaching of a dilute, neutral fluorophore," *Anal Chem*, vol. 72, no. 18, pp. 4317–4321, 2000.
- Sclar, N. and Pollock, D. B., "On diode thermometer," *Solid State Electron*, vol. 15, no. 5, pp. 473–480, 1972.
- Seuntiëns, H. J., Kieft, R. N., Rindt, C. C. M., and Steenhoven, A. A., V., "2D temperature measurements in the wake of a heated cylinder using LIF," *Exp Fluids*, vol. 31, no. 5, pp. 588–595, 2001.
- Shafii, M. B., Lum, C. L., and Koochesfahani, M. M., "In situ LIF temperature measurements in aqueous ammonium chloride solution during uni-directional solidification," *Exp Fluids*, vol. 48, no. 4, pp. 651–662, 2009.
- Shi, L., Kwon, O., Miner, A. C., Majumdar, A., "Design and batch fabrication of probes for sub-100nm scanning thermal microscopy," *J Microelectromech S*, vol. 10, no. 3, pp. 370–378, 2001.
- Shwarts, Y. M., Borblik, V. L., Kulish, N. R., Venger, E. F., and Sokolov, V. N., "Limiting characteristics of diode temperature sensors," *Sensors Actuators*, vol. 86, no. 3, pp. 197–205, 2000.

- Song, L, Hennink, E. J., Young, I. T., and Tanke, H. J., "Photobleaching kinetics of fluorescein in quantitative fluorescence microscopy," *Biophys J*, vol. 68, no. 6, pp. 2588–2600, 1995.
- Song, L, Varma, C. A. G. O., Verhoeven, J. W., and Tanke, H. J., "Influence of the triplet excited state on the photobleaching kinetics of fluorescein in microscopy," *Biophys J*, vol. 70, no. 6, pp. 2959–2968, 1996.
- Sutton, J. A., Fisher, B. T., and Fleming, J. W., "A laser-induced fluorescence measurement for aqueous fluid flows with improved temperature sensitivity," *Exp Fluids*, vol. 45, no. 5, pp. 869–881, 2008.
- Thompson, N. L. and Axelrod, D., "Immunoglobulin surface-binding kinetics studied by total internal reflection with fluorescence correlation spectroscopy," *Biophys J*, vol. 43, no. 1, pp. 103–114, 1983.
- Thompson, N. L. and Lagerholm, B. C., "Total internal reflection fluorescence: applications in cellular biophysics," *Curr Opin Biotech*, vol. 8, no. 1, pp. 58–64, 1997.
- Thomson, S. L. and Maynes, D., "Spatially resolved temperature measurements in a liquid using laser induced phosphorescence," *J Fluid Eng*, vol. 123, pp. 293–302, 2001.
- Toomre, D. and Manstein, D. J., "Lighting up the cell surface with evanescent wave microscopy," *Trends Cell Bio*, vol. 11, no. 7, pp. 298–303, 2001.
- Tsai, C. -H. and Kang, S. -M., "Cell-level placement for improving substrate thermal distribution," *IEEE T Comput Aid D*, vol. 19, no. 2, pp. 253–266, 2000.
- Tsai, C. Y., Chien, H. T., Ding, P. P., Chan, B., Luh, T. Y., Chen, P. H., "Effect of structural character of gold nanoparticles in nanofluid on heat pipe thermal performance," *Mater Lett*, vol. 58, no. 9, pp. 1461–1465, 2004.
- Tuckerman, D. B. and Pease, R. F. W., "High-performance heat sinking for VLSI," *IEEE Electr Device L*, vol. 2, no. 5, pp. 126–129, 1981.
- Vafai, K. and Zhu, L., "Analysis of two-layered micro-channel heat sink concept in electronic cooling," *Int J Heat Mass Trans*, vol. 42, no. 12, pp. 2287–2297, 1999.
- Verkruysse, W., Jia, W., Franco, W., Milner T. E., and Nelson, J. S, "Infrared measurement of human skin temperature to predict the individual maximum safe radiant exposure (IMSRE)," *Lasers Surg Med*, vol. 39, no. 10, pp. 757–766, 2007.
- Walker, G. W., Sundar V. C., Rudzinski, C. M., Wun A. W., Bawendi, M. G., and Nocera, D. G., "Quantum-dot optical temperature probes," *Appl Phys Lett*, vol. 83, no. 17, pp. 3555–3557, 2003.
- Wang, B. X. and Peng, X. F., "Experimental investigation on liquid forced-convection heat transfer through microchannels," *Int J Heat Mass Tran*, vol. 37, suppl. 1, pp. 73–82,

1994.

Wei, X., Joshi, Y., and Patterson, M. K., "Experimental and numerical study of stacked microchannel heat sink for liquid cooling of microelectronic devices," *J Heat Transfer*, vol. 129, no. 10, pp. 1432, 2007.

Wolff, M., Delconte, A., Schmidt, F., Gucher, P., and Lemoine, F., "High-pressure diesel spray temperature measurements using two-colour laser-induced fluorescence," *Meas Sci Technol*, vol. 18, no. 3, pp. 697–706, 2007.

Wu, P. and Little, W. A., "Measurement of the heat transfer characteristics of gas flow in fine channel heat exchanges used for microminature refrigerators," *Cryogenics*, vol. 24, no. 8, pp. 415–420, 1984.

Yamada, J., "Evanescent wave Doppler velocimetry for a wall's near field," *Appl Phys Lett*, vol. 75, no. 12, pp. 1805–1806, 1999.

Zettner, C. M. and Yoda, M., "Particle velocity field measurements in a near-wall flow using evanescent wave illumination," *Exp Fluids*, vol. 34, no. 1, pp. 115–121, 2003.

Zhuang, Y., Ma, C. F., and Qin, M., "Experimental study on local heat transfer with liquid impingement flow in two-dimensional micro-channels," *Int J Heat Mass Tran*, vol. 40, no. 17, pp. 4055–4059, 1997.